APPLIED COMPUTER SCIENCE

The Journal is a peer-reviewed, international, multidisciplinary journal covering a broad spectrum of topics of computer application in production engineering, technology, management and economy.

The main purpose of Applied Computer Science is to publish the results of cutting-edge research advancing the concepts, theories and implementation of novel solutions in computer technology. Papers presenting original research results related to applications of computer technology in production engineering, management, economy and technology are welcomed.

We welcome original papers written in English. The Journal also publishes technical briefs, discussions of previously published papers, book reviews, and editorials. Especially we welcome papers which deals with the problem of computer applications in such areas as:

- manufacturing,
- engineering,
- technology,
- designing,
- organization,
- management,
- economics,
- innovations,
- competitiveness,
- quality and costs.

The Journal is published quarterly and is indexed in: BazTech, Cabell's Directory, CNKI Scholar (China National Knowledge Infrastucture), ERIH PLUS, Google Scholar, Index Copernicus, J-Gate, Scopus, TEMA Technik und Management.

Letters to the Editor-in-Chief or Editorial Secretary are highly encouraged.

CONTENTS

Applied Computer Science, vol. 17, no. 3, pp. 5–18
doi: 10.23743/acs-2021-17

Submitted: 2021-06-13 | Revised: 2021-09-07 | Accepted: 2021-09-21

CPU-GPU, High-performance computing,
Kernel, Data transfer, CUDA streams

K. RAJU [0000-0001-6731-5427]*, *Niranjan N CHIPLUNKAR* [0000-0003-4223-2355]**

PERFORMANCE ENHANCEMENT OF CUDA APPLICATIONS BY OVERLAPPING DATA TRANSFER AND KERNEL EXECUTION

Abstract

The CPU-GPU combination is a widely used heterogeneous computing system in which the CPU and GPU have different address spaces. Since the GPU cannot directly access the CPU memory, prior to invoking the GPU function the input data must be available on the GPU memory. On completion of GPU function, the results of computation are transferred to CPU memory. The CPU-GPU data transfer happens through PCI-Express bus. The PCI-E bandwidth is much lesser than that of GPU memory. The speed at which the data is transferred is limited by the PCI-E bandwidth. Hence, the PCI-E acts as a performance bottleneck. In this paper two approaches are discussed to minimize the overhead of data transfer, namely, performing the data transfer while the GPU function is being executed and reducing the amount of data to be transferred to GPU. The effectiveness of these approaches on the execution time of a set of CUDA applications is realized using CUDA streams. The results of our experiments show that the execution time of applications can be minimized with the proposed approaches.

1. INTRODUCTION

The Graphics Processing Unit (GPU) was originally developed for rendering the images. With hundreds of processing cores modern GPUs are found to be ideal for speeding up data parallel applications. CUDA C/C++ API is used for programming the GPU for general-purpose computation. The execution time of a program can be easily reduced by offloading the CPU computations to the GPU. As a result, nowadays the CPU-GPU heterogenous computing systems are extensively used in many high-performance computing applications.

The GPU is a co-processor operated under the control of central processing unit (CPU). According to CUDA terminology (NVIDIA, 2015), the CPU with its memory is called as host and the GPU with its memory is called as device. The function to be executed on the device is known as kernel. Thousands of threads are created when the kernel is invoked from the host. These threads are organized as blocks, and the blocks are organized as grid. An instance of the kernel code is executed by each thread of the grid.

* Department of CSE, NMAM Institute of Technology, Nitte, India, rajuk@nitte.edu.in, nchiplunkar@nitte.edu.in

Figure 1 depicts the control flow during the execution of any CUDA program. A CUDA program is the combination of host executable and device executable code. Since the host memory is not directly accessible to the device, input data is copied through PCI-e from the host to device. The kernel function is invoked after transferring the input data. The kernel is parallelly executed by several threads. However, each thread computes on separate portion of input data. On completion of kernel execution, the computed results are transferred from the memory of device to that of the host.

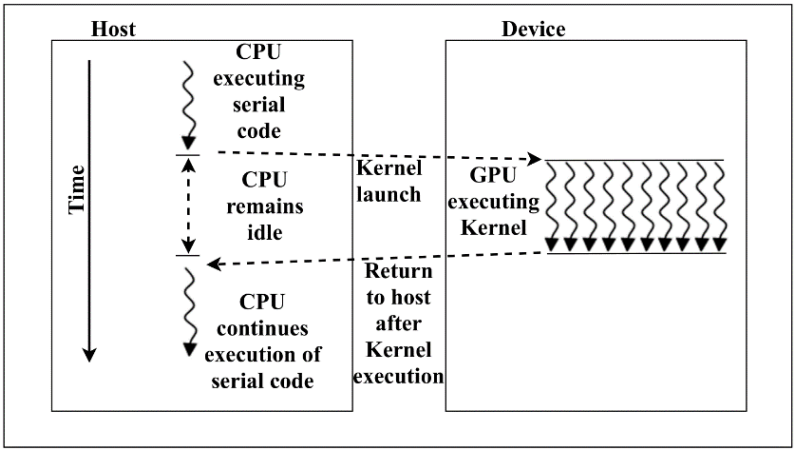

Fig. 1. Flow of control during the execution of CUDA program

The communication bandwidth of GPU memory is much higher than that of PCI-e. The data transfer speed is limited by the bandwidth of PCIe bus. The latest version of PCIe standard (PCI-e 5.0) supports a bandwidth of 128 GBps. NVIDIA's recent, most powerful supercomputing GPU architecture for PC, TITAN V, has a memory bandwidth of 652.8 GBps (NVIDIA TITAN V, n.d.), which is much higher than the bandwidth of PCIe 5.0. The data transfer overhead reduces the performance gain obtained from the use of GPU (Gregg & Hazelwood, 2011). This overhead can be reduced if the data transfer can happen in parallel with the kernel execution.

Another method to mitigate the data transfer bottleneck is to offload a part of GPU workload to the CPU cores. From the host's perspective, calling a kernel is an asynchronous process. A call to GPU function returns immediately and does not wait until the completion of kernel execution. While the GPU is executing the kernel, the CPU can continue the execution of host code, where it can perform computations, launch any other kernels, or transfer data between host and device memory. Modern CPUs comprise multiple cores, each with immense computing capacity. Huge amount of CPU computational power is wasted unless these cores are involved in some useful computation when the GPU is executing the kernel function. It is hard to find computation that can be performed on CPU cores in parallel with kernel execution, as these computations which are performed after the kernel launch normally depend on the results produced by the current kernel. However, in the case of data parallel applications a part of GPU workload can be offloaded to CPU cores. This approach reduces the GPU workload and also the volume of data traffic between CPU and GPU (Huang et al., 2012). Moreover, with this technique the idle CPU cores can be efficiently utilized.

CUDA provides streams, a mechanism that facilitates execution of the kernel in parallel with data transfer. Thus, CUDA applications can be positively sped up by offloading GPU workload to the CPU together with the overlapped kernel execution and data transfer.

In a CUDA program the operations that involve the device, such as CPU-GPU data transfer, kernel launch, etc., are issued by the host. A queue of GPU operations or commands is known as stream. The commands in a stream are executed in their arrival order. Every GPU command is associated with a stream, whose identifier is specified as a parameter to the command. If no stream identifier is specified by the programmer then that command is issued to the default stream or null stream.

A host thread can define multiple non-default streams. The commands in the different non-default streams are considered to be independent and can be executed concurrently. The commands coming from the same stream are executed in the sequential order. Figure 2-a depicts the execution timeline of the GPU operations with a default stream. The captions HtoD and DtoH followed by an index stand for the host to device and device to host data transfers respectively. A kernel is referred to by the caption K followed by an index. The index of a data transfer operation is same as the index of the corresponding kernel.

The commands are performed in the same order that they appear in the stream. The commands in the non-default streams will be started only after the completion of operations in the default stream. However, a new operation in the default stream cannot be started before the completion of already initiated operations in the non-default streams. Figure 2-b gives the execution timeline of the GPU operations on two non-default streams. As shown in this figure, the operations from two different streams can be overlapped. For example, execution of kernel K1 and the HtoD2 data transfer can happen simultaneously.

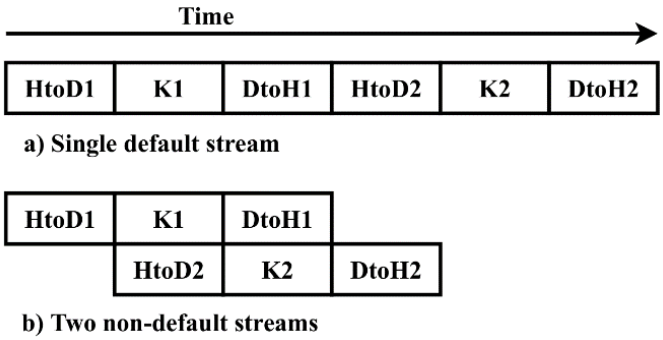

Fig. 2. Execution time line of CUDA commands with (a) single default stream, and (b) two non-default streams

Modern GPUs possess one execution engine and two copy engines. The host to device and device to host data transfer operations use separate copy engines. Data transfer commands from different streams are issued to the relevant copy engines. The copy engines can utilize the full duplex nature of PCI-e bus. That is, two data transfer operations of opposite directions which are from two different streams can be overlapped. Multiple cores of a GPU are considered as a single execution engine for kernel scheduling purpose. The following are the requisites to use CUDA streams to enable concurrent execution of operations through copy and the execution engines:

1. The device must support concurrent copy and kernel execution.
2. Two data transfer operations can be overlapped only if they are in different directions.
3. Commands (for copying the data and invoking the kernel) which are to be overlapped need to be added to separate non-default streams.
4. Pinned or non-pageable memory must be used at the host side.

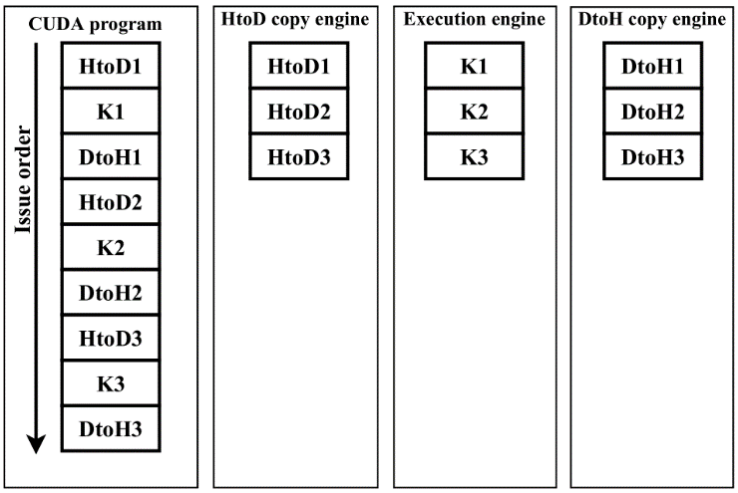

Fig. 3. Issue order of commands to CUDA engines

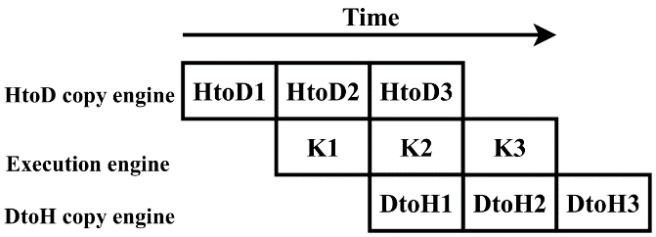

Fig. 4. Execution order of commands in copy and execution engines

Figure 3 shows the order in which the data transfer and kernel launch operations of a program are issued to appropriate CUDA engines. The execution order of commands from different engines are as shown in the figure 4. The operations from different engines can be overlapped if there exists no dependency among the them. Execution of kernel K1 cannot be overlapped with HtoD1 data transfer, as K1 and HtoD1 are from the same stream as shown in figure 2-b and K1 depends on the completion of HtoD1. Whereas HtoD2 data transfer and execution of kernel K1 can be overlapped since these two operations are from different streams and K1 does not depend on the HtoD2 data transfer. Data transfer operations HtoD3 and DtoH1 can be overlapped as these operations are from separate streams and are in opposite directions.

In CUDA, the data transfer operations using `cudaMemcpy()` are synchronous or blocking in nature. The function returns only after the data is copied. The non-blocking version this operation is `cudaMemcpyAsync()`, which requires the data to be allocated in the page-locked memory. The memory allocated using `malloc()` is pageable memory.

Host can swap this memory to disk when more space is required. Page-locked memory or pinned is a portion of memory that is not available for swapping. The pageable memory of the host does not support DMA transfers to or from GPU. Data has to be temporarily stored in page-locked memory before it is transferred to device. By explicitly allocating the data in page locked memory it can be safely used for DMA. Allocation of data in the pinned memory can be done with `cudaHostAlloc()`. It takes the same arguments as `cudaMemcpy()` except that it has an additional argument specifying the stream index into which this command is added. A stream can be created using `cudaStreamCreate()` and destroyed using `cudaStreamDestroy()` functions.

In this paper we aim to speed up the execution of CUDA programs by overlapping kernel execution with the data transfer between CPU and GPU. Using streams, we have implemented different kinds of concurrency for the execution of a set of CUDA kernels. We compared the overlapped execution time with the time taken by the non-overlapped or serial execution. Experimental results show that execution time of CUDA applications can be decreased by simultaneously performing the transferring of data and the execution of kernel.

2. RELATED WORK

Several methods have been proposed by the researchers to speed up GPU applications. These researches mainly focus on utilizing the computational power of CPU cores in addition to the GPU for kernel execution (Raju & Chiplunkar, 2018). Among such works, application specific methods to improve the performance are presented in papers (Antoniadis & Sifaleras, 2017; Fang, Chen & Mao, 2018; Siklosi, Reguly & Mudalige, 2019; Yang, Li & Li, 2017). These parallelization approaches are based on the characteristics of individual applications and cannot be generalized.

There exist some compiler frameworks and libraries that enable the programmer to offload a portion of GPU workload to CPU cores. Frameworks like FluidiCL (Pandit & Govindarajan, 2014), JAWS (Piao et al., 2015), and SKMD (Single Kernel Multiple Device) (Lee et al., 2015) are used for the execution of OpenCL kernels using both CPU and GPU cores. OpenCL allows the programmer to select a processing device, CPU or GPU, for the execution of a given kernel. The compiler automatically generates the binary code for the selected device. Since CUDA does not provide the above feature, implementation of a co-operative execution scheme on CUDA is more complex process compared to the implementation of same on the OpenCL. Cooperative Heterogeneous Computing (CHC) (Lee et al., 2014) is a prominent cooperative execution framework for CUDA which partitions an input kernel and executes the partitions concurrently on host and device.

Only a few approaches have been reported that focus on hiding the data transfer overhead by overlapping the communication and computation. A method to minimize CPU-GPU communication overhead is suggested by (Fu, Wang & Zhai, 2017), in which two or more data transfer operations of same direction are merged into a single operation. Using compiler techniques, multiple commands for data copying are moved to same location in the source code so that these operations can be merged. Merging of data transfer operations decreases the total number of data transfer operations. Hyper-Q feature supported by NVIDIA GPUs enables concurrent execution of multiple independent kernels on a single GPU. However, when the execution of multiple kernels are not properly ordered, contention for shared

resources can degrade the overall performance (Luley & Qiu, 2016). A model has been developed by (Lázaro-Muñoz et al., 2017) that determines the order of kernel execution so as to increase the possibilities of simultaneously performing the data transfer and kernel execution, and reduce the total execution time. An analytical performance model is proposed in (Werkhoven et al., 2014) for classifying the relative performance of the different techniques for overlapping computation and communication. An approach that partitions the input data into sub-blocks and overlaps the data transfer and execution of sub-blocks in a pipelined manner is proposed in (Li et al., 2017).

Gowanlock & Karsin (2019) have developed a sorting approach in which the input data is divided into multiple batches of uniform size which are sorted on the GPU. Sorted batches are merged on the host which completes the task of sorting. The process of transferring input data and sorted batches are overlapped using CUDA streams.

A method to minimize the of GPU memory consumption for training the Convolutional Neural Networks is proposed by (Hascoet et al., 2019). In their method, the GPU memory buffers are temporarily offloaded to CPU in the forward pass and transferred back to GPU as needed by the computation during the backward pass of the backpropagation algorithm. To reduce the PCI-e bottleneck the data transfers and GPU computations are overlapped using streams.

Dhake & Walunj (2019) have used GPU to check whether input data packets contain virus signature. A string-matching algorithm parallelly checks for the occurrence of different patterns of virus string in the input packet. (Patil & Kulkarni, 2021) have investigated the performance characteristics of CPU-GPU data transfer method that is based on pinned memory.

The research works presented in (Gowanlock & Karsin, 2019; Hascoet et al., 2019; Dhake & Walunj, 2019) and (Patil & Kulkarni, 2021) make use of pinned memory and streams to overcome the PCI-e transfer overhead. In our approach, in addition to overlapping the data transfer and kernel execution we have also investigated the advantage of offloading a portion of GPU workload to CPU through an approach called as 4– way and 4+ way concurrency. With this approach, the data transfer from CPU to GPU, kernel execution, data transfer from GPU to CPU, and execution on the CPU cores can occur simultaneously.

In GPU-based graph processing systems the major challenge is that the size of the input graph is so large that it cannot be fitted into the GPU memory. To manage the problem of GPU memory oversubscription (Sabet, Zhao & Gupta, 2020) have proposed a graph processing system in which a subgraph consisting of active vertices is loaded into GPU memory. This method significantly reduces the amount of data transfer between CPU and GPU and hence minimizes the overhead of data transfer. However, this approach is specific to graph processing systems and cannot be generalized.

NVLink is an emerging CPU-GPU communication link which is faster than PCI-e. (Lutz et al., 2020) have investigated the performance of NVLink with respect to processing large data sets and observed significant speedups compared to the usage of PCI-e. However, NVLink is yet to appear in the commodity hardware.

In our approach we use CUDA streams to overlap computation and communication. The input data set is divided into chunks. The execution of a kernel associated with a chunk and transferring of next chunk are overlapped using streams. Compared to the earlier research works our approach not only overlaps kernel execution and data transfer but also offloads a portion of GPU workload to CPU cores. Thereby it reduces the GPU workload as well as the volume of data to be transferred to GPU.

3. METHODOLOGY

Any CUDA program consists of three device related operations: namely, copy the input data from CPU to GPU memory, execute the kernel, and copy the results to CPU memory from the GPU memory. Even if these three steps are added to different streams, they cannot be overlapped due to the dependency between the operations. To enable the concurrency within a data parallel kernel, we divide the data set into several smaller chunks or tiles. The data transfer and kernel execution corresponding to two adjacent tiles can be overlapped by adding them into different non-default streams. CUDA streams can support different levels of concurrency based on the order in which the commands are organized in different streams. These concurrency levels are referred to as 2-way, 3-way, 4-way, and 4+ way concurrency.

The effectiveness of different levels of concurrency are tested with the following data parallel CUDA kernels:

- Vector addition,
- Vector dot product,
- 1-D stencil operation,
- Matrix transpose,
- Matrix multiplication.

In the above kernels the vectors and matrices are of integer data type. Different levels of concurrency are applied for the execution of individual kernels and also for the combined execution of all kernels. These experiments are carried out on a system having Intel Quad-Core i5-7300HQ, 2.50 GHz, 8GB host memory, NVIDIA GTX 1050 with 640 CUDA cores, 4GB device memory, CUDA compute capability of 6.0 and CUDA SDK 9.1. The operating system is Ubuntu (12.04LTS) and the GPU driver version is 24.21.13.9891. While compiling the above kernels we have not used any optimization flags supported by NVIDIA CUDA C compiler (nvcc).

In 1-D stencil and matrix multiplication kernels, each input data element is repeatedly used in multiple computations. On the GPU, the data elements are accessed from the off-chip global memory. GPUs also possess shared memory located within the chip. Access latency shared memory is lesser than that of global memory. On GTX 1050, the global memory bandwidth is 112 Giga Bytes/second, whereas the shared memory bandwidth is above 224 Giga Bytes/second. Shared memory is used in the implementation of above two kernels. The input data elements which are repeatedly used in the computation are copied from the global to shared memory. Frequent accesses to shared memory greatly reduce the access latency, thereby reducing the execution time. Since the shared memory feature is not supported on the CPU, the implementation of above kernels on the CPU are benefited by the same.

3.1. Two-way concurrency

To enable the two-way concurrency, we have divided the input data into four tiles of equal size. These tiles are loaded from the host to the device in succession. The PCI-e transfer operations are referred to as HtoD1 through HtoD4. After the data transfers are completed, the kernel function is invoked successively four times, each time with a different tile of input data as the input parameter. The kernels are referred to as K1 through K4. After each kernel

invocation, the data transfer operation is invoked to transfer the results produced by that kernel from the device to host. These data transfer operations are referred to as DtoH1 through DtoH4. It is necessary to add a kernel invocation operation and associated GPU to CPU data transfer operation into the same non-default stream. Four different pairs of kernel launch operation and the corresponding data transfer operations are added into different streams. Hence, the GPU to CPU data copying operation for a kernel can be overlapped with the execution of another kernel as shown in Figure 5. In this approach two operations from different streams are performed in parallel. Hence, this approach is referred to as 2-way concurrency.

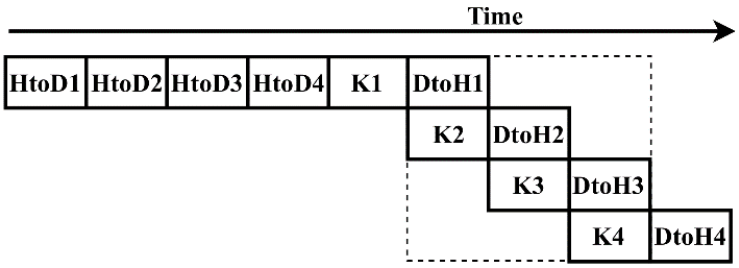

Fig. 5. 2-way concurrency

3.2. Three-way concurrency

In the previous method, kernels are launched only after all the four tiles of input data are copied from the CPU to GPU. In 3-way concurrency, the host to device data transfer for a given input data tile is followed by the corresponding kernel launch, which is then followed by the GPU to CPU data transfer of the results produced by the kernel. These three operations pertaining to a tile of input data are added to same non-default stream. The set of three operations, each pertaining to different tiles of input data are added into different non-default streams.

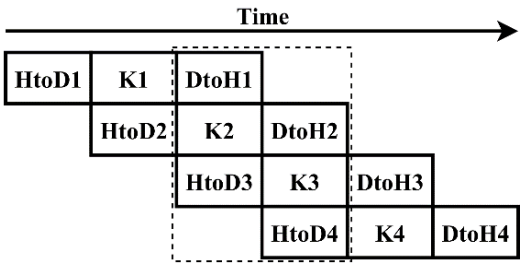

Fig. 6. 3-way concurrency

The three different operations (copying of the data from CPU to GPU, execution of the kernel, and copying of the results from GPU to CPU) corresponding to three different tiles of input data are overlapped as shown in the figure 6. Overlapping of the three operations is possible as these are issued to different CUDA streams and there exists no dependence between them.

3.3. Four-way concurrency

In the previous two concurrency approaches, the CPU cores remain idle when the kernel is being executed by the GPU. The overall execution time of the kernel can be improved if we could offload some portion of the GPU workload to CPU cores. In the 4-way concurrency approach, a portion of the input data is processed in host when the GPU is executing the kernel processing rest of the data. To process the tile allocated to the host, a routine that is functionally equivalent to the kernel is executed on the CPU. For any given application, the implementation of the CPU and GPU versions of the kernels are based on the same algorithm. Compared to OpenMP threads the thread creation and management overhead is lesser in the case of Pthreads. Hence, we have used Pthread APIs to create the CPU thread. This approach overlaps three different GPU operations and execution on the CPU as shown in figure 7. Thus, four different operations are performed simultaneously and hence the name 4-way concurrency.

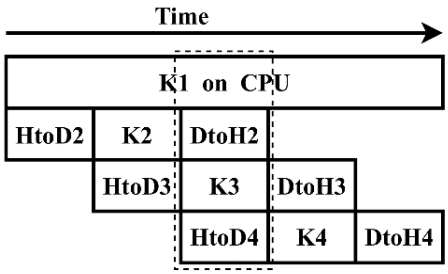

Fig. 7. 4-way concurrency

3.4. Four+ way concurrency

This type of concurrency is same as the four-way concurrency except that it uses multiple CPU threads. Each thread on the CPU can be assigned with separate tile of input data or multiple threads can be used to simultaneously process a single tile. In this way all CPU cores can be utilized for the computation. As shown in the figure 8, in the 4+way concurrency more than 4 operations can be performed in parallel.

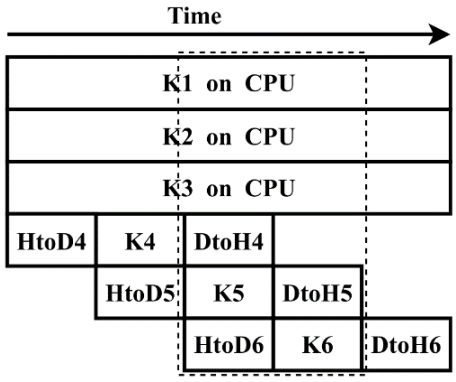

Fig. 8. 4+ way concurrency

The above different methods of concurrency can effectively decrease the time needed for the execution of a CUDA program. Moreover, even the CPU cores can also be engaged in the execution of a kernel. Hence, the overall performance of an application can be improved.

4. RESULTS AND ANALYSIS

The kernels used in our experiments are listed in section 3. The concurrency levels discussed above are applied to the execution of each individual kernel as well as the combined execution of different kernels within a single program. The results obtained from these experiments are discussed in section 4.1 and 4.2.

4.1. Applying concurrency for the execution of individual kernels

In this experiment, we have used 4 streams e for 2-way and 3-way concurrency, each one comprising of three GPU operations, namely CPU to GPU data transfer, kernel invocation, and GPU to CPU data transfer. Thus, we have executed 4 kernels, each processing the input data of uniform size. For vector-based kernels (Vector Addition, Vector Dot Product, and 1-D stencil operation), each of the kernels on different streams process a tile of 327680 integer elements. In the case of 4-way concurrency, we have used 3 streams to process three tiles of data on the GPU. The fourth tile is processed by a CPU thread. In the case of 4+ way concurrency, the fourth tile is processed in parallel by 4 different CPU threads. We have followed the same approach for matrix-based kernels (i.e. matrix transpose and matrix multiplication) also. The size of the matrix processed by each kernel and also by the CPU threads is 896×896 integer elements. Thus, for vector-based kernels the number of elements in each input vector is 1310720 elements (i.e., 5.1 MB) and for matrix-based kernels the size of each input matrix is 3211264 elements (i.e., 12.5 MB).

Tab. 1. Serial, 2, 3, and 4-way concurrent execution times (in milli seconds) for individual kernels

Kernel Name	Serial	2-way	3-way	4-way
Vector Addition	6.04	3.78	2.06	1.76
Vector Dot Product	3.31	3.21	1.78	1.42
Matrix Transpose	9.67	5.19	2.97	2.12
1-D Stencil Operation	4.57	2.28	1.28	6.77
Matrix Multiplication	73.14	68.66	62.33	4486.88

Table 1 lists the serial and concurrent execution time for the above kernels with 2, 3, and 4-way concurrency. While executing any application we have ensured that no other user applications are executing as background processes. However, we observe a slight difference in the two successive execution times of any CUDA program. This difference in execution times is attributed to the background processes of operating system. To protect the results of our experiments from this factor, each application is executed several times until no further improvement in the execution time is observed. Thus, for any application the execution time presented in this table and all the subsequent tables represent the lowest of multiple runs of the given application.

The serial execution uses the default stream as depicted in Figure 2(a). For vector addition, vector dot product, and matrix transpose, the execution time with 4-way concurrency is optimal and the speedup compared to the serial execution is 3.43, 2.33, and 4.56 respectively. These kernels involve less computation and require less time to execute. The 4+way execution time for different kernels is shown in the Table 2. The second and third columns of this table show the execution time when 2 threads and 4 threads respectively are used to process the tile allocated to the CPU. When a tile of input data is processed using multiple CPU threads, the overhead of creating multiple threads subsides the benefit of time saved by the parallelization of processing that tile on CPU. Hence, we do not observe performance gain with 4+ way concurrency either using two or four CPU threads.

Tab. 2. 4+way concurrent execution times (in milli seconds) for individual kernels

Kernel Name	2 CPU Threads	4 CPU Threads
Vector Addition	1.83	1.84
Vector Dot Product	1.47	1.54
Matrix Transpose	2.41	2.65
1-D Stencil Operation	3.65	2.15
Matrix Multiplication	2535.96	1387.31

Tab. 3. GPU-only and CPU-only execution time of individual kernels

Kernel Name	GPU Execution Time (milli seconds)	CPU Execution Time (milli seconds)
Vector Addition	1.33	1.02
Vector Dot Product	0.69	1.07
1-D Stencil	1.03	6.87
Matrix Transpose	2.27	3.73
Matrix Multiplication	20.07	95152.0

The CPU-only execution time for matrix multiplication and stencil operation is much higher than that of GPU-only time as shown in Table 3. This is due to the fact that these two kernels are computation intensive compared to the rest of the kernels. As GPUs consist of large number of cores, compared to the multicore CPUs they exhibit optimal performance for compute intensive data parallel kernels. Hence, as shown in the Table 3, for the above two kernels and even for any other kernels the GPU-only execution time is much lesser than the CPU-only time. The vast difference between the CPU-only and GPU-only time of matrix multiplication is also due to the fact that the algorithm used for multiplication on the CPU is not cache friendly. The simple matrix multiplication operation to multiply matrices A and B to produce matrix C is defined as $c_{ij} = \sum_{k=1}^{n} a_{ik}\, b_{kj}$, where A, B, and C are m×n, n×p, and m×p matrices respectively. The above method of multiplying two matrices can be implemented using three level nested loops. If we consider all matrices to be of order n×n, the size of the cache is B bytes, and the size of a cache line is b bytes, then the cache consists of $\frac{B}{b}$ cache lines. C-language stores matrices in row major order. When the inner loop accesses an element of matrix B, a cache line containing that element must be available in

the cache. According to the algorithm, the inner loop accesses only one element from that cache line. When $n > \frac{B}{b}$, every access to matrix B causes a cache miss. The algorithm results in $\theta(n^3)$ cache misses in the worst case.

GPU provides shared memory which has higher bandwidth than the global memory. We use tile-based algorithm for the matrix multiplication algorithm on the GPU. In this algorithm, a row of matrix A and a column of matrix B is accessed by different threads of a thread-block. By placing the tile containing these rows and columns in the shared memory, repeated long latency global memory accesses can be avoided. Moreover, when the threads of a warp access adjacent elements in the shared memory, GPU can coalesce these different accesses into a single access. Due to these features, the performance of matrix multiplication algorithm on GPU is significantly better than the performance of the same on the CPU. Hence, the 4-way and 4+way concurrencies which offload matrix multiplication workload to CPU increase the execution time compared to the 2-way and 3-way concurrencies which use only GPU.

Therefore, as shown in Table 1, the 3-way concurrency proves to be ideal for 1-D stencil operation and matrix multiplication with a speedup of 3.57 and 1.17 *respectively* compared to the serial execution. However, with 4+way concurrency it can be observed that for both kernels the execution time decreases as the number of CPU threads are increased based on the number of cores available. The decrease in the execution time in this case is attributed to distribution of huge amount of computational load among multiple threads.

4.2. Applying concurrency for the combined execution of different kernels

In this experiment we have overlapped the kernel execution and data transfer operations of five different kernels. Size of the vector for a vector-based application is 327680 elements and the size of the matrix for a matrix-based application is 896×896 elements. Table 4 shows the combined execution time with serial execution, 2-way, and 3-way concurrent execution of 5 different kernels. Compared to the serial execution (using default stream), the 2-way and 3-way concurrency results in a speedup of 1.15 and 1.28 respectively.

Tab. 4. Combined execution time of all kernels with serial execution, 2, and 3-way concurrency

Level of concurrency	Execution Time (in milli seconds)
1-way (single stream)	25.63
2-way	22.33
3-way	20.03

The performance of 4-way concurrency is tested by executing 4 different kernels on the GPU and remaining one on the CPU. In this way, the execution time for five different combinations of kernels are tested. Table 5 lists the execution time for the same. Except for matrix multiplication, speedup is observed when any of the kernel is executed on the CPU and rest are executed on the GPU. The speedup is calculated with respect to the serial execution time (i.e. 25.63ms). As discussed, GPU is suitable for matrix multiplication compared to CPU. Hence executing it on the CPU will not improve the performance.

The 4+ way concurrency is realized by executing vector addition and matrix transpose kernels on the host and the remaining 3 kernels on the device. These two kernels are chosen for execution on the host as their execution time on the host is minimum as shown in the Table 5. The two kernels on the host are executed in parallel by separate threads. Execution time for the above combination of 4+ way concurrency is 19.16 milliseconds which is slightly better than the execution time of matrix transpose kernel executed on the CPU using 4-way concurrency (i.e. 19.45 milliseconds).

Tab. 5. Combined execution time of all kernels with 4-way concurrency

Kernel on the CPU	Execution time (in milli seconds)	Speedup
Vector Addition	19.71	1.3
Vector Dot Product	20.43	1.25
1-D Stencil	20.05	1.28
Matrix Transpose	19.45	1.32
Matrix Multiplication	96169.88	0.0003

5. CONCLUSIONS

CUDA streams enable the overlapping of CPU-GPU communication and execution of kernel. The results of applying concurrency for the execution of individual kernels and combination of different kernels show a significant improvement in the execution time over serial or non-overlapped execution. However, while applying 4-way or 4+ way concurrency care must be taken so that the CPU thread creation overhead does not dominate the performance benefits of offloading the workload to CPU. In this regard, this work can be extended to device a mechanism that can dynamically select a suitable amount workload for the CPU based on its hardware features and the computational characteristics of the given application.

REFERENCES

Antoniadis, N., & Sifaleras, A. (2017). A hybrid CPU-GPU parallelization scheme of variable neighborhood search for inventory optimization problems. *Electronic Notes in Discrete Mathematics*, *58*, 47–54. https://doi.org/10.1016/j.endm.2017.03.007

Dhake, A.A., & Walunj, S.M. (2019). Transfer Time Optimization Between CPU and GPU for Virus Signature Scanning. In A. Luhach, D. Jat, K. Hawari, X.Z. Gao & P. Lingras (Eds.), *Advanced Informatics for Computing Research. ICAICR 2019. Communications in Computer and Information Science* (vol. 1076 pp. 70–78). Springer Singapore. https://doi.org/https://doi.org/10.1007/978-981-15-0111-1_6

Fang, J., Chen, H., & Mao, J. (2018). Understanding data partition for applications on CPU-GPU integrated processors. In *Communications in Computer and Information Science* (vol. 747). Springer Singapore. https://doi.org/10.1007/978-981-10-8890-2_32

Fu, C., Wang, Z., & Zhai, Y. (2017). A CPU-GPU Data Transfer Optimization Approach Based on Code Migration and Merging. *Proceedings - 2017 16th International Symposium on Distributed Computing and Applications to Business, Engineering and Science, DCABES 2017, 2018-Septe* (pp. 23–26). IEEE. https://doi.org/10.1109/DCABES.2017.13

Gowanlock, M., & Karsin, B. (2019). A hybrid CPU/GPU approach for optimizing sorting throughput. *Parallel Computing*, *85*, 45–55. https://doi.org/10.1016/j.parco.2019.01.004

Gregg, C., & Hazelwood, K. (2011). Where is the Data ? Why You Cannot Debate CPU vs. GPU Performance Without the Answer. *IEEE International Symposium on Performance Analysis of Systems and Software*. (pp. 134–144). IEEE. https://doi.org/10.1109/ISPASS.2011.5762730

Hascoet, T., Zhuang, W., Febvre, Q., Ariki, Y., & Takiguchi, T. (2019). Reducing the Memory Cost of Training Convolutional Neural Networks by CPU Offloading. *Journal of Software Engineering and Applications*, *12*(08), 307–320. https://doi.org/10.4236/jsea.2019.128019

Huang, W., Yu, L., Ye, M., Chen, T., & Hu, T. (2012). A CPU-GPGPU scheduler based on data transmission bandwidth of workload. *Parallel and Distributed Computing, Applications and Technologies, PDCAT Proceedings* (pp. 610–613). IEEE. https://doi.org/10.1109/PDCAT.2012.15

Lázaro-Muñoz, A.J., González-Linares, J.M., Gómez-Luna, J., & Guil, N. (2017). A tasks reordering model to reduce transfers overhead on GPUs. *Journal of Parallel and Distributed Computing*, *109*, 258–271. https://doi.org/10.1016/j.jpdc.2017.06.015

Lee, C., Woo, W.R., & Gaudiot, J. (2014). Boosting CUDA Applications with CPU – GPU Hybrid Computing. *International Journal of Parallel Programming*, *42*, 384–404. https://doi.org/10.1007/s10766-013-0252-y

Lee, J., Samadi, M., Park, Y., & Mahlke, S. (2015). SKMD: Single kernel on multiple devices for transparent CPU-GPU collaboration. *ACM Transactions on Computer Systems*, *33*(3). https://doi.org/10.1145/2798725

Li, T., Dong, Q., Wang, Y., Gong, X., & Yang, Y. (2017). Dual buffer rotation four-stage pipeline for CPU – GPU cooperative computing. *Soft Computing*, *23*, 859–869. https://doi.org/10.1007/s00500-017-2795-0

Luley, R.S., & Qiu, Q. (2016). Effective utilization of CUDA hyper-Q for improved power and performance efficiency. *Proceedings – 2016 IEEE 30th International Parallel and Distributed Processing Symposium, IPDPS 2016* (pp. 1160–1169). IEEE. https://doi.org/10.1109/IPDPSW.2016.154

Lutz, C., Breß, S., Zeuch, S., Rabl, T., & Markl, V. (2020). Pump Up the Volume: Processing Large Data on GPUs with Fast Interconnects. *Proceedings of the ACM SIGMOD International Conference on Management of Data* (pp. 1633–1649). ACM Digital Library. https://doi.org/10.1145/3318464.3389705

NVIDIA TITAN V. (n.d.). *NVIDIA Corporation*. Retrieved May 8, 2021 from https://www.nvidia.com

NVIDIA. (2015). *CUDA C Programming Guide v 9.1*. NVIDIA.

Pandit, P., & Govindarajan, R. (2014). Fluidic kernels: Cooperative execution of openCL programs on multiple heterogeneous devices. *Proceedings of the 12th ACM/IEEE International Symposium on Code Generation and Optimization, CGO 2014* (pp. 273–283). ACM Digital Library. https://doi.org/10.1145/2544137.2544163

Patil, S.V., & Kulkarni, D.B. (2021). Data transfer optimization in CPU/GPGPU Communication. *Turkish Journal of Computer and Mathematics Education*, *12*(13), 1920–1923.

Piao, X., Kim, C., Oh, Y., Li, H., Kim, J., Kim, H., & Lee, J.W. (2015). JAWS: A JavaScript framework for adaptive CPU-GPU work sharing. *Proceedings of the ACM SIGPLAN Symposium on Principles and Practice of Parallel Programming, PPOPP, 2015-Janua* (pp. 251–252). ACM Digital Library. https://doi.org/10.1145/2688500.2688525

Raju, K., & Chiplunkar, N.N. (2018). A survey on techniques for cooperative CPU-GPU computing. *Sustainable Computing: Informatics and Systems*, *19*, 72–85. https://doi.org/10.1016/j.suscom.2018.07.010

Sabet, A.H.N., Zhao, Z., & Gupta, R. (2020). Subway: Minimizing data transfer during out-of-GPU-memory graph processing. *Proceedings of the 15th European Conference on Computer Systems, EuroSys 2020* (pp. 1–16). ACM Digital Library. https://doi.org/10.1145/3342195.3387537

Siklosi, B., Reguly, I.Z., & Mudalige, G.R. (2019). Heterogeneous CPU-GPU execution of stencil applications. *Proceedings of P3HPC 2018: International Workshop on Performance, Portability and Productivity in HPC, Held in Conjunction with SC 2018: The International Conference for High Performance Computing, Networking, Storage and Analysis* (pp. 71–80). IEEE. https://doi.org/10.1109/P3HPC.2018.00010

Werkhoven, B. Van, Maassen, J., Seinstra, F.J., & Bal, H.E. (2014). Performance models for CPU-GPU data transfers. *Proceedings – 14th IEEE/ACM International Symposium on Cluster, Cloud, and Grid Computing, CCGrid 2014* (pp. 11–20). IEEE. https://doi.org/10.1109/CCGrid.2014.16

Yang, W., Li, K., & Li, K. (2017). A hybrid computing method of SpMV on CPU–GPU heterogeneous computing systems. *Journal of Parallel and Distributed Computing*, *104*, 49–60. https://doi.org/10.1016/j.jpdc.2016.12.023

Applied Computer Science, vol. 17, no. 3, pp. 19–30
doi: 10.23743/acs-2021-18

Submitted: 2021-06-19 | Revised: 2021-09-13 | Accepted: 2021-09-21

Breast Cancer Diagnosis, Feature Selection, Neural Network, Grid Search, Machine Learning

Nawazish NAVEED [0000-0002-9619-4799]*,
Hayan T. MADHLOOM [0000-0002-6228-5721]*,
Mohd Shahid HUSAIN [0000-0003-4864-9485]*

BREAST CANCER DIAGNOSIS USING WRAPPER-BASED FEATURE SELECTION AND ARTIFICIAL NEURAL NETWORK

Abstract

Breast cancer is commonest type of cancers among women. Early diagnosis plays a significant role in reducing the fatality rate. The main objective of this study is to propose an efficient approach to classify breast cancer tumor into either benign or malignant based on digitized image of a fine needle aspirate (FNA) of a breast mass represented by the Wisconsin Breast Cancer Dataset. Two wrapper-based feature selection methods, namely, sequential forward selection(SFS) and sequential backward selection (SBS) are used to identify the most discriminant features which can contribute to improve the classification performance. The feed forward neural network (FFNN) is used as a classification algorithm. The learning algorithm hyper-parameters are optimized using the grid search process. After selecting the optimal classification model, the data is divided into training set and testing set and the performance was evaluated. The feature space is reduced from nine feature to seven and six features using SFS and SBS respectively. The highest classification accuracy recorded was 99.03% with FFNN using the seven SFS selected features. While accuracy recorded with the six SBS selected features was 98.54%. The obtained results indicate that the proposed approach is effective in terms of feature space reduction leading to better accuracy and efficient classification model.

1. INTRODUCTION

Breast cancer is the most common cancer among women. it is also considered as the second most common cancer worldwide (Dhungel, Carneiro & Bradley, 2015). Early detection and accurate diagnosis of breast cancer can tremendously contribute to the reduction of fatality rate and remarkably important for the reduction of its morbidity and mortality (Addeh, Demirel & Zarbakhsh, 2017; Moodley et al., 2018). A cost-effective computer-aided detection/diagnosis technique can play a crucial part in reducing interpretation error and provide an automated diagnosis of breast cancer. this can hugely assist physicians

* University of Technology and Applied Sciences, CAS-Ibri, Dept. of IT, Sultanate of Oman, nawazish.ibr@cas.edu.om, hayan.ibr@cas.edu.om, mshahid.ibr@cas.edu.om

by providing a second opinion which can ease the process of making the final decision. In this work, artificial neural network is used to build a classification model for breast cancer diagnosis based on fine needle aspiration modality. The main purpose is to correctly recognize the sample type as either benign or malignant. The Wisconsin breast cancer dataset (WBCD) is used for training and testing the proposed model. The accuracy of the classifier highly depends on the features used for classification. We have used the wrapper feature selection to extract the most useful features for the diagnosis purpose. Our approach shows encouraging results and can be developed in a fully automated cad system.

2. RELATED WORKS

Several researchers studied the performance of various prediction algorithms in classifying breast cancer data. (Senturk & Kara, 2014) compared the performance of seven different classification algorithms on the WBCD including discriminant analysis, artificial neural network (ANN), decision tree, logistic regression, support vector machine (SVM), Naïve Bayes (NB), and k-nearest neighbor (KNN). these algorithms were tested on all the nine features provided in the dataset. the best performance was obtained using the SVM with accuracy of 96.5%. another study (Barna & Khan, 2019) conducted to test the performance of six different classifiers, namely, logistic regression, linear discriminant analysis (LDA), quadratic discriminant analysis (QDA), KNN, NB and ANN. the researchers concluded that the ANN outperformed the other classifiers when the data was separated in to training and testing with the ratio of 75:25. the reported accuracy of ANN was 97.21%.

The work presented by (Vijayalakshmi & Priyadarshini, 2017) focused on using neural network to classify breast cancer tumors. The effectiveness of two different neural networks were compared, namely, the Radial Basis Function (RBF), and the back-propagation neural (BPN). It was found that the RBF neural network achieved higher accuracy than the BPN. The RBF accuracy was 98.26% while the BPN was 90.42%.

Khan et al. (2019) proposed a novel embedded approach based on accelerated particle swarm optimization and cuckoo search named HACPSO. Along with other datasets, they tested their approach on Wisconsin Breast Cancer dataset and achieved 98.08% classification accuracy that outclass the existing methods. Mushtaq et al. (2019) compared five different classification algorithms combined with principle-component analysis (PCA) to classify breast cancer tumor. The highest accuracy of 99.20% was obtained with sigmoid based NB classifier.

Kumar studied (Kumar, 2021) the performance of seven different classifiers (logistic regression, KNN, decision tree, SVM, Naïve Bayes, random forest and ANN) and reported that KNN is the best classifier with 97% accuracy and decision tree classifier is the worst performer with 94% accuracy for breast cancer diagnosis. Another study (Islam et al., 2020) reported that ANN is the best classifier in terms of accuracy (98.57%), and precision (97.82%) compare to SVM, KNN, logistic regression and random forest when tested on WBCD.

In the above mentioned studies, the authors focused on comparing the performance of various classification algorithms without giving importance to find the best feature subset. It was assumed that all the features are equally important for the classification, hence, no feature selection was performed. In medical application especially in cancer classification

related problems, it is quite significant to find the best feature subset and also to understand the features dependencies. This will help the domain experts to understand the most effective tumor characteristics and the relationship between them.

On the other hand, some other studies used feature selection methods to find the best attributes which can produce the highest discrimination results. A rule based classification system with PCA was proposed by (Douangnoulack & Boonjing, 2018). Only 7 features were used for the classification and the J48 classifier achieved the accuracy of 97.36% on the WBCD. Kumari & Singh (2018) proposed a system for the prediction of breast cancer. A combination of feature selection using Correlation-Based Measures with classification using several algorithms including linear Regression (LR), SVM, and KNN algorithm. The validation was performed using 10-fold cross validation and the accuracy of the model was 99.2%. Nevertheless, the optimal feature subset was not reported.

Ed-Daoudy & Maalmi (2020) applied Association Rules (AR) to eliminate irrelevant features in the WBCD. Four out of nine features were selected. Several classification algorithms were used. The support vector machine with threefold cross-validation produced the highest classification accuracy (98.00%).

3. MATERIALS AND METHODS

3.1. Wisconsin breast cancer dataset

The Wisconsin breast cancer database (WBCD) was created by Dr. Wolberg from the University of Wisconsin Hospitals and was donated and made publicly available online by Mangasarian (WBCD, 1995). The data was collected over a period of two years starting from 1989 until 1991, and it is used as a standard dataset for classification and other machine learning purposes by several researchers. It represents the observations of breast mass cell nuclei obtained by a fine-needle aspiration modality. The cytological samples were converted into digital images in order to extract the characteristics of the cell nuclei using image processing techniques.

Fine needle aspiration (FNA) is a type of biopsy procedure. Basically, it is one of the various modalities used in the process of breast masses diagnosis. In this procedure a small needle (21 to 25 gauge) is used to acquire a sample of the tissue and fluid from the breast (Casaubon, Tomlinson-Hansen & Regan, 2020) Total number of 699 samples are available in the WBCD, each sample represented by nine different nuclei features. Furthermore, the diagnosis of each sample as a benign or malignant was also provided in the dataset. 458/699 observations were flagged as benign, while 241/699 were flagged as malignant. The details and the names of the feature set are described in Tab. 1. Each feature has a grade between 1 and 10, where the value 1 indicates that the feature is in most normal condition and the value 10 indicates most abnormal condition.

It has been noticed that there are 16 observations with missing values. All the missing values are related to the Bare Nuclei feature. 15 samples are from the benign class, and one sample is from the malignant class. Since the number of missing values are small and in the interest of maintaining data consistency, these 16 samples were removed.

Tab. 1. Dataset details with feature names

Feature Index	Feature Name	Value Range	$\mu \pm \sigma$
1	Clump thickness	1–10	3.42±2.82
2	Uniformity of cell size	1–10	3.13±3.05
3	Uniformity of cell shape	1–10	3.20±2.97
4	Marginal adhesion	1–10	2.80±2.86
5	Single epithelial cell size	1–10	3.21±2.21
6	Bare nuclei	1–10	3.46±3.64
7	Bland chromatin	1–10	3.43±2.44
8	Normal nucleoli	1–10	2.87±3.05
9	Mitoses	1–10	1.59±1.71

3.2. Feature Selection

Feature selection is a commonly used data preprocessing procedure in data classification. It is mainly used for reducing and eliminating irrelevant and redundant attributes from any dataset (Tang, Alelyani & Liu, 2014; Foithong, Srinil & Pinngern, 2017). Additionally, it plays a significant role in enhancing data comprehensibility, data visualization as well as reducing the time to train a classification model, and improves the prediction results (Jain & Singh, 2018).

There exist numerous applications of relevant feature identification techniques in healthcare sector. Filter methods, wrapper methods, ensemble methods and embedded methods are some of the popularly used techniques used for variable selection (Kohavi & John, 1997; Guyon et al., 2008).

In this paper two wrapper feature selection methods are used, namely, the sequential forward selection (SFS) and the sequential backward feature (SBS) selection. The wrapper feature selection methods outperform other existing methods such as filter methods. It finds the most ‘‘useful” features and does optimal selection of features for the learning algorithm (Kumar & Minz, 2014); furthermore, the wrapper methods give more accurate results as it considers the features dependencies (Ang et al., 2015). It has been stated that the Naïve-Bayes learning algorithm is robust when it is used to remove noisy features (Kohavi & John, 1997). This is because the performance of the Naïve-Bayes degrades very slowly as more irrelevant features are added (Kohavi & John, 1997). For that reason, the Naïve-Bayes learning algorithm is used with both SFS and SBS.

In this research, the ultimate goal of performing the feature selection process is not limited to obtaining the highest classification accuracy. However, it is also related to the detection of the most clinically significant features as this optimal set of features can help the specialist objectively focus on these features during a routine manual diagnosis process.

Both SFS and SBS are iterative methods. The SFS starts with an empty set and in each iteration a new unseen feature is added. For each added feature, performance is evaluated using the induction algorithm. Only the feature producing the highest increase of performance is added to new feature subset. Then a new iteration is started with the new generated subset. On the other hand, the SBS starts with full feature set and at each iteration one feature is removed. In both methods the searching process stops when there is no further improvement is detected by the induction algorithm. Fig. 1 illustrates the feature selection process.

According to Fig. 1, the feature selection process for both SFS and SBS starts by generating a feature subset. The performance of the subset is evaluated with Naïve-Bayes using 10-fold cross validation process. For each subset, if the induction algorithm performance increase, the final optimal feature subset is updated. The process continues to evaluate the features until no further enhancement in the performance detected.

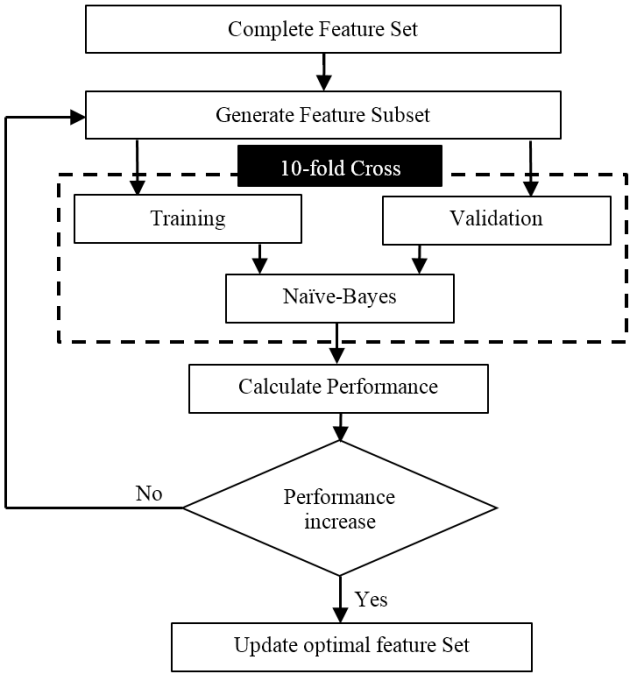

Fig. 1. Feature Selection Process

3.3. Classification

In this research, the ANN is used to classify the breast cancer samples in the WBCD into either benign or malignant. ANN was used intensively in the diagnosis and classification of many medical conditions such as leukemia (Wahhab, 2015), prostate cancer (Wu, Zhuang & Tan, 2020), lung cancer (Hsu et al., 2020), liver cancer (Patsadu, Tangchitwilaikun & Lowsuwankul, 2021) and many others. There are various ANN architectures (Agrawal & Agrawal, 2015). However, one of the most widely used is the multilayer feed-forward neural network (FFNN) with a back-propagation learning algorithm (Zarei et al., 2020). In FFNN, there are a number of parameters need to be tuned in order to obtain the best classification performance. These parameters include the number of hidden layers, the activation function, the number of neurons, the learning rate, and the epochs. The number of hidden layer is set to one as usually single hidden layer is sufficient for various kinds of classification problem (Guliyev & Ismailov, 2018). Regarding the activation function, in fact, there are many options available. Nevertheless, previous researches (Bonakdari et al., 2020; Shenouda, 2006) have established that the sigmoid activation function produced a better result in medical and non-medical applications compared to other activation functions. Hence, for this experiment, the sigmoid activation function is chosen.

The rest of the FFNN hyper-parameters is tuned with the grid search optimization using 10-fold cross validation. The grid search algorithm traverses a given combination of parameters. Later, the parameters resulted in the best performance can be used to train the final model and tested using the test set. In grid search the performance of the model is verified using a statistical method called cross validation (CV) (Liu at al., 2017). The cross validation divides the dataset into two parts, namely, training and validation. On each hyper-parameter combination, the FFNN is trained and the accuracy is verified. Eventually, the model which produced the highest performance is used for the final classification test. Tab. 2 presented the range of each hyper-parameter used in the optimization process.

Tab. 2. Hyper-parameters values

Hyper-parameter	Values
Learning rate	[0.001, 0.01, 0.1]
Number of neurons in the hidden layer	[2,4,6,8,10, 12, 14]
Training cycle	Max(2000)

3.4. Performance Measure

The performance of the proposed breast cancer classification model is evaluated using the confusion matrix. It is used to calculate true positive (TP), true negative (TN), false positive (FP) and false negative (FN). Accuracy is the most empirical metric used to assess effectiveness of a classifiers. Other important metrics are the precision and recall. The precision is calculated as the correct positive prediction over all the samples classified as positive, while recall is used to test the classifier ability to identify the positive cases. These metrics are calculated as follow:

$$Accuracy = \frac{TP+TN}{TP+TN+FP+FN} \tag{1}$$

$$Precision = \frac{TP}{TP+FP} \tag{2}$$

$$Recall = \frac{TP}{TP+FN} \tag{3}$$

4. RESULTS AND DISCUSSION

The proposed work is performed in three folds, first, the best features were selected using two wrapper methods, namely, sequential forward selection and sequential backward selection. Second, the hyper-parameters optimization using grid search, and finally the FFNN training and testing with optimal set of features. The feature selection and classification analysis were performed using RapidMiner. RapidMiner is an open-source data mining and machine learning tool and it provides the largest coverage of healthcare data mining requirements compared to other tools such as R, Scikit-learn and Spark (Santos-Pereira, Gruenwald & Bernardino, 2021).

From the data presented in Fig. 2, it can be seen that both wrapper methods performance is equal at feature number 3 and feature number 5. However, the optimal performance of SFS was obtained at 7th feature. On the other hand, the SBS reached its highest performance at the 6th feature. The best selected features for both methods are listed in Tab. 3.

Based on this result, the top 7 features selected using SFS were utilized to construct the FFNN model.

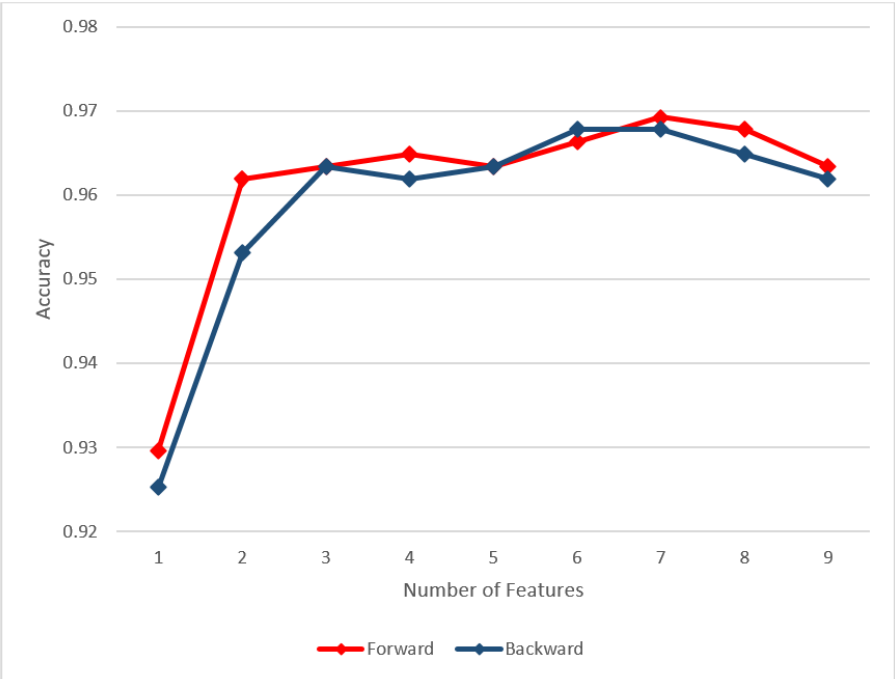

Fig. 2. SFS and SBS performance

Tab. 3. The best feature subset selected using SFS and SBS

Feature Index	Optimal Features (SFS)	Optimal Features (SBS)
F1	Bare Nuclei	Bare Nuclei
F2	Normal Nucleoli	Normal Nucleoli
F3	Clump Thickness	Clump Thickness
F4	Uniformity of Cell Shape	Uniformity of Cell Shape
F5	Bland Chromatin	Bland Chromatin
F6	Marginal Adhesion	Marginal Adhesion
F7	Uniformity of Cell Size	

During the grid search optimization, 18 FFNN architecture was trained and validated using 10-fold cross validation. Each architecture was constructed with different set of parameters as mentioned in Tab. 3.

As shown in Fig. 3, the best result was obtained when number of neurons in the hidden layer was equal to 6 and learning rate equal to 0.01 with 100 epochs.

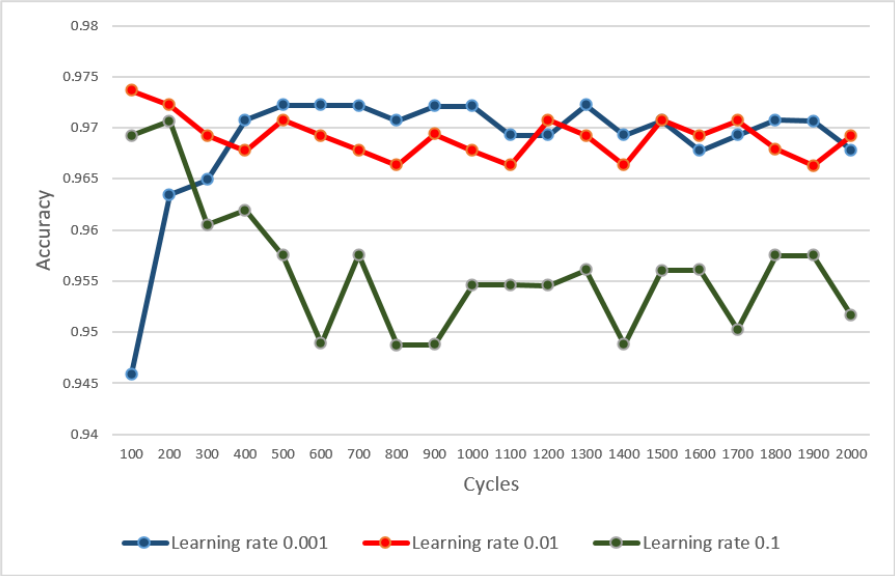

Fig. 3. The performance of the three different learning rates with six hidden neurons

After finding the optimal hyper-parameters, the original dataset was divided into two sets, the training set and the test set with the ratio of 70% for training and 30% for testing. Based on that, and in order to compare the classification results obtained using both feature selections methods, the classification experiment was performed twice. The first experiment considered the 7 features selected using SFS, whilst, the second experiment was performed on the 6 features selected using SBS. The final classification results are presented in Tab. 4, and Tab. 5.

It is apparent from the data presented in Tab. 4 that the FFNN classification performance using both feature subsets obtained using SFS and SBS is almost the same as in both experiments all the benign instances were correctly classified. Nevertheless, there is a slight difference in the classification result of the malignant instances. The SFS subset resulted in classifying 69 malignant instances out or 71, whereas the SBS subset wrongly classify 3 malignant instances as benign.

Tab. 4. Classification results with SFS and SBS feature subsets

Experiments	Correctly classified instances	Incorrectly classified instances	TP	TN	FP	FN
SFS + FFNN (7 Features)	204	2	69	135	0	2
SBS + FFNN (6 Features)	203	3	68	135	0	3

As illustrated in Tab. 5, The overall classification accuracy of FFNN using the SFS features subset is outperformed the accuracy obtained using the SBS features subset. In the first experiment the accuracy was 99.03 % with 100% precision and 97.18% recall. While in the second experiment the accuracy was 98.54 % with 100% precision and 95.77% recall.

Tab. 5. Performance evaluation of FFNN with SFS and SBS feature subsets

Experiments	Accuracy (%)	Precision (%)	Recall (%)
SFS + FFNN (7 Features)	99.03	100	97.18
SBS + FFNN (6 Features)	98.54	100	95.77

As shown in Tab. 4, the first experiment classified 2 malignant cases as benign and in the second experiment there are 3 malignant cases classified as benign. Although the number of misclassified instances are insignificant, in medical application classifying an unhealthy case as healthy is more dangerous than classifying healthy case as unhealthy. This is because in the latter situation the patient can undergo further investigation and then the misclassification can be ruled out.

In our experiment, the reason of getting misclassified instances could be due to the imbalance data distribution of the WBCD as the ratio of majority (benign) to minority (malignant) is approximately 1:2. The number of benign instances used in the training phase (309) is almost double in size compared to the number of malignant instances (168). Although the majority to minority ratio is not tremendously high, the possibility of the learning algorithm overwhelmed by the majority class could not be ruled out. Nevertheless, the proposed approach to classify breast cancer provides an outstanding accuracy with high precision and recall in comparison with the previous experimental results in the literature. Moreover, the proposed approach identified the optimal discriminative set of features using the SFS feature selection algorithm. It has been found that the two features, namely, Single epithelial cell size and Mitoses are not contributing to the diagnosis of breast cancer using the fine-needle aspiration modality.

In the literature, several methods have been proposed for the diagnosis of breast cancer based on the WBCD. Tab. 6 demonstrates the classification accuracy achieved by previous studies compared to our proposed approach.

Tab. 6. Comparison of the proposed method with previous researches in the literature

Authors	Feature Selection Reduction	No of feature selected	Classification method	Reported Accuracy (%)
(Vijayalakshmi & Priyadarshini, 2017)	Not Reported	Not Reported	RBF neural network	98.26
(Yi & Yi, 2017)	Pearson chi-square test	4	Decision Tree	94.30
(Douangnoulack & Boonjing, 2018)	PCA	7	Decision Tree (J48)	97.36
(Kumari & Singh, 2018)	Pearson's linear correlation	Not Reported	KNN	99.28
(Mushtaq et al., 2019)	Not Reported	Not Reported	Naïve Bayes with sigmoid PCA	99.20
(Ed-daoudy & Maalmi, 2020)	association rules	4	SVM	98.00
Proposed Approach	SFS	7	FFNN	99.03

It can be seen that the proposed method outperformed many of the works previously done. On the other hand, the work performed by (Kumari & Singh, 2018; Mushtaq et al., 2019) achieved slightly higher accuracy at 99.28 and 99.2 respectively compared to the proposed method. However, both research works did not focus on finding the most clinically significant. Furthermore, the number of selected features are not reported. Most of the feature selection methods used in the previous experiments focused on filter feature selection methods. Usually filter methods do not consider dependencies between the features. However, in this research the SFS and SBS are used to get the optimal subset of features. The main advantage of these methods is that it will take the interaction between the features into consideration. One interesting finding is that a well optimized FFNN architecture can produce better classification accuracy compared to some of the most popular machine learning algorithms such as SVM and J48.

It is worth mentioning that in medical application especially in cancer classification related problems, it is highly important to select the best set of features that can produce the optimal model performance. This will help the domain experts to understand the most effective tumor characteristics and the relationship between them.

5. CONCLUSION

Data mining and machine learning techniques are extensively used to explore patterns in medical data, which can be used for many purposes such as diagnosis and prognosis. Many researches have been conducted in the medical field to accurately diagnose several diseases such as cancer. One of the most important step in the context of computer-aided diagnosis is features reduction. Certainly, there are some features non-informative and redundant features. These features make the classification algorithms ineffective. Hence, features selection will considerably enhance the performance of the classification algorithm.

In this research, an approach to classify breast cancer based on FNA modality has been proposed. Feature selection is a prominent process used for improving the overall classification accuracy as well as understanding the tumor characteristics. In this work, two wrapper feature selection methods, namely, the SFS and SBS were used to extract the optimal subset of tumor attributes. Using SFS, seven important features have been identified from the original nine feature set. Afterward, the FFNN classifier was optimized, trained and tested on the WBCD. The proposed approach performance is evaluated and compared with other previous works. The seven features selected using SFS produced the highest accuracy of 99.03. This research demonstrated wrapper feature selection methods such as SFS can be used for removing the less important features and the proposed FFNN model can be used to obtain efficient automatic diagnostic systems.

Acknowledgment

This work is part of a research project(DSR_IRPS_2019-20_PROP_4) supported by the University of Technology and Applied Science, CAS-Ibri.

REFERENCES

Addeh, A., Demirel, H., & Zarbakhsh, P. (2017). Early detection of breast cancer using optimized ANFIS and features selection. *2017 9th International Conference on Computational Intelligence and Communication Networks (CICN)* (pp. 39–42). IEEE. http://doi.org/10.1109/CICN.2017.8319352

Agrawal, S., & Agrawal, J. (2015). Neural network techniques for cancer prediction: A survey. *Procedia Computer Science*, *60*, 769–774. http://doi.org/10.1016/j.procs.2015.08.234

Ang, J. C., Mirzal, A., Haron, H., & Hamed, H. N. A. (2015). Supervised, unsupervised, and semi-supervised feature selection: a review on gene selection. *IEEE/ACM transactions on computational biology and bioinformatics*, *13*(5), 971–989. http://doi.org/10.1109/TCBB.2015.2478454

Barna, S. D., & Khan, S. (2019). Performance Evaluation of Classification Learning Models for Wisconsin Breast Cancer Data Repository. *7th International Conference on Data Science and SDGs: Challenges, Opportunities and Realities* (EC-50). Bangladesh.

Bonakdari, H., Moradi, F., Ebtehaj, I., Gharabaghi, B., Sattar, A. A., Azimi, A. H., & Radecki-Pawlik, A. (2020). A Non-Tuned Machine Learning Technique for Abutment Scour Depth in Clear Water Condition. *Water*, *12*(1), 301. http://doi.org/10.3390/w12010301

Casaubon, J. T., Tomlinson-Hansen, S., & Regan, J.-P. (2020). *Fine Needle Aspiration of Breast Masses. StatPearls*. StatPearls Publishing.

Dhungel, N., Carneiro, G., & Bradley, A. P. (2015). Automated Mass Detection in Mammograms Using Cascaded Deep Learning and Random Forests. *International Conference on Digital Image Computing: Techniques and Applications (DICTA)* (pp. 1–8). IEEE. http://doi.org/10.1109/DICTA.2015.7371234

Douangnoulack, P., & Boonjing, V. (2018). Building Minimal Classification Rules for Breast Cancer Diagnosis. *2018 10th International Conference on Knowledge and Smart Technology (KST)* (pp. 278–281). IEEE. http://doi.org/10.1109/KST.2018.8426198

Ed-Daoudy, A., & Maalmi, K. (2020). Breast cancer classification with reduced feature set using association rules and support vector machine. *Network Modeling Analysis in Health Informatics and Bioinformatics*, *9*(1), 34. http://doi.org/10.1007/s13721-020-00237-8

Foithong, S., Srinil, P., & Pinngern, O. (2017). Min-Uncertainty & Max-Certainty Criteria of Neighborhood Rough-Mutual Feature Selection. *Walailak Journal of Science and Technology*, *14*(4).

Guliyev, N. J., & Ismailov, V. E. (2018). On the approximation by single hidden layer feedforward neural networks with fixed weights. *Neural Networks*, *98*, 296-304. http://doi.org/10.1016/j.neunet.2017.12.007

Guyon, I., Gunn, S., Nikravesh, M., & Zadeh, L. A. (2008). *Feature extraction: foundations and applications* (Vol. 207). Springer. http://doi.org/10.1007/978-3-540-35488-8

Hsu, Y.-C., Tsai, Y.-H., Weng, H.-H., Hsu, L.-S., Tsai, Y.-H., Lin, Y.-C., Hung, M.-S., Fang, Y.-H., & Chen, C.-W. (2020). Artificial neural networks improve LDCT lung cancer screening: a comparative validation study. *BMC Cancer*, *20*(1), 1023. https://doi.org/10.1186/s12885-020-07465-1

Islam, M. M., Haque, M. R., Iqbal, H., Hasan, M. M., Hasan, M., & Kabir, M. N. (2020). Breast Cancer Prediction: A Comparative Study Using Machine Learning Techniques. *SN Computer Science*, *1*(5), 290. https://doi.org/10.1007/s42979-020-00305-w

Jain, D., & Singh, V. (2018). Feature selection and classification systems for chronic disease prediction: A review. *Egyptian Informatics Journal*, *19*(3), 179–189. https://doi.org/10.1016/j.eij.2018.03.002

Khan, A., Shah, R., Imran, M., Khan, A., Bangash, J. I., & Shah, K. (2019). An alternative approach to neural network training based on hybrid bio meta-heuristic algorithm. *Journal of Ambient Intelligence and Humanized Computing*, *10*(10), 3821-3830. https://doi.org/10.1007/s12652-019-01373-4

Kohavi, R., & John, G. H. (1997). Wrappers for feature subset selection. *Artificial intelligence*, *97*(1–2), 273–324. https://doi.org/10.1016/S0004-3702(97)00043-X

Kumar, V. (2021). Evaluation of computationally intelligent techniques for breast cancer diagnosis. *Neural Computing and Applications*, *33*(8), 3195–3208. https://doi.org/10.1007/s00521-020-05204-y

Kumar, V., & Minz, S. (2014). Feature selection: a literature review. *SmartCR*, *4*(3), 211-229.

Kumari, M., & Singh, V. (2018). Breast Cancer Prediction system. *Procedia Computer Science*, *132*, 371–376. https://doi.org/10.1016/j.procs.2018.05.197

Liu, X., Li, B., Shen, D., Cao, J., & Mao, B. (2017). Analysis of Grain Storage Loss Based on Decision Tree Algorithm. *Procedia Computer Science*, *122*, 130–137. https://doi.org/10.1016/j.procs.2017.11.351

Moodley, J., Walter, F., Scott, S., & Mwaka, A. (2018). Towards timely diagnosis of symptomatic breast and cervical cancer in South Africa. *South African Medical Journal*, *108*(10), 803–804. https://doi.org/10.7196/SAMJ.2018.v108i10.13478

Mushtaq, Z., Yaqub, A., Hassan, A., & Su, S. F. (2019). Performance Analysis of Supervised Classifiers Using PCA Based Techniques on Breast Cancer. *2019 International Conference on Engineering and Emerging Technologies (ICEET)* (pp. 1–6). IEEE. https://doi.org/10.1109/CEET1.2019.8711868

Patsadu, O., Tangchitwilaikun, P., & Lowsuwankul, S. (2021). Liver Cancer Patient Classification on a Multiple-Stage using Hybrid Classification Methods. *Walailak Journal of Science and Technology*, *18*(10). https://doi.org/10.48048/wjst.2021.9169

Santos-Pereira, J., Gruenwald, L., & Bernardino, J. (2021). Top data mining tools for the healthcare industry. *Journal of King Saud University – Computer and Information Sciences*, in press. https://doi.org/https://doi.org/10.1016/j.jksuci.2021.06.002

Senturk, Z. K., & Kara, R. (2014). Breast Cancer Diagnosis Via Data Mining: Performance Analysis of Seven Different algorithms. *Computer Science & Engineering: An International Journal (CSEIJ)*, *4*(1), 35–46. https://doi.org/10.5121/cseij.2014.4104

Shenouda, E. A. M. A. (2006). A Quantitative Comparison of Different MLP Activation Functions in Classification. In: J. Wang, Z. Yi, J. M. Zurada, B. L. Lu & H. Yin (Eds.), *Advances in Neural Networks. Lecture Notes in Computer Science* (vol. 3971). Springer. https://doi.org/10.1007/11759966_125

Tang, J., Alelyani, S., & Liu, H. (2014). Feature selection for classification: A review. In *Data classification: Algorithms and applications* (chapter 2). Chapman and Hall/CRC. https://doi.org/10.1201/b17320

Vijayalakshmi, S., & Priyadarshini, J. (2017). Breast Cancer Classification using RBF and BPN Neural Networks. *International Journal of Applied Engineering Research*, *12*(15), 4775–4781.

Wahhab, H. T. A. (2015). *Classification of acute leukemia using image processing and machine learning techniques*. University of Malaya.

WBCD. (1995). Retrieved January 20, 2021 from https://archive.ics.uci.edu/ml/datasets/breast+cancer+wisconsin+(original).

Wu, J., Zhuang, Q., & Tan, Y. (2020). Auxiliary Medical Decision System for Prostate Cancer Based on Ensemble Method. *Computational and Mathematical Methods in Medicine*, *2020*, 6509596. https://doi.org/10.1155/2020/6509596

Yi, L., & Yi, W. (2017). Decision Tree Model in the Diagnosis of Breast Cancer. In *2017 International Conference on Computer Technology, Electronics and Communication (ICCTEC)* (pp. 176–179). IEEE. https://doi.org/10.1109/ICCTEC.2017.00046

Zarei, M., Ansari, H., Keshavarz, P., & Zerafat, M. (2020). Prediction of pool boiling heat transfer coefficient for various nano-refrigerants utilizing artificial neural networks. *Journal of Thermal Analysis and Calorimetry*, *139*(6), 3757–3768.

Applied Computer Science, vol. 17, no. 3, pp. 31–46
doi: 10.23743/acs-2021-19

Submitted: 2021-06-26 | Revised: 2021-09-08 | Accepted: 2021-09-21

fuzzy logic, fuzzy sets, fuzzy controller, simulation model, Matlab, SIMULINK

Andrzej JARDZIOCH [0000-0003-1285-8330]*,
Wioletta MARCZAK [0000-0001-7980-2652]*

APPLICATION OF A FUZZY CONTROLLER IN THE PROCESS OF AUTOMATED POLYETHYLENE FILM THICKNESS CONTROL

Abstract

The present article aims to describe the design of a fuzzy controller used for automated control of the thickness of the extruded polyethylene film effected by the adjustment of the actuator in the cooling ring. In order to determine whether the designed controller operates properly, a model extruder was created and a simulation study was carried out. The Simulink programming environment integrated with Matlab was used for the development of the fuzzy controller and the simulation. The conducted simulation study demonstrated that the implementation of the designed controller would enable the adjustment of thickness on the perimeter of the film tube and quick reaction to possible departure in the assumed film thickness in mass production.

1. INTRODUCTION

Decisions taken with regard to the production process are very complex. It is caused by a large, hard to define number of factors influencing decision-making and the fact that they are human decisions. The value of the same data or indicators can be variously assessed by different people. Having to account for the subjective uncertainty of decision-making is a serious drawback. Today, the system of decision-making can be optimized by the application of fuzzy inferencing (Lutomirski, Mazur & Strzelecki, 1995). Fuzzy inferencing is used in many fields of activity. It is found in computer-controlled systems for operating machines, robots and vehicles, data exploration tasks or creation of expert systems (Wachowicz, 2002). The main principle of fuzzy logic is a departure from the conventional division of responses into true (1) or false (0). Fuzzy logic makes it possible to calculate the degree of membership; that is, any state between 1 and 0. In this method, values and conditions relating to a certain phenomenon are expressed linguistically, not numerically. The output, in turn, can be calculated on the basis of comparison and correlation of these conditions (Lofti, 1988). Thanks to satisfying results of the application of the algorithm in many areas of technology, fuzzy logic is often selected in regulation systems. Fuzzy logic enables smoother

* West Pomeranian University of Technology, Faculty of Mechanical Engineering and Mechatronics , Poland, andrzej.jardzioch@zut.edu.pl, wioletta.marczak@zut.edu.pl

regulation and in the case when some information is missing, it yields better decisions than typical numerical methods (Ciloglu, 2010). Fuzzy inferencing enables the control of non-linear objects when their non-linearity renders their description by means of analytical methods difficult. Fuzzy control has the following characteristics:

- it enables the modeling of highly complex nonlinear dependencies where analytic description is difficult or impossible,
- it enables the application of adaptive parameter choice strategy on the basis of learning dataset (ANFIS – Adaptive Neuro-Fuzzy Inference Systems),
- it is flexible and it tolerates imprecise data,
- it is able to perform parallel calculations,
- it can be combined with conventional control systems (Driankov, Hellendoorn & Reinfrank, 1996).

The need to design algorithms for production scheduling and control has led to an increased interest in artificial intelligence tools. One of its calculation methods is fuzzy logic, whose application is very broad. The fuzzy logic algorithm is invaluable in solving numerous optimization problems, including engineering issues connected with the operation of production plants and other machines (Pasupathi Nath & Nishant Balaj, 2014).

Item (Czapaj, Kamiński & Benalcazar, 2020) on the reference list presents some thoughts on fuzzy logic and includes possible applications of fuzzy logic, e.g. in electrometry and industrial heating, control of cooling devices and mechanical hard disks, image processing and speech recognition. The authors of (Zou, Yan, Wang & Zhang, 2020) present the application of fuzzy logic algorithm in controlling the operation of photovoltaic systems. The study offers an improved algorithm of maximum power point tracking based on the principle of fuzzy control and differential flatness control theory. Firstly, due to the application of differential flatness control, the output voltage of a PV cell increases linearly and a maximum power point voltage is found. Then, a fuzzy logic algorithm is used to stabilize the PV cell output voltage. The applicability of the algorithm is verified by MATLAB simulations and an equipment experiment. An interesting application of fuzzy logic in motion control is described in (García-Martínez et al., 2020). In this study, a new strategy is presented for tuning a proportional-integrative-derivative (PID) fuzzy logic controller (FLC), which relies on direct fuzzy relations in order to compute PID constants. Another interesting and innovative approach is presented in (Skobiej & Jardzioch, 2019). This paper discusses the ways in which the design of a given fuzzy logic system influences the construction of rules for a particular agent. The article focuses on the problem of coding the agent's rules and modification of the coding by genetic algorithm. The agent's task is to make an effective decision on which order, from the set of the awaiting orders, should be transferred into a production zone next. The decision is based on the response of the fuzzy logic system.

The objective of the present study is to introduce the design of a fuzzy controller used for automated control of thickness of the extruded polyethylene film effected by the adjustment of the actuator in the cooling ring. In order to determine whether the designed controller works properly, an operational model of an extruder was developed with the application of fuzzy control. The paper is divided into five sections. The first one includes a review of the literature on the applications of fuzzy logic to optimize the operation of devices and processes. Section two presents the research problem connected with the control

of a PE film extruder. In section three, the developed fuzzy controller used for the adjustment of the actuators in the cooling ring is described. Section four presents the results of tests used to indicate whether the developed controller adjusting the actuators in the cooling ring works properly, which were carried out in the operational model of the extruder. The operation of the controller was validated in the MATLAB and Simulink environments. The final section of the paper presents conclusions and suggestions for further study.

2. RESEARCH PROBLEM

One of the major difficulties that arise in the operation of a PE film extruder is the retention of film thickness on the perimeter of the tube, as in the next step the PE film is welded to produce plastic bags. The bags are tested for weld seam resistance. If the film's thickness is not even on the perimeter of the tube, it will not be resistant enough to pass the tests. The bags will crack primarily on the weld seams, generating production waste and increasing the cost of production process. It can therefore be assumed that failure to retain an even thickness of the film will result in:

- decreased mechanical resistance of the PE film and products made of it,
- increased raw material consumption,
- decreased quality of the film on the yarn,
- lower efficiency or impossibility of running technological processes which use PE film (printing, welding) (Lutomirski, Mazur & Strzelecki, 1995).

There are two types of deviation in PE film thickness:

- deviation of the mean value from the nominal value of the film thickness measured along the axis of the extruded film. This is usually caused by wrong relation between the speed of the extruder screw and the extraction speed. It follows from a lack of stability of the speeds; a variable bulk density of raw material, pressure pulsation and interrupted flow of raw material leading to fluctuation in temperature in cylinder and head heating zones, resulting in flow resistance variation. The latter is significant for extruders with high wear of the plasticizing system,
- deviation in the film thickness in the cross section, which mainly results from fluctuation in the intensity of the flow of the extruded film through the nozzle and inappropriate cooling conditions. It may be caused by contamination of the nozzle, uneven aperture in the nozzle of the extruder head, thermal heterogeneity of the material inside the head and the tube cooling asymmetry in the cooling unit or errors in construction of the head or cooling ring.

The application of gravimetric dosing system in the process of PE film production enables the restriction of film density tolerance limits measured in length. The application of such a method of feeding raw material also significantly limits its intake (Lutomirski, 2005).

This paper focuses on presenting a solution for the control and adjustment of film thickness and the elimination of deviation in film thickness in cross section. The paper discusses the application of a fuzzy controller which is meant to assist the setting of appropriate setpoints accompanying the extruder's start-up, but also to retain the pre-set values for film thickness within the limit of +/– 3 sigma.

The object of the study is the production process of polyethylene film by blow extrusion. Figure 1 presents a diagram of a blow extrusion machine.

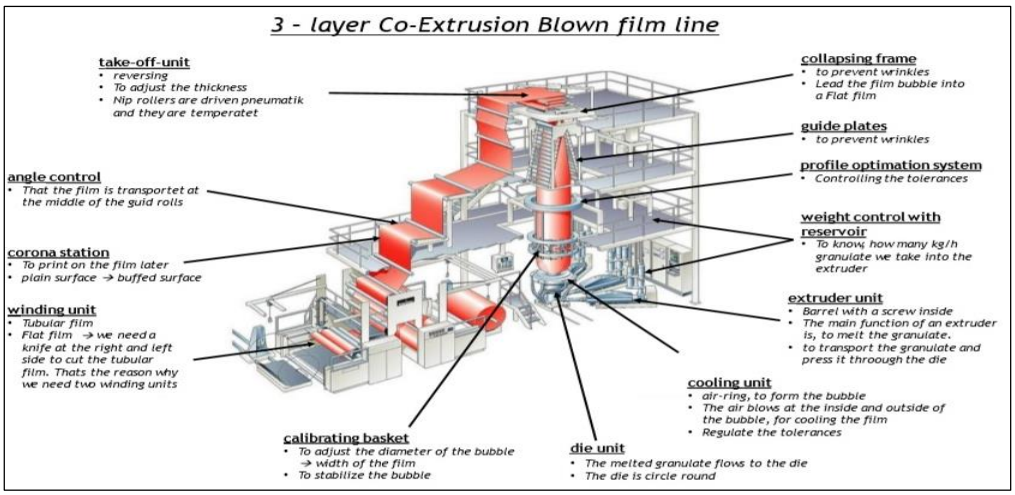

Fig. 1. A diagram of a blow extrusion machine

The most important objective is to obtain film of even thickness on the perimeter that falls within the tolerance limits determined by the customer. The machine is man-operated. Film thickness is measured manually and the operator manually sets the screws that determine the slit-width on the head of the blower. A description of the steps taken by operators and of the production process itself can be found in (Jardzioch, Marczak & Krebs, 2018; Jardzioch, Marczak & Skobiej, 2019; Jardzioch & Marczak, 2020). Paper (Jardzioch & Marczak, 2020) presents a diagram of a blow extrusion machine without automated control of film thickness. It describes a concept for ap-plication of Fuzzy Logic control in measuring film profile and automated adjustment of film thickness with the use of automatic cooling ring.

In order to set the required thickness of the produced PE film, the operator takes the following main steps:

- setting machine parameters according to the parameter chart (incl.: density: gr/m^2, feed rate: kg/h, screw revolutions u/min, calender rolls speed m/min),
- observation of the position and shape of the blown bubble, and, depending on the operator's subjective assessment, taking subsequent steps (figure 2 presents a diagram of the position and shape of the blown bubble),
- manual setting of the screws that determine the slit-width on the head of the blower,
- another observation of the position of the bubble – if it is stable, according to the opera-tor's subjective assessment, no subsequent steps are taken before another thickness measurement is conducted on a sample from the PE film yarn,
- after film thickness measurement when uneven thickness appears, the procedure of adjusting regulatory screws is continued.

Setting of the screw that determines the slit-width on the head of the blower is conducted on the basis of the human knowledge and experience. Consequently, it is possible for each opera-tor to take different action concerning the regulation of the machine to solve a given problem. Operators have varying knowledge and experience, which may entail differences in the regulatory action taken, and the effect may be different than expected. Sometimes the time in which a satisfying level of film thickness is achieved is different, increasing the amount of production waste.

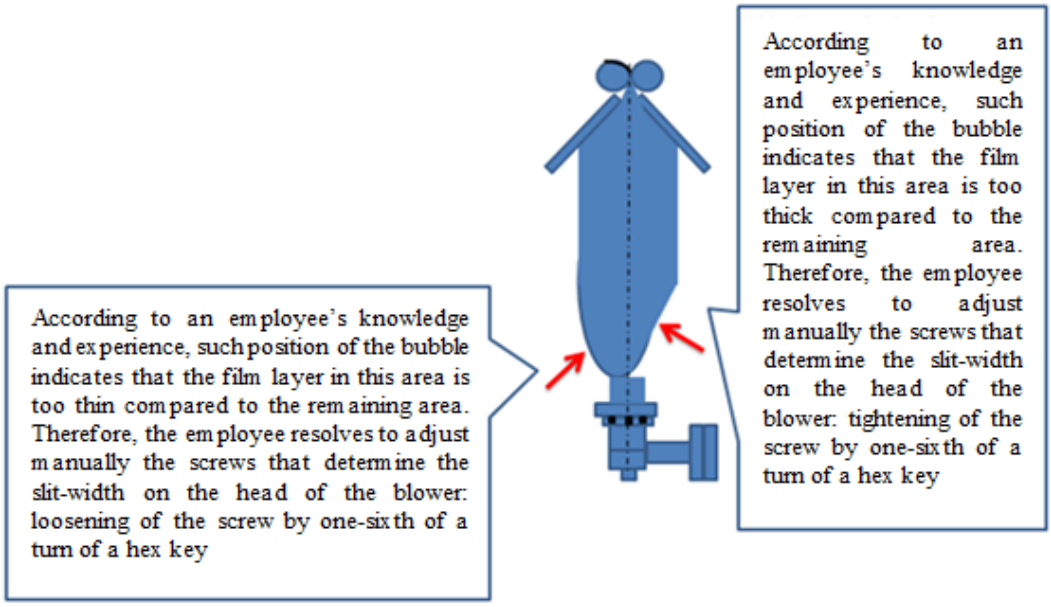

Fig. 2. Position and shape of the blown bubble

Another example of a situation when a problem with uneven film thickness on the perimeter may arise is a change in ambient temperature during the three production shifts, such as a nightly drop in temperature by 15 degrees Celsius. Then the adjustment of film thickness is achieved by setting the cooling from the cooling ring. This, however, does not enable segmental, local adjustments of the film thickness. The cooling is increased or de-creased over the whole perimeter of the tube. Other possible situations that cause inconsistencies in film thick-ness include: incorrect setting of the slit-width on the head of the blower, insufficient tightening of the bolts and their loosening during operation, and a build-up of scale at the head during machine operation.

Considering prolonged reaction time with regard to the implementation of corrective measures, varying action taken depending on the operator, their knowledge and experience, as well as machine design constraints, a decision was made to develop and apply a fuzzy controller that would automatically set and control the thickness of extruded film in mass production. This study presents a fuzzy controller which controls one of the 32 actuators regulating air cooling in the cooling ring.

3. THE DESIGN OF A FUZZY CONTROLLER TO CONTROL POLYETHYLENE FILM THICKNESS

In this paper, the authors introduce their own concept of a fuzzy controller tailored to the needs of the production process in question, drawing upon the experience of the experts con-trolling the PE film production process.

Experimental studies on the testing facility demonstrated that it is the time of reaction to a disturbance that has the biggest impact on correct film thickness control. Another crucial issue is to be able to take regulatory action on the film tube exactly where the deviation outside the assumed tolerance occurred.

In order to develop the concept, the application of a controller to measure film thickness directly on the machine was suggested. It was assumed that the information obtained from measurements should be transmitted to the main computer, where the data would be verified with the aid of an intelligent controller based on fuzzy inferencing. The signals formulated by the controller would be passed to the cooling ring located at the base of the machine. In the case when the film is too thick in certain areas, the cooling should be decreased. When the produced film is too thin, the intensity of cooling in the given areas should be increased. The measurements of film thickness should be taken throughout the whole cycle of production. Figure 3 presents the diagram of the application of a fuzzy controller in PE film production with different signal paths.

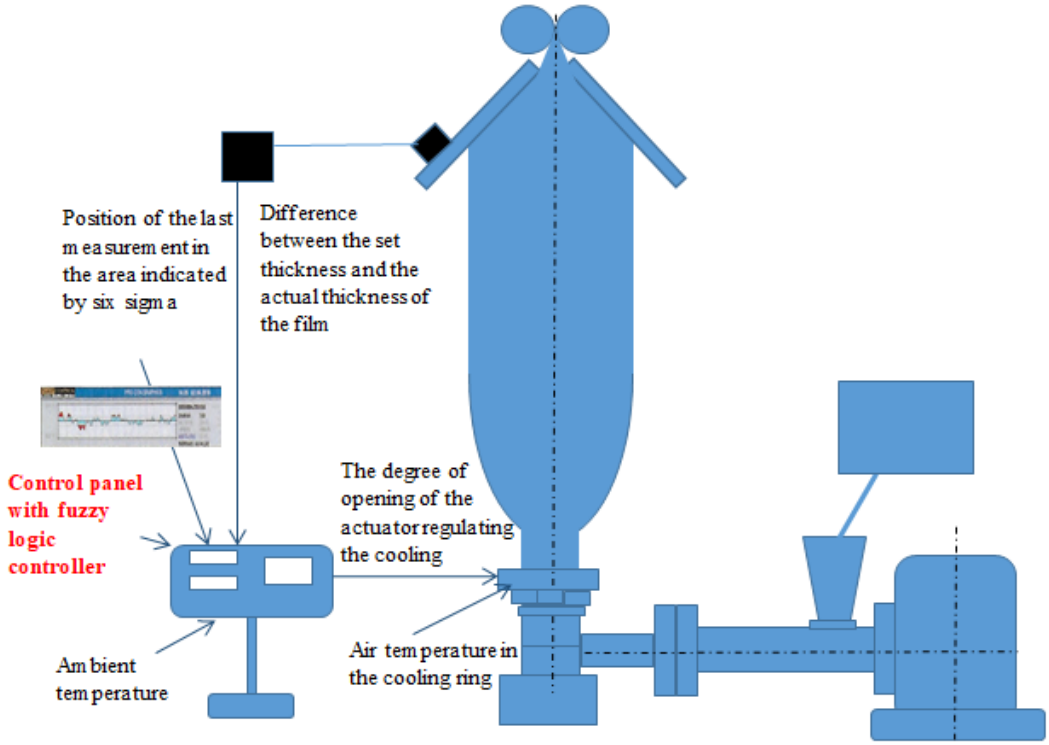

Fig. 3. A diagram of the application of a fuzzy controller in PE film production and the signal paths

Measurement results are sent to the main computer with a fuzzy controller on an ongoing basis; followed by verification and appropriate reaction. Controlled air-flow cooling provides on-target impact on film thickness in the material zone.

The system for adjusting film thickness operates continually. It retrieves information on the current state of the production system. Then the process of inferencing is conducted, as a result of which a parameter is generated that determines whether to decrease or increase air-flow cooling on the extruded film bubble. The cooling is performed by means of regulatory actuators on the cooling ring. The data used for the development of the fuzzy controller refers to film thickness measurements carried out directly on the extruder, in the conditions of mass production.

To fulfill the research objective, two systems were developed. One is fuzzy controller 1, which will control the operation of the cooling ring and adjust the degree of opening of its actuators which regulate the cooling. As a target, fuzzy controller 1 is meant to be fitted on the extruder, but in the research phase there is no such possibility. It results from financial concerns related to high cost of assembly, the need to involve additional staff members from the IT and engineering departments and the amount of time required to complete the task. Consequently, a decision was made to develop another system, the extruder operation model. It is meant to simulate the operation of the extruder so that the application of fuzzy controller 1 that adjusts the cooling in the cooling ring can be examined.

Three input variables: x1, x2 and x3 were used for fuzzy controller 1. The first variable (variable x1) is the difference between the set thickness and the actual thickness of the film. It may assume positive or negative values. The maximum negative value is –10, while the maximum positive value is +10. Both maximum values, positive and negative, serve to indicate the range to be covered by the fuzzy sets. The second input variable (variable x2) is the position of the last measurement in the area indicated by six-sigma. Variable x2 may assume positive or negative values. The maximum negative value of the position of the last point is –3. In this area, the points whose value is below the center line on the control chart are found. The maximum positive value is +3. In this area, there are those points whose value is above the center line on the control chart. The values of variable x2 are defined by the ranges of positions of the points within the distance of +/– 3 sigma from the mean value of film measurements recorded on the control chart. It is relevant in which zone below or above the center line the last measurement is, as it may suggest process deregulation and consequently possible significant deviations in the thickness on the perimeter. The third variable (variable x3) is the ambient temperature. Here, the values can range from the minimum +10°C to the maximum +35°C. They represent the lowest and the highest ambient temperature recorded during the tests. The ambient temperature has to be considered as a change in the value influences the thickness of the extruded film at a given time. Input variable values for fuzzy controller 1 were divided into intervals. Variables x1 and x2 were divided into 7 intervals: very large positive (bdd), large positive (dd), small positive (md), close to zero (bz), small negative (mu), large negative (du), very large negative (bdu). Variable x3 was divided into 5 intervals: very small (bm), small (m), medium (s), large (d) and very large (bd). The output variable is the degree of openness of actuators regulating the cooling in the automatic ring (y). As with variables x1 and x2, it was divided into 7 intervals.

In the case of fuzzy controller 1 the process of inferencing based on fuzzy logic was applied in order to determine the settings of the actuators regulating air-flow cooling with the aim of obtaining the expected film thickness. The inferencing process consists of three stages: fuzzification, i.e. converting input variables into fuzzy variables; inferencing with the use of linguistic rule base; and defuzzification, i.e., obtaining a single number from the output variable. Figure 4 presents the particular stages of the inferencing process based on fuzzy logic for the system of fuzzy controller 1.

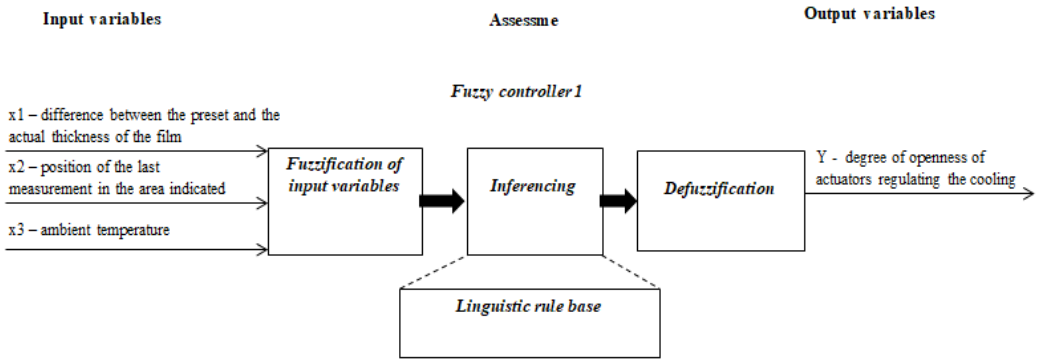

Fig. 4. Stages of the inferencing process based on fuzzy logic for the system of fuzzy controller 1

At the fuzzification stage, the particular input variable values are ascribed the values of fuzzy sets that describe them. The input variable is interpreted here as a linguistic variable with appropriately defined values. A classic theory of sets assumes that any given element can "partially belong to a set" and this membership can be expressed by a real number from the range (0, 1) whose value is determined by a properly defined membership function (Jardzioch, 2009).

Table 1 presents the particular linguistic variables and their ascribed membership functions.

In fuzzy logic, the conclusion block is where the degree of activation of the premises is calculated on the basis of fuzzy rules. The rule base is composed of a set of conditional instructions (premises). They are derived from the experience of the process operator.

The rules are composed of a conditional block (a premise, IF-statement) and a conclusion block Yj starting after the word THEN. The fuzzification of input variables enables direct use of rules expressed in linguistic terms, as sentences. Figure 5 presents sample linguistic rules used for assessing the degree of opening of the actuators regulating the cooling. For fuzzy controller 1 there are 245 rules in the controller's rule base. They determine the degree of opening of the actuators regulating the cooling. The number of rules is the product of the numbers of fuzzy sets.

Tab. 1. Linguistic variables and their ascribed membership functions for the developed *fuzzy controller 1*

No.	Indication	Linguistic variable description	Membership functions
1.	*Fuzzy controller 1*	X1 – difference between the preset and the actual thickness of the film [µm]; values: very large positive (bdd), large positive (dd), small positive (md), close to zero (bz), small negative (mu), large negative (du), very large negative (bdu).	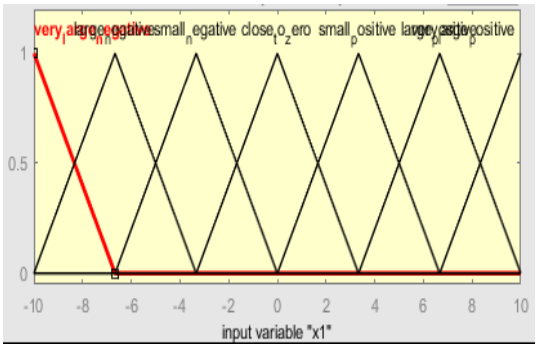
2.		X2 – position of the last measurement in the area indicated by six sigma; values: very large positive (bdd), large positive (dd), small positive (md), close to zero (bz), small negative (mu), large negative (du), very large negative (bdu)	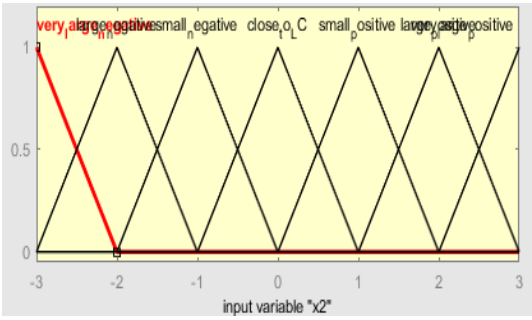
3.		X3 – ambient temperature [°C]; values: very small (bm), small (m), medium (s), large (d) and very large (bd).	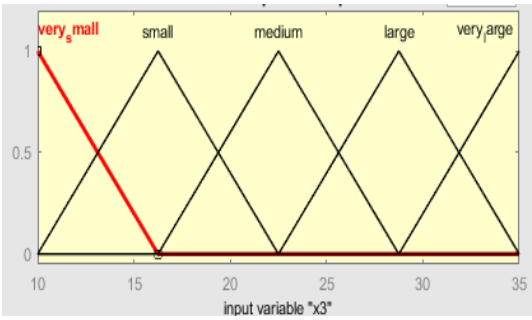
4.		Y – degree of openness of actuators regulating the cooling; values: very large positive (bdd), large positive (dd), small positive (md), close to zero (bz), small negative (mu), large negative (du), very large negative (bdu)	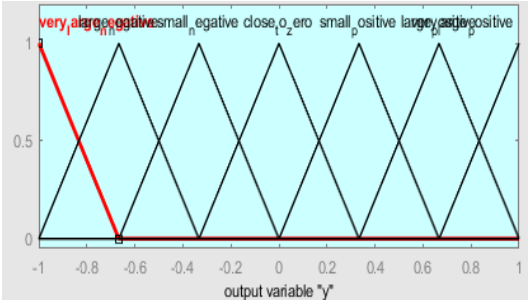

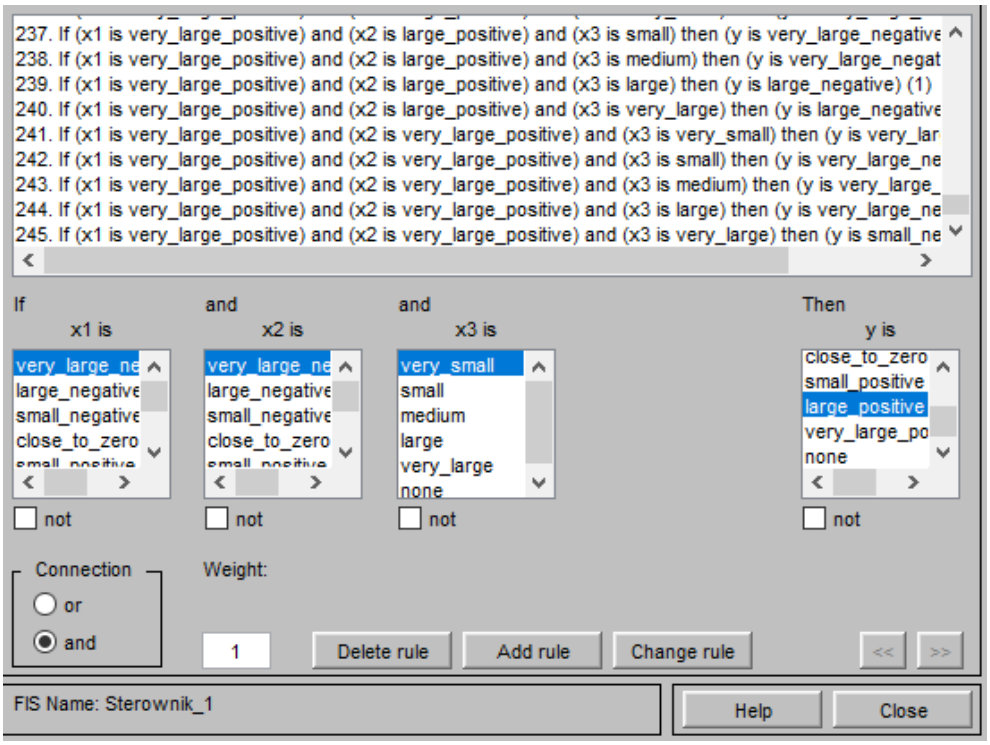

Fig. 6. Examples of rules used for assessing the degree of opening of the actuators regulating the cooling in the fuzzy controller

The fuzzy inference value is transferred to the defuzzification block.

As a result of the defuzzification process, the value is obtained for the degree of opening of the actuators regulating the cooling in the automatic ring. In the devised controller, defuzzification is performed with the use of Mean of Maximum method (MOM).

4. SIMULATION TESTS PRESENTING THE OPERATION OF THE DEVISED FUZZY CONTROLLER

Simulation tests were conducted with the use of Matlab program with Fuzzy Logic Toolbox and SIMULINK modules. To develop the simulation model, four different Simulink blocks were used, namely: From SpreadSheet, Mux, Fuzzy Logic Controller with Ruleviewer, To Workspace. Actual data obtained in the process of polyethylene film production were used in the studies.

Figure 7 shows the extruder operation model developed to test the operation of the devised fuzzy controller which controls the cooling in the cooling ring, along with and its variables.

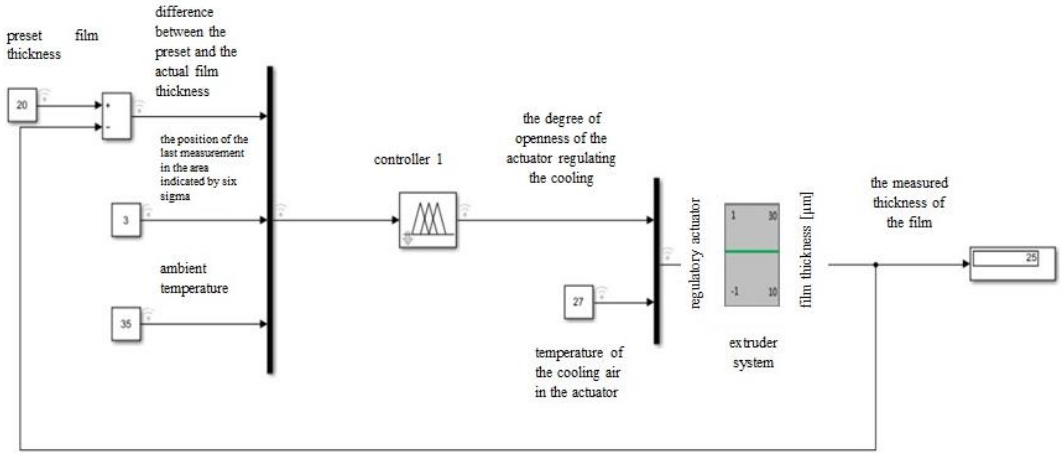

Fig. 7. The concept of simulation model to verify the operation of fuzzy control

Two input variables x4 and x5 were used for the concept of the extruder operation model. The first input variable for the extruder operation model (variable x4) is the output variable (y) of fuzzy controller 1, that is the degree of opening of the actuators regulating the cooling in the automatic ring. The maximum value assumed by variable x4 is +1 and the minimum value is –1. The second input variable for the extruder operation model (variable x5) is the temperature of the cooling air in the actuator. Its values range from a minimum +19°C to the maximum +35°C. These are the lowest and the highest temperatures recorded in the actuator during the tests. The temperature of the cooling air in the actuator matters a lot, because any change in the temperature of the cooling air influences the thickness of the extruded film. Input variable values for the extruder operation model were divided into intervals. Variable x4 was divided into 7 intervals: very large positive (bdd), large positive (dd), small positive (md), close to zero (bz), small negative (mu), large negative (du), very large negative (bdu). Variable x5 was divided into 5 intervals: very small (bm), small (m), medium (s), large (d) and very large (bd). The output variable is the measured film thickness (y2). It was divided into 5 intervals: very small (bm), small (m), small close to nominal (mbn), large close to nominal (dbn), large (d) and very large (bd).

With regard to the extruder operation model, the inferencing process based on fuzzy logic was applied to test the operation of fuzzy controller 1. Figure 8 presents an example of fuzzy controller 1 in operation. It presents the way in which the rules of fuzzy inference influence the data transferred to the fuzzy controller. As for fuzzy controller 1, in figure 8, three vertical lines indicate the values supplied to the fuzzy controller: the difference between the set and the actual thickness of the film = 10, the position of the last measurement in the area indicated by 6 sigma = 3 sigma, ambient temperature = 35°C. The yellow color indicates that the particular variable belongs to fuzzy sets. The blue color indicates that the output variable belongs to fuzzy sets. The value of this variable – here, the degree of opening of the actuators regulating the cooling – is determined during the defuzzification process. In this case, the de-gree of opening of the actuators regulating the cooling after the first cycle equals –0.34. This means that the opening of the actuators is reduced, which leads to a reduction of cooling air-flow and as a result, film thickness is decreased.

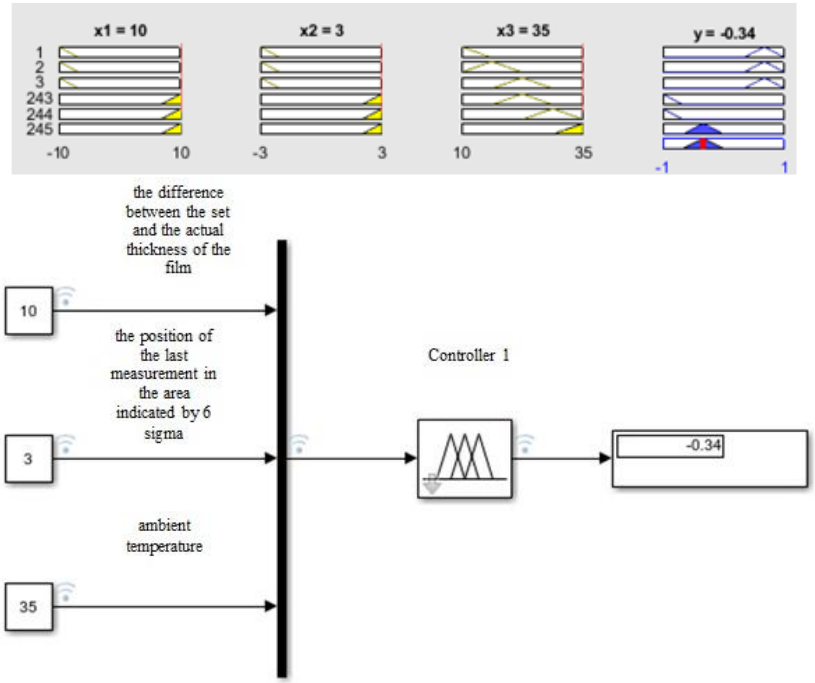

Fig. 8. Example of the operation of fuzzy controller 1 – the degree of opening of the actuators regulating the cooling

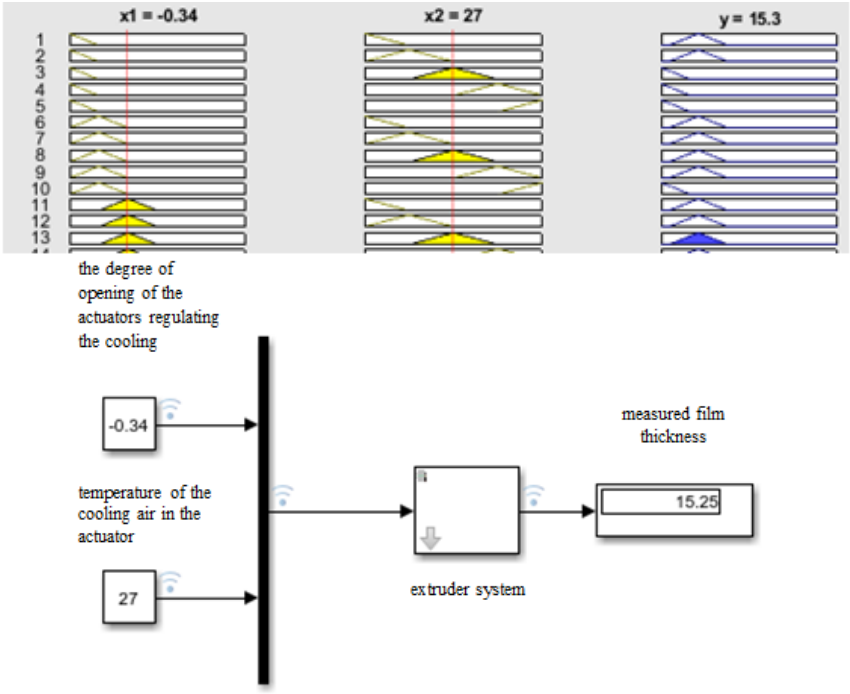

Fig. 9. Extruder operation model

In the case of the extruder operation model whose task is to simulate the operation of an extruder and test the application of a fuzzy controller controlling the cooling in the ring (Figure 9), there are two vertical lines indicate the values supplied to the extruder operation model: the degree of opening of the actuators regulating the cooling. This value was the fuzzy controller's output and equaled –0.34 in the first cycle of the study. The second supplied value referred to a disturbance in the cooling air temperature and equaled 27°C. The output variable for the extruder operation model is the measured film thickness. In the first round of tests, the measured film thickness was 15.3 μm. This means that the nominal thickness of 20 μm was not attained.

Table 2 present the simulation results, including subsequent rounds of tests. Each cycle was further divided into variables belonging to the fuzzy controller and to the extruder operation model.

In the part referring to the fuzzy controller the first three columns contain input variables. These input variables were: the difference between the set and the actual thickness of the film (variable x1), the position of the last measurement in the area indicated by 6 sigma (variable x2), ambient temperature (variable x3). In the last column there is the output variable Y indicating the degree of opening of the actuators regulating the cooling. In the row below the variables, comments about the results can be found. In the part referring to the extruder operation model the first two columns contain input variables: the degree of opening of the actuators regulating the cooling in the automatic ring (variable x4) and the temperature of the air in the actuator (variable x5). The third column contains the output variable Y2, that is, the measured film thickness. In accordance with the assumed procedure, if no interference in the process is necessary, such as the adjustment of the airflow by means of actuators, then the degree of opening of the actuators regulating the cooling is 0. If the degree of the opening is higher than 0, then the cooling airflow is increased, which leads to increased thickness. When the degree of the opening is lower than 0, the opening is reduced; consequently, a decrease in the cooling airflow leads to decreased thickness of the film. In the extruder operation model a disturbance referring to air temperature in the regulating actuators was accounted for.

Tab. 1. Selected simulation results

First cycle of tests			
Fuzzy controller 1			
***x*1** **the difference between the set and the actual thickness of the film**	***x*2** **the position of the last measurement in the area indicated by 6 sigma (s)**	***x*3** **ambient temperature (°C)**	**Y** **the degree of opening of the actuators regulating the cooling in the automatic ring**
+10	+3	35	-0.34
Comment	A reduction in the degree of the opening of the actuators is required to the level of –0.34, which will result in decreased film thickness.		
Extruder operation model			
***x*4** **the degree of opening of the actuators regulating the cooling in the automatic ring**		***x*5** **air temperature in the actuator (°C)**	***Y2*** **measured film thickness (µm)**
-0.34		27	15.3
Comment	Setting the degree of opening of the actuators at -0.34 and accounting for the disturbance in the form of air temperature in the actuator, the measured film thickness is 15.3 µm, which means that the expected thickness 20 µm is not achieved.		
Second cycle of tests			
Fuzzy controller 1			
***x*1**	***x*2**	***x*3**	**Y**
-4.7	-1.5	35	0.33
Comment	An increase in the degree of opening of the actuators regulating the cooling to the level of 0.33 is required, which will result in increased thickness of the film.		
Extruder operation model			
***x*4**		***x*5**	***Y2***
0.33		27	24.88
Comment	Setting the degree of opening of the actuators at 0.33 and accounting for the disturbance in the form of air temperature in the actuator, the measured film thickness is 24.88 µm, which means that the expected thickness 20 µm is not achieved.		
Third cycle of tests			
Fuzzy controller			
***x*1**	***x*2**	***x*3**	**Y**
4.88	1.5	35	0
Comment	A reduction in the degree of opening of the actuators regulating the cooling to the level of 0 is required, which will result in decreased thickness of the film.		
Extruder operation model			
***x*4**		***x*5**	***Y2***
0		27	20.13
Comment	Setting the degree of opening of the actuators at 0 and accounting for the disturbance in the form of air temperature in the actuator, the measured film thickness is 20.13 µm, which means that it is very close to the expected 20 µm.		

5. CONCLUSIONS

The aim of the present study was to develop two systems. One of them was fuzzy controller 1, whose task was to control the operation of the cooling ring and adjustment of the degree of opening of the actuators regulating the cooling which are set in that ring. Fuzzy controller 1 is eventually meant to be installed on the machine, but it is impossible in the phase of experimental study owing to financial obstacles connected with high costs of assembly, involving additional staff members from IT and engineering departments, or extra time required to fulfill the task. With these limitations in mind, a second system called the extruder operation model was developed. It simulated the operation of an extrusion machine and was used to test the application of fuzzy controller 1 for the control of cooling in the cooling ring; specifically, in one of the 32 actuators built into it. The devised systems: fuzzy controller 1 and extruder operation model were developed in the MATLAB SIMULINK environment. On the basis of conducted simulations, it was concluded that the solution based on the application of fuzzy controller 1 is helpful in the setting of appropriate set points accompanying the extruder's start-up, but also in retaining the pre-set values for film thickness. Fuzzy controller 1 enables prompt reaction to disturbances in the process of blow extrusion. Due to the application of fuzzy controller 1, which adjusts the cooling in the cooling ring by adjusting the degree of opening of the actuator, the system will work better as in some cases such adjustments cannot be made manually by the operator. The tests administered so far indicate that the application of the devised fuzzy controller 1 will facilitate a quick reaction, and consequently a retention of homogenous film thickness on the perimeter in the process of mass production. The implementation of a fuzzy controller made it possible to use the knowledge and experience of the operators and to express it in the form of linguistic rule base. As part of further study, the authors intend to develop another concept of the extrusion machine operation; this time, relying on artificial neural networks and their integration with fuzzy logic. Additionally, the model will be extended by a system presenting the operation of an extruder, including all 32 actuators regulating the cooling airflow in the cooling ring. The authors also plan to put forth a strategy for tuning a proportional-integrative-derivative (PID) fuzzy logic controller (FLC), which relies on direct fuzzy relations in order to compute PID constants.

REFERENCES

Ciloglu, Y. (2010). *A Short Fuzzy Logic Tutorial*. Bilkent.

Czapaj, R., Kamiński, J., & Benalcazar, P. (2020). Logika rozmyta dla potrzeb sterowania układów napędowych – wprowadzenie teoretyczne. *Energetyka*, *3*, 103–111.

Driankov, D., Hellendoorn, H., & Reinfrank, M.(1996). *Wprowadzenie do sterowania rozmytego*. WNT.

García-Martínez, J. R., Cruz-Miguel, E. E., Carrillo-Serrano, R. V., Mendoza-Mondragón, F., Toledano-Ayala, M., & Rodríguez-Reséndiz, J. (2020). A PID-Type Fuzzy Logic Controller-Based Approach for Motion Control Applications. *Sensors*, *20*(18), 5323. https://doi.org/10.3390/s20185323

Jardzioch, A. (2009). *Sterowanie elastycznymi systemami obróbkowymi z zastosowaniem metod sztucznej inteligencji*. Zachodniopomorski Uniwersytet Technologiczny w Szczecinie.

Jardzioch, A., & Marczak, W. (2020). Opracowanie inteligentnego sterowania adaptacyjnego do nadzorowania pracy maszyny wytłaczającej folię polietylenową. In *Inżynieria zarządzania, Cyfryzacja produkcji Aktualności badawcze 3* (pp. 617–627). PWE.

Jardzioch, A., Marczak, W., & Krebs, I. (2018). The improvement of manufacturing proces through the use of statistical process control. *Journal of Machine Construction and Maintenance*, *4*, 105–111.

Jardzioch, A., Marczak, W., & Skobiej, B. (2019). The application of fuzzy logic in monitoring the stability of a production proces. In *Innowacyjne metody i technologie w badaniach inżynierskich* (pp. 391–404). Wydawnictwo Uczelniane Politechniki Koszalińskiej.

Lofti, A. Z. (1988). Fuzzy Logic. *Computer*, *21*(4), 83–93.https://doi.org/10.1109/2.53

Lutomirski, S. (2005). Metody stabilizacji grubości folii w procesie jej wytwarzania metodą wytłaczania ze swobodnym rozdmuchiwaniem. *Przetwórstwo Tworzyw*, *11*(2), 50–55.

Lutomirski, S., Mazur, J., & Strzelecki, R. (1995). Układy pomiaru i stabilizacji grubości wytwarzanej metodą wytłaczania z rozdmuchiwaniem. *Polimery*, *10*, 601–605.

Pasupathi Nath, R., & Nishant Balaj, V. (2014). Artificial intelligence in power systems. *IOSR Journal of Computer Engineering*, 1–7.

Skobiej, B., & Jardzioch, A. (2019). Selected Aspects of Crossover and Mutation of Binary Rules in the Context of Machine Learning. In: J. Świątek, L. Borzemski, & Z. Wilimowska (Eds.), *Information Systems Architecture and Technology: Proceedings of 39th International Conference on Information Systems Architecture and Technology – ISAT 2018. ISAT 2018. Advances in Intelligent Systems and Computing* (vol. 853). Springer. https://doi.org/10.1007/978-3-319-99996-8_34

Wachowicz, E. (2002). Zastosowania teorii zbiorów rozmytych do modelowania procesów technologicznych. *Inżynieria Rolnicza*, *7*(40), 5–17.

Zou, Y., Yan, F., Wang, X., & Zhang, J. (2020). An efficient fuzzy logic control algorithm for photovoltaic maximum power point tracking under partial shading condition. *Journal of the Franklin Institute*, *357*(6), 3135–3149. https://doi.org/10.1016/j.jfranklin.2019.07.015

Applied Computer Science, vol. 17, no. 3, pp. 47–59
doi: 10.23743/acs-2021-20

Submitted: 2021-05-23 | Revised: 2021-09-14 | Accepted: 2021-09-21

Optimal Sliding Mode Controller, Whale Optimization Algorithm, lower limb, rehabilitation robot

Noor SABAH [0000-0003-1512-1158]*, *Ekhlas HAMEED* [0000-0002-9039-2030]**, *Muayed S AL-HUSEINY* [0000-0003-3192-0232]***

OPTIMAL SLIDING MODE CONTROLLER DESIGN BASED ON WHALE OPTIMIZATION ALGORITHM FOR LOWER LIMB REHABILITATION ROBOT

Abstract

The Sliding Mode Controllers (SMCs) are considered among the most common stabilizer and controllers used with robotic systems due to their robust nonlinear scheme designed to control nonlinear systems. SMCs are insensitive to external disturbance and system parameters variations. Although the SMC is an adaptive and model-based controller, some of its values need to be determined precisely. In this paper, an Optimal Sliding Mode Controller (OSMC) is suggested based on Whale Optimization Algorithm (WOA) to control a two-link lower limb rehabilitation robot. This controller has two parts, the equivalent part, and the supervisory controller part. The stability assurance of the controlled rehabilitation robot is analyzed based on Lyapunov stability. The WO algorithm is used to determine optimal parameters for the suggested SMC. Simulation results of two tested trajectories (linear step signal and nonlinear sine signal) demonstrate the effectiveness of the suggested OSMC with fast response, very small overshoot, and minimum steady-state error.

1. INTRODUCTION

Spinal cord injury, accidents, and stroke are the significant sources of disability for the athletics, drivers, and elderly persons that create troubles in their lifes (Furlan et al., 2021; Rodrigues & Rodrigues, 2018). Rehabilitation tools were focused on recovering full/partial functionality by enhancing their motion capabilities using different techniques. Recently, wearable robots of lower-limb exoskeletons have been employed for helping disabled people with mobility issues (Rupal et al., 2017).

A rehabilitation robot is a robot that helps patients recuperate from strokes or other types of extremity injuries. The goal of developing a rehabilitation robot is to assist individuals with daily living problems. Since robots are suited to provide a precise and reproducible physiotherapy, they are excellent tools for providing high-quality treatment at a low cost with minimal intervention (Saryanto & Cahyadi, 2016).

* University of Wasit, Electrical Engineering Department, Iraq, noors@uowasit.edu.iq
** Mustansiriyah University, Computer Engineering Department, Iraq, ek_karam@uomustansieiryah.edu.iq
*** University of Wasit, Electrical Engineering Department, Iraq, malhuseiny@uowasit.edu.iq

The preferred path of robot joints needs a strong controller to reduce a steady-state error to minimize disturbances and the variation of system parameters. Different controller strategies with parameter optimization techniques are developed to guarantee asymptotic stability and to estimate the uncertainty aspects of adaptive controlled lower-limb systems. The Sliding Mode Controller (SMC) is often considered one of the most effective methods used to control robotic systems, including rehabilitation robots.

Babaiasl et al. (2015) proposed a sliding mode controller for upper limb rehabilitation robots to track desired trajectories and reject system uncertainties and disturbances. (Zhou, Zhou & Ai, 2016) proposed an impedance control strategy for rehabilitation robots based on nonsingular terminal sliding mode control to ensure precision in trajectory tracking and improve the stability of the system. (Liu et al., 2018) proposed Adaptive Sliding Mode Control (ASMC) for a lower limb exoskeleton rehabilitation robot to achieve improved performance in terms of jitter elimination and trajectory tracking. For alternative control methods in lower limb rehabilitation robots, (Yang & Gao, 2020) suggested the Adaptive Neural Sliding Mode Controller. The authors proposed a control strategy that dynamically switches between assistance and challenge modes depending on the user's performance by amplifying or decreasing the deviation between the user and the rehabilitation robot in their analysis. A multisensor fusion system was proposed for a seamless cognitive and physical interaction between the robot and the patient. The system uses radial basis function (RBF) to provide reliable activity and motor capability recognition, fall detection, and physical fitness assessment in the rehabilitation training process. (Abbasimoshaei & Mohammadimoghaddam, 2020) designed Adaptive Fuzzy Sliding Mode Controller (AFSMC) for a hand rehabilitation robot to overcome uncertainties and disturbances, reduce chattering effects, and compensate the varying forces of the patients. (Almaghout et al., 2020) proposed super-twisting nonsingular terminal sliding mode control for design and control of a lower limb rehabilitation robot, taking into account negative torques of the patient's limb to obtain the desired training missions; their results are comparable to those of adaptive sliding mode control. A Fuzzy Sliding Mode Controller (FSMC) was also proposed by (Maalej et al., 2020) for minimizing torques applied to a rehabilitation robot to help children, suffering from several diseases, to walk compared to the use of wheelchairs. Their simulation results show that the proposed controller is effective, moreover, it has been shown that the fuzzy sliding mode controllers are robust against parametric variations such as masses and lengths of kid’s legs.

This research focuses on designing an Optimal Sliding Mode Controller (OSMC) based on Whale Optimization Algorithm (WOA) for tracking the trajectory of a two-link lower-limb rehabilitation robot by using dynamic equation for a human two-joint during-walk lower-limb model. WOA is used to tune the parameters of the suggested controller. The dynamic model of this robot is was derived by (Rezage & Tokhi, 2016) depended on anthropometric data (described by Winter (2009)). The stability analyses of both joints of a closed-loop controlled system based on the dynamic robot equations are explained by Lyapunov stability.

The rest of this paper is organized as follows, the dynamic mathematical model of the two-link lower-limb rehabilitation robot is given in section 2, the suggested controller is detailed in section 3, the WOA is illustrated in section 4, simulation results are presented in section 5; finally, the conclusions are provided in section 6.

2. LOWER LIMB REHABILITATION ROBOT DYNAMIC MODEL

The structure of a two degree of freedom (2-DOF) rehabilitation robot is shown in Figure (1), this robot consists from two link with two joints of the lower limb: a joint at the hip and a joint at the knee, link1 assists the rehabilitation of the hip and link2 for the knee. The dynamic model of this robot is was derived by (Rezage & Tokhi, 2016) depended on anthropometric data (described by Winter (2009)) for person with 74 kg in weight and 1.69 m in height (Alshatti, 2019; Winter, 2009).

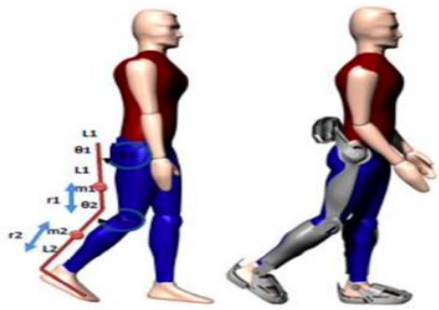

Fig. 1. 2-DOF Rehabilitation Robot (Rezage & Tokhi, 2016)

The dynamic model of the 2-DOF robot given by (Rezage & Tokhi, 2016) is expressed in matrix form as:

$$M(\theta)\ddot{\theta} + C(\theta,\dot{\theta})\dot{\theta} + G(\theta) = u(t) \tag{1}$$

where: $\theta, \dot{\theta}$, and $\ddot{\theta}$, respectively represent the angle, angular velocity, and acceleration of a robot joint vector. Matrices of human limbs for each inertia $M(\theta)$, Coriolis and centrifugal torque $C(\theta,\dot{\theta}) \in R^{(2*2)}$. The torque of gravity $(G(\theta))$ has one-dimensional vector $\in R^{(2*1)}$, $u(t)$ indicates the control signal. The obtained $M(\theta)$ are given in Eq. 2:

$$M(\theta) = \begin{bmatrix} I_1 + I_2 + m_1(L_{c1})^2 + m_2(L_1)^2 + m_2(L_{C2})^2 + 2m_2L_1L_{C2}\,cos(\theta_2) & I_2 + m_2(L_{C2})^2 + m_2L_1L_{C2}\,cos(\theta_2) \\ I_2 + m_2(L_{C2})^2 + m_2L_1L_{C2}\,cos(\theta_2) & I_2 + m_2(L_{C2})^2 \end{bmatrix} \tag{2}$$

$C(\theta,\dot{\theta})$ matrix elements can be given by Eq. 3:

$$C(\theta,\dot{\theta}) = \begin{bmatrix} -m_2L_1L_{c2}\,sin(\theta_2)\dot{\theta}_2 & -m_2L_1L_{c2}\,sin(\theta_2)(\dot{\theta}_1 + \dot{\theta}_2) \\ m_2L_1L_{c2}\,sin(\theta_2)\dot{\theta}_1 & 0 \end{bmatrix} \tag{3}$$

The gravitational vector $(G(\theta))$ elements are given in Eq. 4:

$$G(\theta) = \begin{bmatrix} m_1L_{c1}g\,sin(\theta_1) + m_2gL_1\,sin(\theta_1) + m_2gL_{c2}\,sin(\theta_1 + \theta_2) \\ m_2gL_{c2}\,cos(\theta_1 + \theta_2) \end{bmatrix} \tag{4}$$

The variables of these equations and physical parameters are defined by Table (1).

Tab. 1. The variables and physical parameters for lower limb rehabilitation robot

Parameters	Notation	Unit	Value
Length of link 1	L_1	m	0.54
Length of link 2	L_2	m	0.48
Link (1) center of mass	L_{c1}	m	0.2338
Link (2) center of mass	L_{c2}	m	0.241
Mass of link 1	m_1	kg	8
Mass of link 2	m_2	kg	3.72
Inertia of link 1	I_1	kg.m^2	0.42
Inertia of link 2	I_2	kg.m^2	0.07
Gravity acceleration	g	m/s^2	9.8
Angular Displacement of link 1	θ_1	Rad	–
Angular Displacement of link 2	θ_2	Rad	–
Angular Velocity of link 1	$\dot{\theta}_1$	Rad/s	–
Angular Velocity of link 2	$\dot{\theta}_2$	Rad/s	–
Angular acceleration	$\ddot{\theta}$	Rad/s^2	–

3. OPTIMAL SLIDING MODE CONTROLLER DESIGN

Sliding mode control has two significant advantages. The first advantage is that the system's dynamic behavior can be tailored by selecting a specific sliding function, the second advantage is that it is able to treat any uncertainties that affect the control system. The SMC can be used to control nonlinear processes that are subject to external disturbances and large model uncertainties in practice. Usually, the SMC is composed of two parts. The first part involves designing a sliding surface that satisfies design requirements for sliding motion. The second concern is with selecting a control law that will make the switching surface appealing to the system state (DeCarlo, Zak & Matthews, 1988; Hung, Gao and Hung, 1993).

The designed Optimal Sliding Mode Controller (OSMC) that is suggested in this paper for the two-link rehabilitation robot is shown in Figure (2).

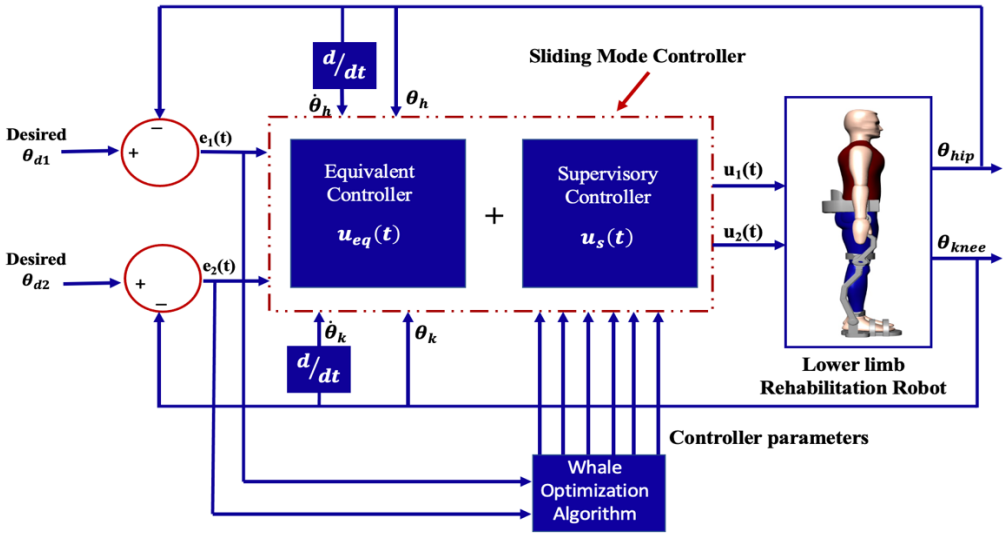

Fig. 2. The block diagram of the suggested OSMC

In order to design this controller, Eq. (1) is rewritten to the following form:

$$\ddot{\theta} = M^{-1}(\theta)\left(-C(\theta,\dot{\theta})\dot{\theta} - G(\theta)\right) + M^{-1}(\theta)u(t) \tag{5}$$

or

$$\ddot{\theta} = f(\theta,\dot{\theta}) + b(t)u(t) \tag{6}$$

where

$$f(\theta,\dot{\theta}) = M^{-1}(\theta)\left(-C(\theta,\dot{\theta})\dot{\theta} - G(\theta)\right) \tag{7}$$

and

$$b(t) = M^{-1}(\theta) \tag{8}$$

One of the important steps in designing the SMC is the selection of the sliding surface. Here in this paper, we assume the sliding surface (sliding function $s(t)$) for each link i (i= 1, and 2) is given by:

$$s(t) = k_p e(t) + k_d \dot{e}(t) + k_I \int_0^t e\,(t)dt = 0 \tag{9}$$

where $k_p = diag(k_{p_1}, k_{p_2})$, $k_d = diag(k_{d_1}, k_{d_2})$, and $k_I = diag(k_{I_1}, k_{I_2})$ are proportional, derivative, and integral gains in respectively of link i (i=1, 2), while $e(t)$=[$e_1(t)$ $e_1(t)$] and $\dot{e}(t) = [\dot{e}_1(t)\ \dot{e}_1(t)]$ are the tracking error and the derivative of the tracking error in respectively. The tracking errors will aim to zero asymptotically $\forall t \geq 0$ if system states

remain on the sliding surfaces chosen. The system state trajectories are then guided to the sliding surfaces using the control law $u(t)$. The main challenge is to select a Lyapunov function of the form $V = 0.5s^T.s < 0$ and choose such a control law (Nguyen, Ha & Nguyen, 1989):

$$\dot{V}(t) = s^T(t).s(t) < 0; s \neq 0, \tag{10a}$$

or:

$$s^T(t)\dot{s}(t) \leq -\alpha|s| = -\alpha.s^T(t).sgn(s) \tag{10b}$$

The α scalar is positive and *sgn*(.) is signum function.

The designed control law $u(t)$= [$u_1(t)$ $u_2(t)$] is selected as:

$$u(t) = b(t)^{-1}\left[u_{eq}(t) + u_s(t)\right] \tag{11}$$

where $u_{eq}(t) = [u_{eq1}(t)\ u_{eq2}(t)]$ is the equivalent control part and $u_s(t)$ = $[u_{s1}(t)\ u_{s2}(t)]$ is supervisory control part. The $u_{eq}(t)$ is given by:

$$u_{eq}(t) = \ddot{\theta}_d + C_1 e(t) + C_2 \dot{e}(t) - f(\theta, \dot{\theta}) \tag{12}$$

The $\ddot{\theta}_d$ = $[\ddot{\theta}_{d1}\ \ddot{\theta}_{d2}]$ is the desired acceleration of link *i* (*i*=1, 2), $C_1 = diag(C_{11}, C_{12})$ and $C_2 = diag(C_{21}, C_{22})$, where the parameters of C_1 and C_2 are positive optimal values of link *i* (*i*=1, 2) obtained by WOA.

the supervisory controller part $u_s(t)$ is designed as:

$$u_s(t) = s(t) + K_i\ sign(s(t)) \tag{13}$$

where $K_i = diag(K_1, K_2)$ are positive constant values. Since sign (.) function cause chattering, a nonlinear hyperbolic tangent function (tanh(.)) is used instead, so Eq.(13) becomes:

$$u_s(t) = s(t) + K_i\ tanh\big(s(t)\big) \tag{14}$$

The optimal parameters of the equivalent control part $u_{eq}(t)$ and the supervisory control part $u_s(t)$ of link1 ($C_{11}, C_{12}, k_{p_1}, k_{d1}, k_{I_1}, and\ K_1$) and link2 ($C_{21}, C_{22}, k_{p_2}, k_{d2}, k_{I_2}, and\ K_2$) are determine by Whale optimization algorithm which is described in the next section.

4. WHALE OPTIMIZATION ALGORITHM (WOA)

WOA is a modern meta-heuristic algorithm; WOA simulates the humpback whale population bubble-net as they hunt their prey. Whales are considered the world's largest mammals. Because of the spindle cells in their brain, they are intelligent. The humpback whale has a unique hunting mechanism as follows: Bubble-net feeding, this hunting activity is achieved by blowing special bubbles in a spiral or nine-shaped path. Humpback whales

(search agents) are aware of their prey's position and surround them. They believe the current optimal solution is an ideal solution and similar to the desired solution (Mohammed Umar & Rashid, 2019). Following the optimal candidate solution assignment, the other agents attempt to update their positions to align with the best search agent, this is given by Eq. 15 and Eq. 16 below which are the basic principles of the Whale optimization algorithm:

$$\vec{D} = \left|\vec{C}.\overrightarrow{X^*}(t) - \vec{X}(t)\right| \tag{15}$$

$$\vec{X}(t+1) = \overrightarrow{X^*}(t) - \vec{A}.\vec{D} \tag{16}$$

where t indicates the current iteration, $\vec{A}$ and $\vec{C}$ indicate the vectors of coefficient, $(\overrightarrow{X^*})$ denotes the optimal solution's position vector, and $\vec{X}$ indicated the position vector of a solution, and | | indicates the absolute value. The $\vec{A}$ and $\vec{C}$ vectors are determined as in Eq. 17 and Eq. 18 respectively:

$$\vec{A} = 2.\vec{a}.\vec{r} - \vec{a} \tag{17}$$

$$\vec{C} = 2.\vec{r} \tag{18}$$

Over the course of iterations, the components of are linearly decreased from 2 to 0, and $(\vec{r})$ is a random vector whose value is between [0,1]. The bubble-net mechanism is mathematically formulated as follow:

1. Shrinking encircling mechanism: the value of $\overrightarrow{A}$ in Eq. 17 is a random value in the interval [-a, a], and the value of a is reduced from 2 to 0 over iterations.
2. Spiral updating position mechanism: this mechanism calculates the distance between the whale's position and the prey's position, and the humpback's helix-shaped movement is formed as given by Eq. 19:

$$\vec{X}(t+1) = e^{bl}.\cos(2\pi l).\overrightarrow{D'} + \overrightarrow{X^*}(t) \tag{19}$$

where $\overrightarrow{D'} = \left|\overrightarrow{X^*}(t) - \overrightarrow{X(t)}\right|$ is the distance between the optimal solutions (prey) and the ith whale, b is a constant, and l is a random number in the range [–1,1].

When humpback whales swim around their prey, they implement the two mechanisms described by the mathematical model above. It is assumed that there is a 50% reasonable probability to update Whales' position as given by Eq. 20:

$$\vec{X}(t+1) = \begin{cases} \overrightarrow{X^*}(t) - \vec{A}.\vec{D} \; if \; p < 0.5 \\ \overrightarrow{D'}.e^{bl}.\cos(2\pi l) + \overrightarrow{X^*}(t) \; if \; p \geq 0.5 \end{cases} \tag{20}$$

where p is a random number in [0,1]. During the search phase, search agents scan for best solution at random and adjust their positions in response to other agents' movements. We use the $(\overrightarrow{A})$ with values > 1 or <1 to push the search agent to travel further away from the reference agent. The search phase has the following mathematical model:

$$\vec{D} = \left|\vec{C}.\overrightarrow{X_{rand}} - \vec{X}\right| \tag{21}$$

$$\vec{X}(t+1) = \overrightarrow{X_{rand}} - \vec{A}.\vec{D} \tag{22}$$

where $(\overrightarrow{X_{rand}})$ is a randomly selected position vector from of the current population (Mirjalili & Lewis, 2016). Figure (3) below illustrates the whale optimization algorithm flowchart.

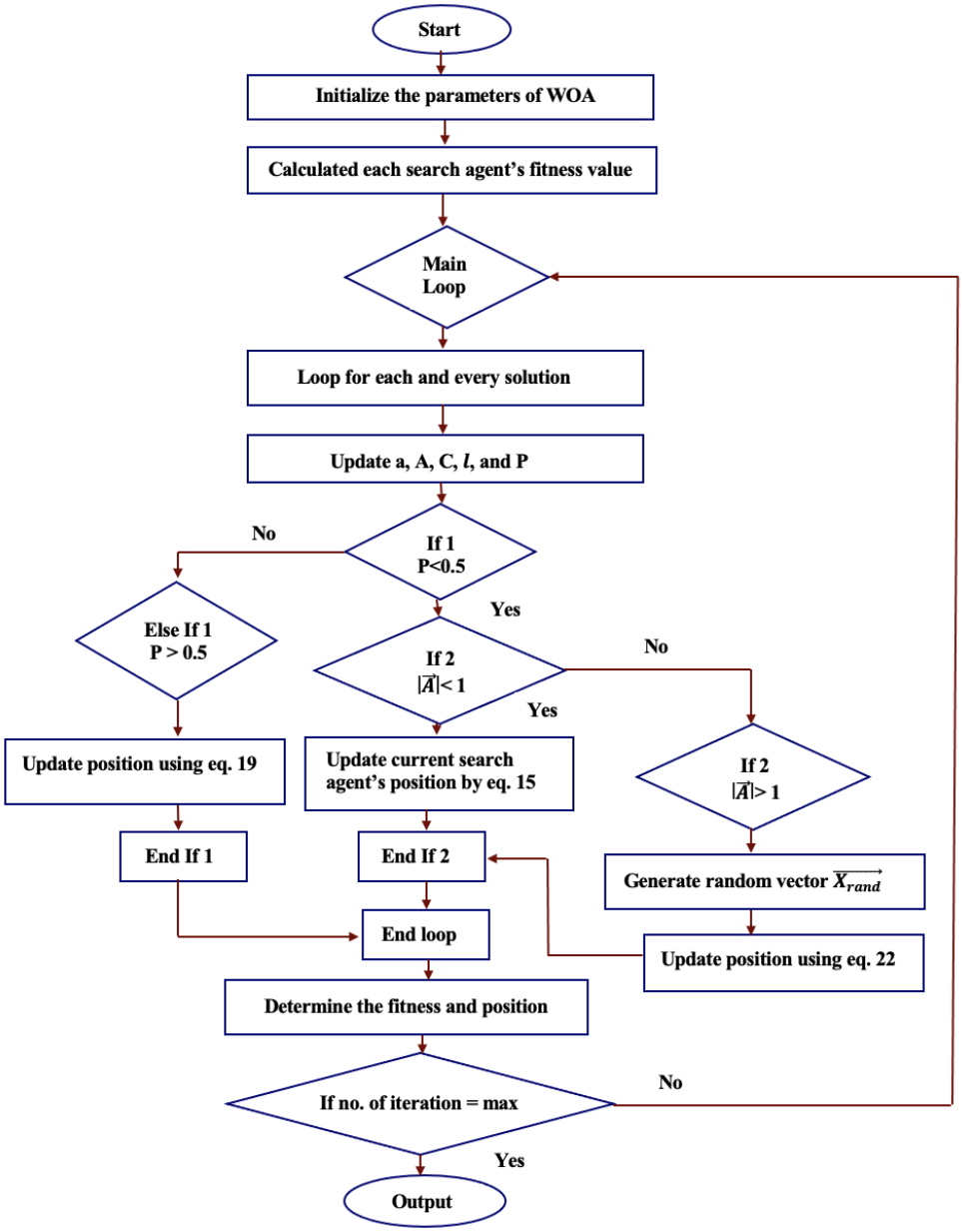

Fig. 3. The whale optimization algorithm flowchart

5. SIMULATION RESULTS

With the facility included in the version of the MATLAB software (R2019b), various simulation scenarios of lower limb rehabilitation robot are executed for both linear (step) and nonlinear paths with 10% uncertainties in parameters of the $f(\theta, \dot{\theta})$ are considered to illustrate the efficiency of the suggested controller. The parameters of the suggested controller are tuned based on the whale optimization algorithm. WOA parameters are given in Table 2, the WOA fitness function ITAE (Integral Time Absolute Errors) is given by Eq. 23:

$$F = ITAE = \int_0^{\infty} t|e(t)|dt \tag{23}$$

Tab. 2. The parameters that are used in the WOA technique.

Whale Optimization Algorithm	Parameters
No. of iterations	50
No. of search agents	10
dim (number of variables)	12
lower bound of variable n (lb)	[3 1 0.25 3 1 0.25 48 48 3 3 0.25 0.25]
upper bound of variable n (ub)	[7 4 1 7 4 1 52 52 7 7 1 1]

The optimal suggested controller parameters tuned by WOA are given in Table 3.

Tab. 3. The optimal suggested controller parameters tuned by WOA

Controller parameters of link1	Value	Controller parameters of link2	Value	ITAE
C_{11}	6.13942	C_{21}	0.767228	3352.0481
C_{12}	6.18503	C_{22}	0.619479	
k_{p1}	6.91426	k_{p2}	5.02718	
k_{d1}	0.904177	k_{d2}	0.68582	
k_{I1}	2.34528	k_{I2}	2.61624	
K_1	50.8101	K_2	50.0808	

5.1. Linear path with 10% uncertainties

The step response (positive unity step for link1, and negative unity step for link2) of the controlled lower limb rehabilitation robot (position and control signal) with 10% uncertainty in the parameters of the $f(\theta, \dot{\theta})$ function are shown in Fig.(4) and Fig.(5). These results show that the performance of the robot with the suggested controller is more efficient, where the robot flows the desired path very fast (t_s=1.605 sec. for link1 and t_s=1.468 sec. for link2) very small overshoot and zero steady-state error, with a smooth control signal. the evaluation parameters of simulation results for the suggested controller are given in Table 4.

Tab. 4. The simulation result's evaluation parameters for the OSMC

Parameters	Link1(hip)	Link2 (knee)
$M_p(\%)$	0.09	–0.12
$t_s\,(sec.)$	1.605	1.468
$e_{s.s}$	0	0
$t_r\,(sec.)$	0.421	0.366

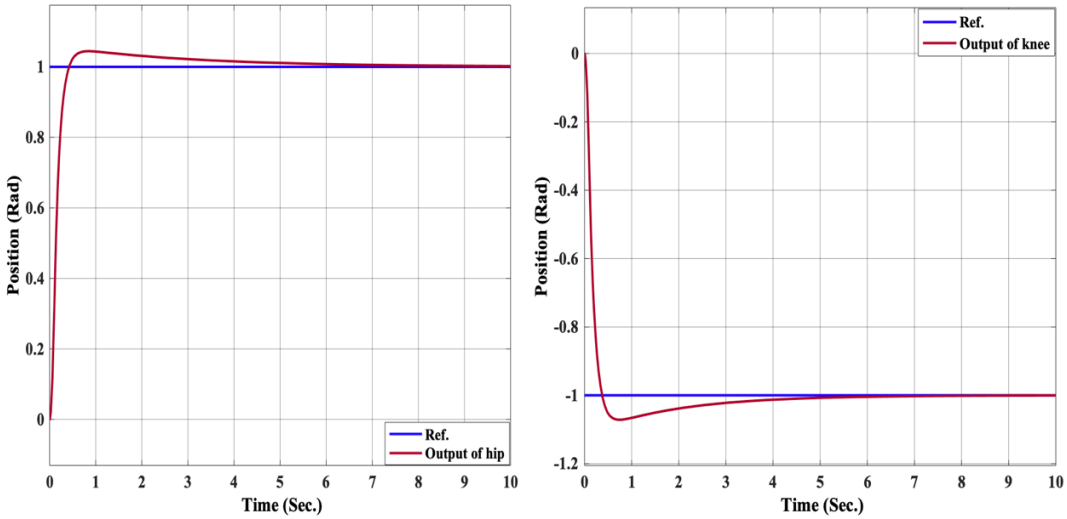

Fig. 4. The position of hip link and knee link for linear path

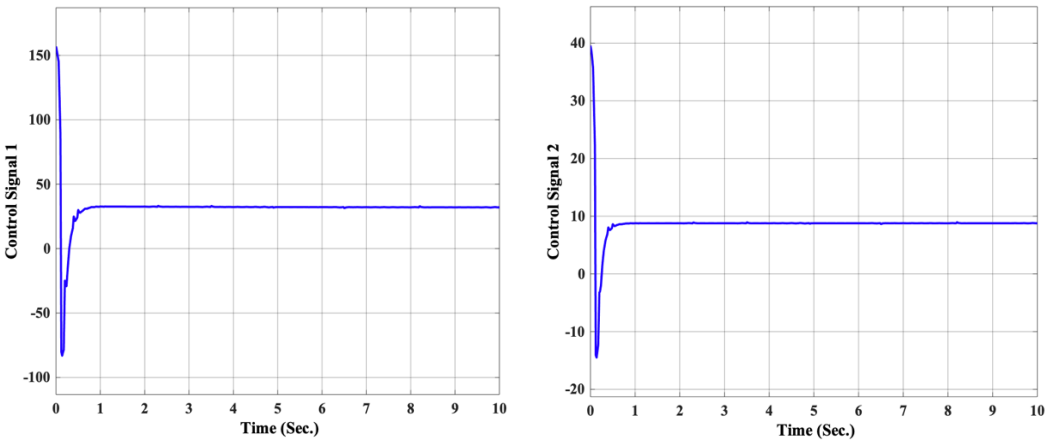

Fig. 5. The control signals for linear path

5.2. Nonlinear path with 10% uncertainties

The simulation results of the lower limb rehabilitation robot with the suggested OSMC tested by the desired nonlinear input signal ($x_{d1} = {}^{\pi}/_{4} + (1 - cos3t)$ for link1 and $x_{d1} = {}^{\pi}/_{6} + (1 - cos5t)$ for link2) with 10% uncertainty in the parameters of the $f(\theta, \dot{\theta})$ function are illustrated in Fig. 6 and Fig.7; these results show that despite the nonlinearity of the input signal, the WOA optimized controller converges with precise control over the plant. It achieves very good performance parameters and zero error.

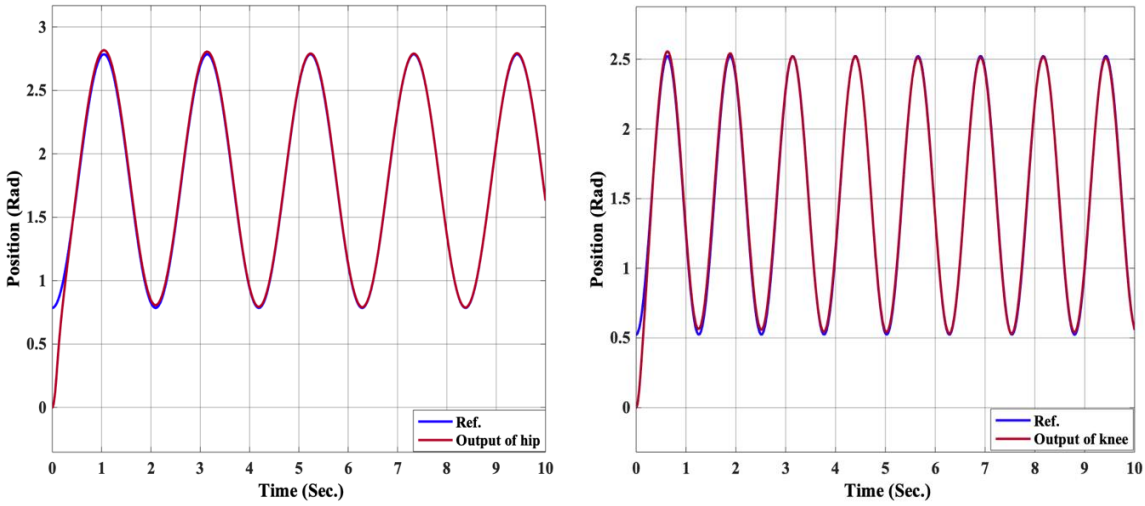

Fig. 6. The position of hip link and knee link for nonlinear path

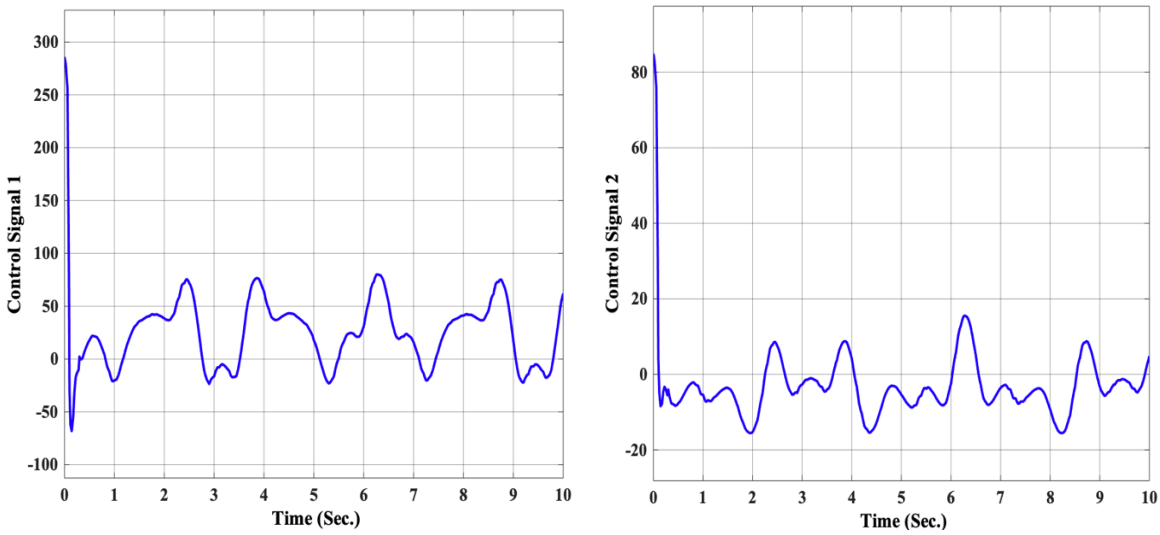

Fig. 7. The control signals for nonlinear path

6. CONCLUSIONS

The main aim of this work was to design an Optimal Sliding Mode Controller (OSMC) for tracking the desired trajectory and improve the performance of a two-link lower limb rehabilitation robot. The parameters of the SMC were optimized by using a Whale Optimization Algorithm (WOA). The transient parameters of the obtained results show the effectiveness of the suggested controller achieving zero steady-state error in two scenarios, the linear with 10% uncertainty and the nonlinear with 10% uncertainty in parameters of the $f(\theta, \dot{\theta})$ function. The controlled output settled within the vicinity of the desired value after 1.605 sec. and 1.468 sec. for the linear case. These results show reliability of the proposed approach and suggests investigating their capabilities in more complex scenarios as well as physical implementation.

Acknowledgment

Praise and thanks be to God who made all of this possible. The author wants to share the deep appreciation for the excellent advice, motivation, and assistance provided to her supervisors, Professor Dr. Ekhlas H. Karam and Assistant Professor Dr. Muayed S AL-Huseiny.

REFERENCES

Abbasimoshaei, A., & Mohammadimoghaddam, M. (2020). *Design for a New Hand Rehabilitation* (Vol. 1). Springer. https://doi.org/10.1007/978-3-030-58147-3

Almaghout, K., Tarvirdizadeh, B., Alipour, K., & Hadi, A. (2020). Design and control of a lower limb rehabilitation robot considering undesirable torques of the patient's limb. *Proceedings of the Institution of Mechanical Engineers, Part H: Journal of Engineering in Medicine*, *234*(12), 1457–1471. https://doi.org/10.1177/0954411920947849

Alshatti, A. (2019). *Design and Control of Lower Limb Assistive Exoskeleton for Hemiplegia Mobility* (Doctoral dissertation). University of Sheffield.

Babaiasl, M., Goldar, S. N., Barhaghtalab, M. H., & Meigoli, V. (2015). Sliding mode control of an exoskeleton robot for use in upper-limb rehabilitation. *International Conference on Robotics and Mechatronics, ICROM 2015*, 694–701. https://doi.org/10.1109/ICRoM.2015.7367867

DeCarlo, R. A., Zak, S. H., & Matthews, G. P. (1988). Variable structure control of nonlinear multivariable systems: a tutorial. *Proceedings of the IEEE*, *76*(3), 212–232, https://doi.org/10.1109/5.4400

Furlan, A. D., Irvin, E., Munhall, C., Giraldo-Prieto, M., Master, R. M., Danak, S., Costante, A., Pitzul, K. B., Bhide, R. P., Marchenko, S., Mahood, Q., David, J. A., Flannery, J. F., & Bayley, M. (2021). Rehabilitation service models for people with physical and/or mental disability living in low- and middle-income countries: A systematic review. *Journal of Rehabilitation Medicine*, *50*(6), 487–498. https://doi.org/10.2340/16501977-2325

Hung, J. Y., Gao, W., & Hung, J. C. (1993). Variable Structure Control : A Survey. *IEEE Trans. Ind. Electron*, *40*(1), 2–22.

Liu, J., Zhang, Y., Wang, J., & Chen, W. (2018). Adaptive sliding mode control for a lower-limb exoskeleton rehabilitation robot. *Proceedings of the 13th IEEE Conference on Industrial Electronics and Applications, ICIEA 2018* (pp. 1481–1486). IEEE. https://doi.org/10.1109/ICIEA.2018.8397943

Maalej, B., Medhaffar, H., Chemori, A., & Derbel, N. (2020). A Fuzzy Sliding Mode Controller for Reducing Torques Applied to a Rehabilitation Robot. *Proceedings of the 17th International Multi-Conference on Systems, Signals and Devices, SSD 2020* (pp. 740–746). https://doi.org/10.1109/SSD49366.2020.9364130

Mirjalili, S., & Lewis, A. (2016). The Whale Optimization Algorithm. *Advances in Engineering Software*, *95*, 51–67. https://doi.org/10.1016/j.advengsoft.2016.01.008

Mohammed, H. M., Umar, S. U., & Rashid, T. A. (2019). A Systematic and Meta-Analysis Survey of Whale Optimization Algorithm. *Computational Intelligence and Neuroscience*, *2019*, 8718571. https://doi.org/10.1155/2019/8718571

Nguyen, T. V. M., Ha, Q. P., & Nguyen, H. T. (1989). *A Chattering-Free Variable Structure Controller for Tracking of Robotic Manipulators*. Retrivied from https://www.araa.asn.au/acra/acra2003/papers/02.pdf

Rezage, G. Al, & Tokhi, M. O. (2016). Fuzzy PID control of lower limb exoskeleton for elderly mobility. *2016 20th IEEE International Conference on Automation, Quality and Testing, Robotics, AQTR 2016 – Proceedings* (pp. 1–6). IEEE. https://doi.org/10.1109/AQTR.2016.7501310

Rodrigues, A., & Rodrigues, A. (2018). Prise en charge des traumatisés médullaires. *Le Praticien En Anesthesie Reanimation*, 8–11. https://doi.org/10.1016/j.pratan.2018.08.010

Rupal, B. S., Rafique, S., Singla, A., & Singla, E. (2017). Lower-limb exoskeletons : Research trends and regulatory guidelines in medical and non-medical applications. *International Journal of Advanced Robotic Systems*, *November-December*, 1–27. https://doi.org/10.1177/1729881417743554

Saryanto, W. Y., & Cahyadi, A. I. (2016). Modeling and Design of Low Cost Lower Limb Rehabilitation Robot Control System for Post - Stroke Patient using PWM Controller. *International Journal of Mechanical & Mechatronics Engineering IJMME-IJENS*, *16*(1), 101–108.

Winter, D. A. (2009). *Biomechanics And Motor Control Of Human Movement* (Fourth Ed.). John Wiley & Sons, Inc.

Yang, T., & Gao, X. (2020). Adaptive Neural Sliding-Mode Controller for Alternative Control Strategies in Lower Limb Rehabilitation. *IEEE Transactions on Neural Systems and Rehabilitation Engineering*, *28*(1), 238–247. https://doi.org/10.1109/TNSRE.2019.2946407

Zhou, J., Zhou, Z., & Ai, Q. (2016). Impedance Control of the Rehabilitation Robot Based on Sliding Mode Control. *Mechanical Engineering and Control Systems*, 135–140. https://doi.org/10.1142/9789814740616_0030

Applied Computer Science, vol. 17, no. 3, pp. 60–72
doi: 10.23743/acs-2021-21

Submitted: 2021-07-14 | Revised: 2021-09-07 | Accepted: 2021-09-21

Multi-Robot Systems, Formation control, Behavior-Based Control, Switching strategy, Stateflow

Kuppan Chetty RAMANATHAN [0000-0002-2419-938X]*,
Manju MOHAN [0000-0001-5021-9770]*,
Joshuva AROCKIA DHANRAJ [0000-0001-5048-7775]*

BACKWARD MOTION PLANNING AND CONTROL OF MULTIPLE MOBILE ROBOTS MOVING IN TIGHTLY COUPLED FORMATIONS

Abstract

This work addresses the development of a distributed switching control strategy to drive the group of mobile robots in both backward and forward motion in a tightly coupled geometric pattern, as a solution for the deadlock situation that arises while navigating the unknown environment. A generalized closed-loop tracking controller considering the leader referenced model is used for the robots to remain in the formation while navigating the environment. A tracking controller using the simple geometric approach and the Instantaneous Centre of Radius (ICR), to drive the robot in the backward motion during deadlock situation is developed and presented. State-Based Modelling is used to model the behaviors/motion states of the proposed approach in MATLAB/STATEFLOW environment. Simulation studies are carried out to test the performance and error dynamics of the proposed approach combining the formation, navigation, and backward motion of the robots in all geometric patterns of formation, and the results are discussed.

1. INTRODUCTION

Motion planning and control of multiple mobile robots moving in tightly coupled formation garnered enormous research interest in the past two decades owing to the applications of such systems in security and surveillance, defense, disaster management, driverless vehicle platoons, and material handling in industrial manufacturing environments. The essential problem in such tightly coupled systems is to make the systems efficiently plan their paths by navigating the environment in a coordinated fashion avoiding the obstacles as well as each other to achieve its goal. Therefore, it refers to the problem of developing a closed-loop control strategy that controls the relative position and orientation between the group of robots during its fly (Werger & Mataric, 2001; Barfoot & Clark, 2004; Alonso-Mora, Baker & Rus, 2017; Kuppan Chetty, Singaperumal & Nagarajan 2011a, 2011b; Kuppan Chetty et al., 2011).

* Hindustan Institute of Technology and Science, Centre for Automation and Robotics, School of Mechanical Sciences, OMR, Rajiv Gandhi Salai, Padur, Chennai - 603103, India, kuppanc@hindustanuniv.ac.in.

As reported in various literature, numerous approaches, algorithms, topologies for motion planning and control of multiple robots in tightly coupled formation and its advantages, disadvantages, and applications are addressed in (Arkin, 1998; Dougherty et al., 2004; Li & Xiao, 2005; Mataric & Michaud, 2008; Kuppan Chetty et al., 2012; Xu et al., 2014; Lee & Chwa, 2018; Wang & Philips, 2018). Behavior-Based and Leader-Follower approaches are commonly used and widely accepted by researchers due to their simple and scalable nature (Soni & Hu, 2018; Wang & Philips, 2018). However, the major limitation is that the ability of the system remains in a stable formation in dynamically changing unknown environments filled with obstacles.

In most of the studies, found in the literature, the robots are made to move in the formation by specifying the trajectory of the leader robots and make the other robots efficiently track the assigned leader without perturbing the formation throughout the fly (Li & Xiao, 2005; Kuppan Chetty, Singaperumal & Nagarajan 2011a, 2011b; Kuppan Chetty et al., 2011, 2012). Though, when it comes to guiding the robots in the unknown environment, apart from tightly coupled formation, the robots also need to plan their paths to reach their particular goal by avoiding collision between themselves and obstacles in the environment of interest. Under such conditions, as the number of robots increases in the group, the control methods reported in the literature fails due to their centralization and requirement of higher communication bandwidth (Li & Xiao, 2005; Kuppan Chetty et al., 2011; Soni & Hu, 2018; Wang & Philips, 2018). Further, it is difficult to design and model the system in a traditional manner. Therefore, it needs a distributed controller that combines formation planning along with the navigational capabilities of the group of robots in achieving a stable formation with wide communication capabilities between the group members to have knowledge about their states and the actions of their teammates.

One such control strategy is addressed and employed in (Kuppan Chetty et al., 2011, 2012), where a hybrid control approach combining the advantages of behavior-based and leader-follower approach is used to control the group of mobile robots in tightly coupled formation by planning its path, avoiding an obstacle in the dynamic unknown environments. In this approach to achieve the desired objective of the formation planning and navigation in a distributed manner, the total functionality of the multi-robot system is decomposed into functional behaviors such as Navigation and Formation, based on the motion states of the robots utilizing the methodology of the behavior-based reactive approach. The formation amongst the robot is achieved by a tracking controller using the leader-follower approach and the navigation and motion planning by using the heuristic controllers coupled in the layered manner as suggested in (Arkin, 1998; Mataric,2008). The important aspect of controlling multiple robots in the formation is the active obstacle avoidance on the follower robots, which is very crucial for the robots to remain in the closed defined geometric pattern through the exchange of leaderships between the robots is also addressed in (Kuppan Chetty et al., 2011, 2012).

Even though the robots are able to move in a closed defined formation along with navigational and obstacle avoidance on both leader and follower robots by exchanging the leaderships, there exists a deadlock situation when all the robots experience obstacles on their path at the same time. This deadlock situation arises as a result of the confusion in lending their leadership to one of the robots in the group. One possible solution, in this case, is to make all the robots plan their motion in the backward direction without changing their orientation to a safer distance and continue to plan its path afterwards. However, in most of

the studies reported in the literature, the tracking controller is designed only to track the leader robot moving in the forward direction using the kinematics of the robots. Therefore, addressing this deadlock situation and backward motion is critically important amongst the group of robots moving in a tightly coupled formation navigating unknown environments.

The organization of the manuscript is as follows. Literature on the backward motion control of multiple mobile robots, its limitations, and the need for a distributed switching control strategy to address the deadlock situation is described in section 2. The detailed description and methodology on the design of switching control strategy and theoretical formulation for backward motion controller are presented in section 3. Section 4 deals with the modeling and simulation studies in MATLAB/STATEFLOW environment. The simulation results that are obtained to validate the performance of the proposed approach are discussed in detail in section 5. Finally, the outcome of this work is concluded and the scope for further improvements is presented in section 6.

2. RELATED WORK

In recent times, the backward motion control of robots moving in a tightly coupled formation garnered enormous research interest amongst researchers. Autonomous backward navigation of mobile robots using remembered landmarks is addressed in (Petukhov & Rachkov, 2009). The reference points along the trajectory are used to design the control algorithm for the control of robot motion. This method maintains tight coupling between the robot and makes an alternative decision commanding the robot in backward motion for some distance to avoid an obstacle in its path. However, the major drawback of this method is the complex computational algorithm used to compute the reference points and coordinating the backward motion of the robots is only for a minimum distance in real-time.

A nonlinear smooth feedback tracking control law using the line- of sight method and PID algorithm for the mobile robot group tracking a rectilinear path in the backward motion in an in inline formation is proposed and addressed in (Ma et al., 2014; Cheng et al., 2017). Similarly, motion control of n passive trailers off-hooked with the mobile robot in backward motion is addressed in (Chung et al., 2011; Petrov, 2010).

Here leader robot is considered as a truck and the follower robots as the trailer in in-line formation with the separation distance between them is considered a hooked distance. The trajectory-based tracking control algorithm is addressed where the trailers trajectory is computed using the set of equations using the kinematic model of the robots and trailer considering the off hooked distance and the steering angle as the parameters in leader – referenced model. Although the results show the efficient control of robots in backward motions, the main disadvantage is that the presence of a set of non-linear equations in the tracking controller and linearizing the models to obtain the reference trajectory makes the system complex to understand and increases the computational cost as well as hinders the performance of the system. The major disadvantage is this system works only during the backward motion.

In the approaches that have been devised in the literature for the backward motion of the mobile robots, the backward motion control problem is formulated as a trajectory-following problem, rather than as the control of independent, generalized coordinates. The motion control is complicated because the kinematic model is represented by highly nonlinear equations.

The reversing of robots is an open-loop unstable control problem. In addition, the robots must incorporate the navigation capabilities along with the two major important aspects of alignment and synchronization while positioning the robots in the tightly couple formation moving in the backward direction are to be considered. Therefore, it is necessary to develop a distributed control strategy able to drive the robots in both the backward and forward motion during navigation in tightly coupled geometric patterns for achieving a stable formation during its fly.

Inspired from the observations from the literature, a distributed switching control strategy in behavior-based approaches, like the one addressed in (Alonso-Mora, Baker & Rus, 2017; Kuppan Chetty et al., 2011; Dougherty et al., 2004) is developed incorporating the backward motion control of robots is developed and presented in this work. A tracking controller addressed in (Kuppan Chetty et al., 2011; Dougherty et al., 2004) considering the leader referenced model is used for the robots to track its leader's path while navigating the environment. When a deadlock situation arises, the controller switches to the backward motion tracking controller where the robot motion control is developed using a simple geometric approach using the Instantaneous Centre of Radius (ICR) and differential drive kinematics of the robots. The proposed approach combines the formation planning, navigation, and obstacle avoidance of robots addressing the deadlock situations of driving the robots effectively in the backward motion without perturbing the formation of the robots. The performance and error dynamics of the proposed approach are investigated through simulation studies in MATLAB/STATEFLOW environment.

3. METHODOLOGY

In order to meet the collective objective of the robot group to efficiently navigate the environment along with a stable tightly coupled formation, a layered distributed control architecture, where the fundamental behaviors/motion states of the robots are considered as components is developed and presented in (Kuppan Chetty et al., 2011, 2012) as shown in Figure 1. In this layered design, the total functionality of the system is divided into a set of functional behaviors such as the lower-level navigation and higher-level formation, based on the motion states of the robots, using the methodology of the behavior-based reactive approach designed by (Arkin, 1998; Mataric, 2008). These two levels work on individual goals concurrently and asynchronously, where the entire sets of behaviors are swapped in and out of execution which yields the collective task upon integration, for achieving the goals such as navigation and formation. The behavior/motion states are selected by the robots based on the information perceived by the robot sensors explicitly and implicitly from the environment during the fly. More details on the realization of individual behaviors, assumptions used to formulate the behaviors, arbitration, and coordination techniques could be found in (Kuppan Chetty et al., 2011, 2012).

Considering the objective of driving the robots in the backward motion without losing the formation, the higher-level formation behavior is decomposed into two and arbitered using the priority-based arbitration technique as in the rest of the system as shown in Figure 1, which is the modified form from (Kuppan Chetty et al., 2011, 2012). The decomposed behaviors are the generalized tracking controller which uses the theoretical formulation of closed-loop feedback control technique using the kinematics of the robots and the geometric

controller using the Instantaneous Centre of Curvature/Radius (ICC/ICR) based on the velocities of the robots, responsible for driving the robots in the backward motion. These controllers swap themselves in and out of execution based on the relative motion of their leader, to remain in the defined formation. In both cases, the kinematics of a non-holonomic differential drive robot is considered in the realization of the control law. The detailed formulation of the generalized tracking controller and the geometric controller is discussed in the subsequent sections.

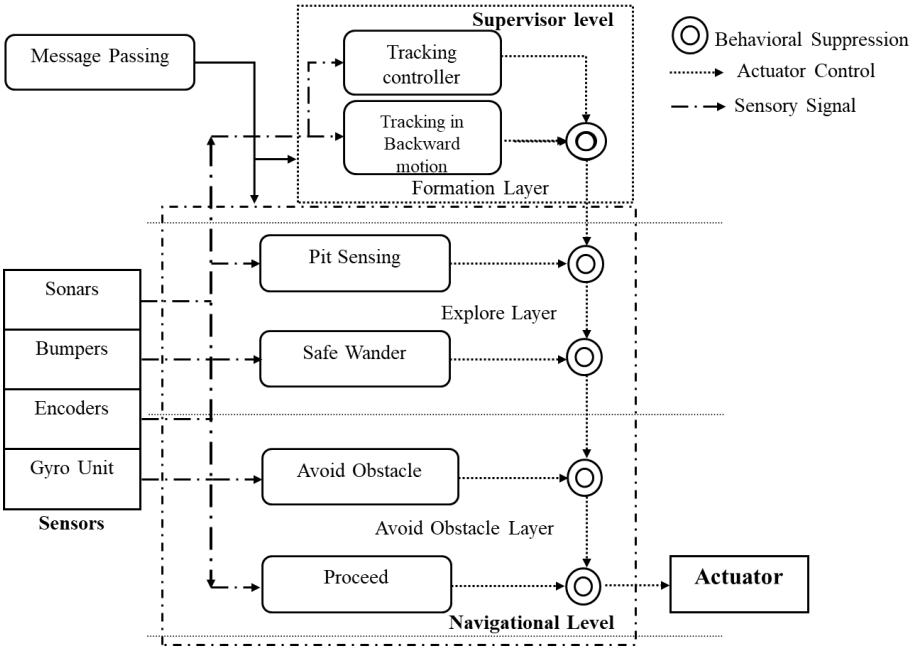

Fig. 1. Behavior-Based Switching Control Architecture for Multi-Robot Formation with modified formation layer

3.1. Generalized Tracking Controller

The generalized tracking controller used to position the robot in the tightly coupled formation is modeled based on the kinematics of the non-holonomic wheeled mobile robot in Figure 2. Let R_1 be the robot designated as leader and R_2 be the robot designated as a follower in which the direction of motion represents the x-axis, the robot frame. The robot R_2 is made to follow the leader R_1 in any geometric pattern such as inline, collateral, and parallel as illustrated in Figure 2. The posture of the robots in the group is given by x_L, y_L, θ_L and x_{Fi}, y_{Fi}, θ_{Fi} where L and F represent the leader and follower, respectively. Let l_d be the desired linear separation and φ_d be the desired angular separation. it is necessary to maintain the desired linear and angular separation between the robots to remain in the tightly coupled formation. The translational and rotational velocities of the leader and follower robots are υ_L, ω_L and υ_F, ω_F respectively. The closed-loop tracking controller is designed such that the follower robots estimate their wheel velocities in a way that the formation/separation errors (linear and angular) reduce asymptotically to zero and position themselves in the desired

geometric pattern with its leader as shown in Figure 3. Here the control problem reduces to a trajectory tracking control problem rather than the regulation problem of the follower by observing the leader's information.

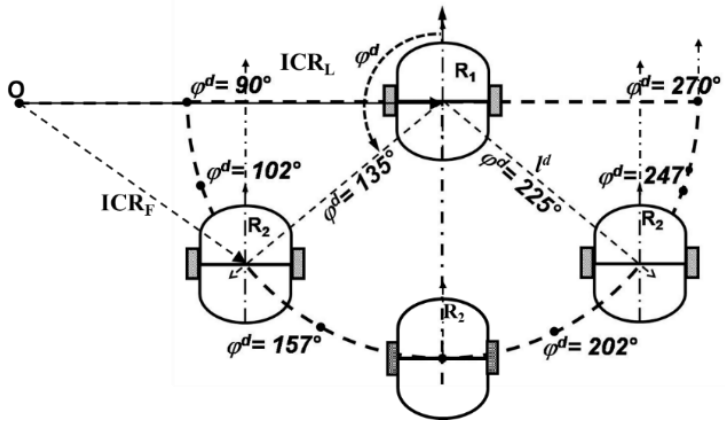

Fig. 2. Position of Robots in desired linear and angular separation describing the formation topologies

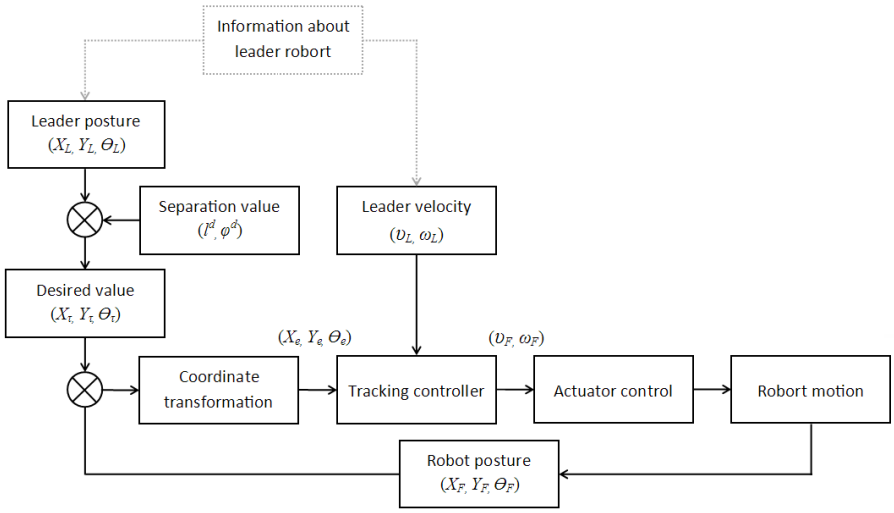

Fig. 3. Generalized tracking controller illustrated in (Kuppan Chetty, et al., 2011, 2012)

The details of the formulation of the trajectory tracking controller could be observed in (Kuppan Chetty et al., 2011, 2012). Hence, based on the kinematic model, the position of the robots and error coordinates in the robot frame and feedback linearization as given in (Kuppan Chetty et. al., 2012), the tracking control law for estimating the velocities υ_F and ω_F of the follower robots is obtained as:

$$\begin{bmatrix} v_F \\ \omega_F \end{bmatrix} = \begin{bmatrix} cos\,\theta_e & l^d\,sin(\,\varphi^d + \theta_e) \\ \frac{sin\,\theta_e}{h} & \frac{l^d\,cos(\varphi^d+\theta_e)}{h} \end{bmatrix} \begin{bmatrix} v_L \\ \omega_L \end{bmatrix} + \begin{bmatrix} k_1 & 0 \\ 0 & \frac{-k_2}{h} \end{bmatrix} \begin{bmatrix} x_e \\ y_e \end{bmatrix} \tag{1}$$

where,

$$x_e = \begin{bmatrix} \left(X_L - l^d\,cos(\,\phi^d + \theta_L) - X_F\right) cos\,\theta_F \\ +\left(Y_L - l^d\,sin(\,\phi^d + \theta_L) - Y_F\right) sin\,\theta_F \end{bmatrix} \tag{2}$$

$$y_e = \begin{bmatrix} -\left(X_L - l^d\,cos(\,\phi^d + \theta_L) - X_F\right) sin\,\theta_F \\ +\left(Y_L - l^d\,sin(\,\phi^d + \theta_L) - Y_F\right) cos\,\theta_F \end{bmatrix} \tag{3}$$

being the positional error between the leader and follower robots and k_1 and k_2 are controller gains that are constant positive integers greater than zero, which guarantee the system stability.

3.2. Geometric Controller during deadlock situation

As the deadlock situation arises as mentioned in section 1, one possible and logical solution is to reverse i.e., drive the entire robot system in a backward direction to a safer distance without losing its geometric patterns. In most of the studies found in the literature and the tracking controller illustrated above, motion control is difficult because the kinematic model is represented by highly nonlinear equations. Further, the motion planning in the backward direction of robots is an open-loop unstable control problem and formulated as a trajectory following problem rather than the control of independent, generalized coordinates as addressed in (Kuppan Chetty et. al., 2011, 2012). However, this system fails, when the entire focus is on reversing the robot platoons without losing their geometric pattern and maintaining the desired separation and orientation. The main disadvantage is that the presence of a set of non-linear equations in the tracking controller and linearizing the models to obtain the reference trajectory for the robots makes it complex to understand and increases the computational cost as well as hinders the performance of the system.

To address this issue, a tracking controller is proposed using a simple geometric relationship between the robot using the linear and angular separation, l_d and φ_d. We know that there are two critical parameters l and φ that determine the geometric shape of the robot formation and it does not change the pattern throughout its fly even if it is driven in forward or backward motion. Also, we know that the parameters that govern the motion of the robot are the translational and rotational velocities v_L, ω_L and v_F, ω_F respectively. The robots are driven in any given trajectory based on controlling the velocities that govern a rolling motion on the wheels of the robots and it rotates about a point known as the Instantaneous Centre of Curvature (ICC)/Instantaneous Centre of Radius (ICR):

$$ICR = \frac{v}{\omega} \tag{4}$$

From Figures 2 and 3, it could be observed that ICC and ICR play an important role in making the robots to remain in the formation keeping the required linear and angular separation while following a curvilinear trajectory. The ICC of the leader robot is given by

the distance between point O and the axis of R_1 and the ICC/ICR of the robot designated as a follower is given by the distance between point O and the axis of R_2 respectively. The ICC/ICR of the robots designated as leader and follower is determined as in equation (5):

$$ICR_L = \frac{v_L}{\omega_L} \text{ and } ICR_F = \frac{v_F}{\omega_F} \tag{5}$$

While in tightly coupled formation, Robot R_2 designated as a follower is required to follow the robot R_1 in a defined linear and angular separation. From the geometric aspect and the literature of trajectory tracking between the robots, it could be observed that the ICR of the robots designated as follower arranged in any geometric pattern with the desired linear and angular separation could be found using the law of sines as

$$ICR_F = ICR_L - l^d \, sin(\varphi^d) \tag{6}$$

Substituting equation (5) in the equation, it becomes

$$\frac{v_F}{\omega_F} = \frac{v_L}{\omega_L} - l^d \, sin(\varphi^d) \tag{7}$$

When, v_L, ω_L, l^d, φ^d is known, then assuming either v_L=v_F or ω_L=ω_F, the required wheel velocities of the follower robot could be determined which positions the follower robot in the desired separation with respect to the leader mimicking its motion behavior. This approach of estimating the wheel velocities, converts the backward motion problem from the trajectory tracking problem to the trajectory following problem and eliminates the set of nonlinear equations, and makes the computations simple.

4. SIMULATION STUDIES

Simulation studies are carried out to investigate the performance of the developed backward motion tracking controller. Simulation studies are carried out in a MATLAB/ STATEFLOW environment. State flow is chosen because, it is an interactive graphical design and development tool that works with Simulink to model and simulate complex systems modeled as finite state machines, also called reactive event-driven systems based on motion states of the robots. In this work, the complex multi-robot system is modeled as a layered reactive system, where the inherent behaviors work on individual goals asynchronously, upon integration used to achieve the overall task of stable formation without losing its geometric patterns. The major advantage of such an approach is the functional interactions between the state machines are investigated in terms of state transitions in the system either with discrete behaviors modeled by Finite State Machines or the continuous behaviors modeled algebraically using differential equations. Therefore, this work follows the similar method called state-based modeling addressed in (Kuppan Chetty et al., 2011, 2012), to model and simulate the individual task achieving behaviors mentioned in Figure 1.

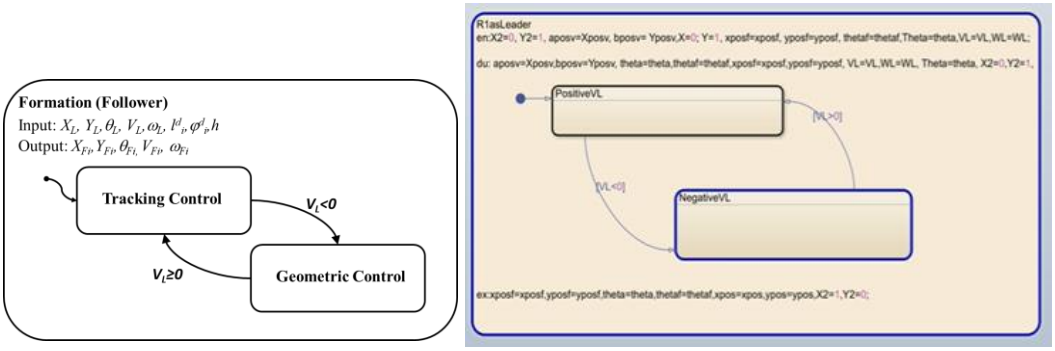

(a) **(b)**

Fig. 4. (a) Behavior implementation in State flow; (b) Response of switching between control between behaviors

The detailed implementation of the layered control approach in a state flow environment could be found in (Kuppan Chetty et al., 2011, 2012). Figure 4 shows the implementation of the formation control behavior of the multi-robot system, where the task achieving behaviors such as the tracking controller and the geometric controller responsible for driving the robots in forward and backward directions are modeled as temporal states. The lines with the arrow-heads between the states represent the state transitions that are necessary to provide the interconnections between the states/behaviors. The transitions from the tracking controller and the geometric controller occur based on the explicit information of the leader robots wheel velocities received and used as the state transition conditions. The arrow with a dotted head indicates the default state while the controller enters the formation motion state. The necessary information such as the postures and velocities of the robots in the group are received as explicit information through inter-robot communication.

The idea of switching between both the formation state is, whenever the velocities of the leader robot are less than a positive integer, i.e. driven in a negative direction, the controller switches the state from the generalized tracking controller to the geometric controller to drive the robots designated as a follower to mimic the behavior of the leader robot. This is shown in Figure 4 (b) as the result of switching between the behaviors in real-time simulation studies in a state flow environment. The necessary entry variables and exit variables, response output of the corresponding behavior, separation errors, and motor control data obtained as the results are recorded. The required interfaces for the statecharts to the inputs and outputs are created in the Simulink environments. The required sensor inputs for perception by the robots are created as discrete events and data in the signal builder of the Simulink environment as given in (Kuppan Chetty et al., 2011, 2012).

Simulation studies are carried out for 200 units in time frame with three robots R_1, R_2, and R_3 navigating the environment of interest in a wedge-shaped geometric pattern. At any instance of time Robot R_1 is considered as the leader robot, and R_2, R_3 are designated as follower robots, tracking the leader with the desired linear and angular separation of 1000 mm and 135° and 225° respectively placing the follower robots in either side of the leader, respectively. Leader navigates the environment with the lower-level navigational behaviors with the piecewise constant translational and rotational velocity of ±150 mm/s and ±3°/s making an ICC/ICR of 2.9 m.

The leader robot is made to reverse its direction if all the robot experiences obstacles on its path and this condition are simulated in the signal builder that all sensors provide a logically high signal at the same instant. The dimensional parameters of the differential drive kinematics of the *Pioneer P3DX* open-ended robot research platform are considered. The initial values of the robots R_1, R_2 and R_3 are given and ensured that the postures of the R_2 and R_3 are at arbitrary positions to test the efficiency of the tracking controller to make the robots remain in the stable formation. Postures and wheel velocities of all the robots are taken and logged as the output in the data logger. The wheel velocities of all the robots are constrained and bounded by the conditions $\upsilon < \upsilon_{max} <\pm 300\ mm/s$ and $\omega < \omega_{max} < \pm 40\ °/s$, considering the kinematics of the P3DX robot research platform.

5. RESULTS AND DISCUSSION

Figure 5 to 7 illustrates the results that have been obtained as the performance of the existing tracking controller and proposed geometric controller, controlling the robot group is tightly coupled wedge-shaped geometric pattern during forward and backward motion robots. Figure 5 (a), Figure 6 (a), and Figure 7 (a) show the performance of the generalized tracking controller in the backward motion while navigating the environment. Similarly, Figure. 5 (b), Figure 6 (b), and Figure 7 (b) show the performance of the geometric controller in the backward motion. It is also observed that the switching control strategy developed using the behavior-based approach effectively switches its behavior from the generalized tracking to the proposed geometric tracking when all the robots experience the obstacles and driving in the backward motion.

Figure 5 shows the trajectory of the robots during the fly, navigating the environment by changing its direction of motion. The efficiency of the generalized tracking controller could be observed from both (a) and (b), whereby it makes the robots remain in the tightly coupled formation during the fly. However, it could be observed from (a) that the tracking controller fails to make the robots remain in the formation during backward motion with maximum separation errors and goes into the uncontrollable state, which is indicated by a dotted rectangle in Figure 5 (a).

This is because the linearized model makes the rotational velocities of the robot R_2 and R_3 go beyond the constraint values. From Figure 5 (b), it could be observed that the geometric controller safely drives the robots in the backward motion keeping its tight geometric pattern, as this works by calculating the wheel velocities of the follower robots by the *ICC/ICR* relationship with its leader robot as given in equation (7) and guides the robot without losing its geometric pattern by mimicking the motion of the leader. It could also be observed from Figure 4 (b) that the switching control strategy switches from the geometric controller to the tracking controller once the backward motion is completed i.e., wandering to a safer distance to avoid the obstacle.

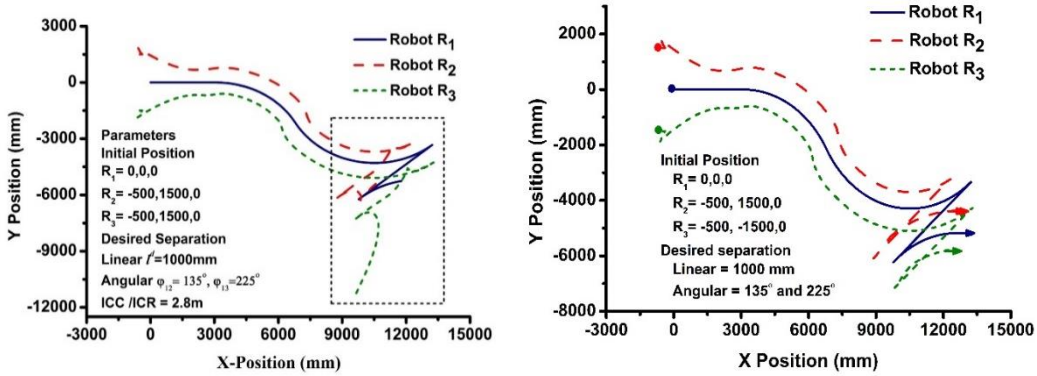

(a) **(b)**

Fig. 5. (a) Trajectory of robots in wedge-shaped formation exhibiting uncontrolled motion using a tracking controller; (b) The trajectory of robots in wedge-shaped formation exhibiting controlled motion using proposed controller during backward motion

Figure 6 (a) and (b) illustrates desired linear and angular separation between the robots, where it could be observed that the generalized tracking controller could not be able to guide the robots to remain in the formation during backward motion, However, the geometric controller makes the robot to remain in the formation during its fly.

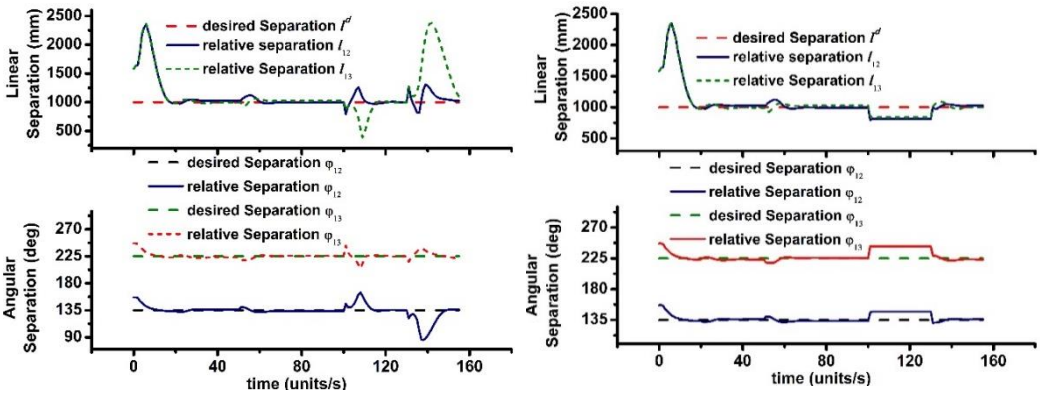

(a) **(b)**

Fig. 6. (a) Linear and angular separation of robots in wedge-shaped formation exhibiting loss of formation using generalized tracking controller; (b) Linear and angular separation of robots in wedge-shaped formation exhibiting tightly coupled separation using proposed controller during backward motion

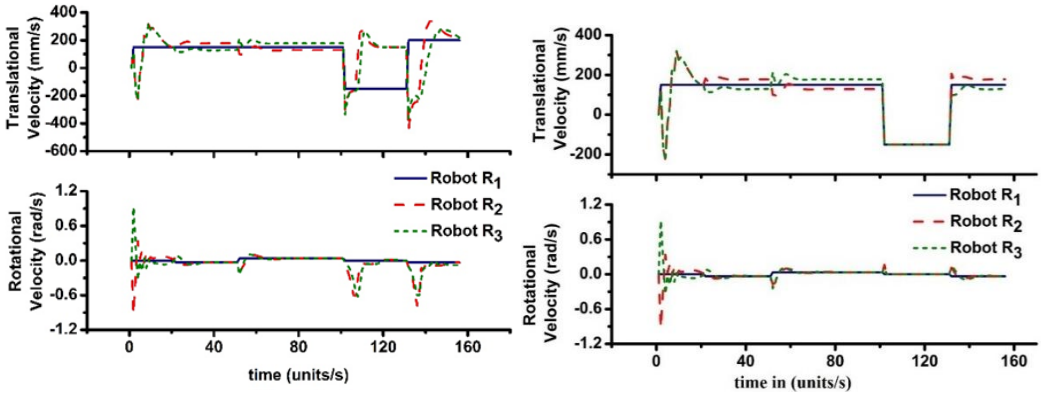

(a) **(b)**

Fig. 7. (a) Velocity profiles of robots in collateral formation exhibiting uncontrolled velocities using a tracking controller; (b) Velocity profiles of robots in collateral formation exhibiting controlled velocities between the robots using the proposed controller during backward motion

The velocity profiles of the robots are illustrated in Figure 7. It is also observed from Figure 7 (a) that the generalized tracking controller, lacks to keep the rotational velocity in the constrained limit as the sudden change in the direction of motion causes a step-change in the input and increases the tracking error. However, the proposed geometric controller keeps the robot in the tightly coupled formation where it estimates the rotational velocity by the ICC/ICR relationship given in equation (7) and by mimicking the leader's translational velocity.

Further simulations have been carried out by keeping the robots in various geometric formation topologies such as inline and collateral, and it is found out that the proposed geometric controller guides the robot in the defined geometric pattern in the backward motion with the linear, angular, and orientation errors less than ±2%, ±0.8%, and ±1.3% respectively.

6. CONCLUSION AND FUTURE SCOPE

In this work, a switching control strategy in a behavior-based approach where the behavior or motion states of the robots are switched to achieve the task of driving the robots in the backward motion with the tightly coupled formation is addressed. A generalized closed-loop tracking controller considering the leader referenced model is used for the robots to remain in the formation while navigating the environments. A simple geometric controller using the Instantaneous Centre of Radius (ICR) is developed to drive the robot in the backward motion during the deadlock situated is developed and presented. State-Based Modelling is used to model the behaviors/motion states of the proposed approach in MATLAB/STATEFLOW environment. Simulation studies are carried out to test the performance and error dynamics of the proposed approach combining the formation, navigation, and backward motion of the robots in all geometric patterns of formation. The simulation results show that the proposed closed-loop controller based on geometric approach efficiently drives the robots in the backward motion with stable formation without perturbing the formation of the robots, with the linear, angular, and orientation errors less than ±2%, ±0.8%, and ±1.3% respectively, during the fly. It is also planned to conduct experiments virtually in Webots virtual simulation environment and in real-time using differential drive pioneer P3DX robot research platforms in an environment filled with multiple obstacles.

REFERENCES

Alonso-Mora, J., Baker, S., & Rus, D. (2017). Multi-robot formation control and object transport in dynamic environments via constrained optimization. *The International Journal of Robotics Research*, *36*(9), 1000–1021. http://doi.org/10.1177/0278364917719333

Arkin, R.C. (1998). *Behavior-Based Robotics*. MIT Press.

Barfoot, T.D., & Clark, C.M. (2004). Motion planning for Formations of Mobile Robots. *International Journal of Robotics and Autonomous Systems*, *46*, 65–78. http://doi.org/10.1016/j.robot.2003.11.004

Cheng, J., Wang, B., Zhang, Y., & Wang, Z. (2017). Backward Orientation Tracking Control of Mobile Robot with N Trailers. *International Journal of Control, Automation, and Systems*, *15*, 867–874. http://doi.org/10.1007/s12555-015-0382-7

Chung, W., Park, M., Yoo, K., Roh, J., and Choi, J. (2011). Backward-motion control of a mobile robot with n passive off-hooked trailers. *Journal of Mechanical Science and Technology*, *25*(11), 2895–2905. http://doi.org/10.1007/s12206-011-0909-7

Dougherty, R., Ochoa, V., Randles, Z., & Kitts, C. (2004). A Behavioral Control approach to formation keeping through an obstacles field. In *Proceedings of the IEEE Aerospace Conference* (pp. 168–175, vol. 1). IEEE. http://doi.org/10.1109/AERO.2004.1367602

Kuppan Chetty, R.M., Nagarajan, T., Karsiti, N.B., & Singaperumal, M. (2012). State Based Modelling and Control of a Multi Robot Systems Using Simulink/Stateflow. *Journal of Applied Sciences*, *12*(24), 2494–2502. http://doi.org/jas.2012.2494.2502

Kuppan Chetty, R.M., Singaperumal, M., & Nagarajan, T. (2011a). Behavior Based Multi Robot Formations with Active Obstacle Avoidance Based on Switching Control Strategy. *Journal of Advanced Materials Research*, *443-440*, 6630–6635. http://doi.org/10.4028/www.scientific.net/AMR.433-440.6630

Kuppan Chetty, R.M., Singaperumal, M., & Nagarajan, T. (2011b). Distributed Formation planning and Navigation framework of Wheeled Mobile Robots. *Journal of Applied Sciences*, *11*(9), 1501–1509. http://doi.org/10.3923/jas.2011.1501.1509

Kuppan Chetty, R.M., Singaperumal, M., Nagarajan, T., & Inamura, T. (2011). Coordination Control of Wheeled Mobile Robots – A Hybrid Approach. *International Journal of Computer Applications in Technology*, *41*(3/4), 195–204. http://doi.org/10.1504/IJCAT.2011.042695

Lee, G., & Chwa, D. (2018). Decentralized behavior-based formation control of multiple robots considering obstacle avoidance. *Intelligent Service Robotics*, *11*, 127–138. http://doi.org/10.1007/s11370-017-0240-y

Li, X., & Xiao, J. (2005). Robot formation control in Leader-Follower Motion Using Direct Lyapunov Method. *International Journal of Intelligent Control and Systems*, *10*(2), 244–259.

Ma, Y., Zhang, Y., Cheng, J., & Zhao, Q.J. (2014). Backward Path Tracking of Mobile Robot with Two Trailers. *Applied Mechanics and Materials*, *716-717*, 1512-1517. http://doi.org/10.4028/www.scientific.net/AMM.716-717.1512

Mataric, M.J., & Michaud, F. (2008). Behavior Based Systems. In B. Siciliano & O. Khatib (Eds.), *Handbook of Robotics* (pp. 891–909). Springer.

Petrov, P. (2010) Nonlinear Backward Tracking Control of an Articulated Mobile Robot with Off axle hitching. In *Proceedings of the 9th WSEAS International Conference on Recent Advances in Signal Processing, Robotics and Automation* (pp. 269–273). The ACM Digital Library.

Petukhov, S.V., & Rachkov, M.Y. (2009). Navigation Method of Autonomous Robot Backward Motion by Remembered Landmarks. *Mobile Robotics*, 19–25. https://doi.org/10.1142/9789814291279_0005

Soni, A., & Hu, H. (2018). Formation Control for a Fleet of Autonomous Ground Vehicles: A Survey. *Robotics*, *7*(4), 67. http://doi.org/10.3390/robotics7040067

Wang, Q., & Phillips, C. (2014). Cooperative Path Planning for Multi-Vehicle Systems. *Electronics*, *3*, 636–660. http://doi.org/10.3390/electronics3040636

Werger, B.B., & Mataric, M.J. (2001). From insect to internet: situated control for Networked Robot Teams. *Annals of Mathematics and Artificial Intelligence*, *31*, 173–197. http://doi.org/10.1023/A:1016650101473

Xu, D., Zhang, X., Zhu, Z., Chen, C., & Yang, P. (2014). Behavior-Based Formation Control of Swarm Robots. *Mathematical Problems in Engineering*, *2014*, 205759. http://doi.org/10.1155/2014/205759

Applied Computer Science, vol. 17, no. 3, pp. 73–81
doi: 10.23743/acs-2021-22

Submitted: 2021-06-13 | Revised: 2021-09-08 | Accepted: 2021-09-21

RGB-D, Kinect, Local Binary Pattern, Pattern Recognition, Feature Extraction, Histogram, Face Recognition

Sunil Kumar B L [0000-0002-7406-036X]*, *Sharmila Kumari M* [0000-0002-0707-0891]**

RGB-D FACE RECOGNITION USING LBP-DCT ALGORITHM

Abstract

Face recognition is one of the applications in image processing that recognizes or checks an individual's identity. 2D images are used to identify the face, but the problem is that this kind of image is very sensitive to changes in lighting and various angles of view. The images captured by 3D camera and stereo camera can also be used for recognition, but fairly long processing times is needed. RGB-D images that Kinect produces are used as a new alternative approach to 3D images. Such cameras cost less and can be used in any situation and any environment. This paper shows the face recognition algorithms' performance using RGB-D images. These algorithms calculate the descriptor which uses RGB and Depth map faces based on local binary pattern. Those images are also tested for the fusion of LBP and DCT methods. The fusion of LBP and DCT approach produces a recognition rate of 97.5% during the experiment.

1. INTRODUCTION

For the authentication of the individuals, biometric verification using signature, iris, retina, fingerprints, voice and face is being used. Face recognition is considered amongst these techniques as one of the most popular, collectable and easily accessible systems. The method of biometric identification consists of collecting the biometric data of the individual and matching it with biometric data of the specific person. Some of the problems involved in this process are changes in posture and illumination, facial background etc. Recognition of the human face extracts features from the face and compares them with all facial images stored in the database. Local binary pattern (LBP) extraction technique can be used for clustering, classification, and segmentation of features. Using LBP and other extended methods, the texture classification (Song et al., 2015; Yu et al., 2014) is achieved which involves easy calculation and also produce good results. RGBD is the image obtained with the help of Kinect are the combination of red, green, blue color information and the depth information (Abebe & Hwang, 2019). These red green blue color uses 8-bit representation and depth uses 16-bits. To reduce the space 16-bit is transformed into 11-bits. Depth is measured in terms of millimeters and the value ranges from "1" to "10.000". RGB along with the depth can be used to get the improved results in digital image processing.

* Canara Engineering College, India, blsuny@gmail.com
** PA College of Engineering, India, sharmilabp@gmail.com

These images can be obtained with the low price Kinect camera. These images are used in 3D image reconstruction, Augmented Reality, Robotics, Pattern Recognition and Image Processing.

2. RELATED WORK

The RGBD datasets by Microsoft Kinect have motivated improvements in the areas from reconstruction to gesture recognition. Extracting relevant information helps to obtain proper data for the needs. In recent years, there has been increased focus on usage of RGB-D cameras for development of 3D scene understanding and object detection algorithms (Lin, Fidler & Urtasun, 2013). Kinect sensor based surveillance systems have also been deployed for border control (Chowdhury & Vatsa, 2016). Usage of Kinect sensors for indoor surveillance systems is an interesting research problem due to its capability of capturing RGB, Depth and NIR footage from a single camera unit. Face is highly analyzed biometric (Zhao et al., 2003) and face recognition gives better performance on 3D images compared to 2D images in the presence of pose and illumination covariates. Additional discriminative information provided by the depth map, increases the rate of recognition (Silberman et al., 2012; Wang et al., 2012). Recently, decreased cost of depth sensors has made it feasible to use the images in different applications and has consequently led to increased curiosity in RGB-D face detection (Hg et al., 2012) and face recognition. (Han et al., 2013) introduced the RGB and Depth based images for face-recognition (Huynh, Min & Dugelay, 2012) when depth sensors are started. Because of the difficulty in managing pose and lighting on 2D face recognition, 3D face recognition approaches have been suggested. The 3D image is less sensitive to changes in lighting and therefore more useful for correcting pose variations. The downside to using facial recognition approaches based on 3D is the high cost (Goswami, Vatsa & Singh, 2013) of the conventional 3D sensors. Kinect (Cruz, Lucio & Velho, 2012) tools are the alternative to these costly scanners and are capable of collecting the depth information very precisely. The depth information shows the possibility of accurate 3D face reconstruction which is used in the recognition of faces (Hsu et al., 2014). The performance improvements can be seen using local binary pattern descriptor due to RGB and depth images (Min, Kose & Dugelay, 2014; Zohra, Rahman & Gavrilova, 2016).

2.1. LBP based face descriptors

Ojala proposed Local Binary Pattern in 1990, which uses an effective and easy method to extract the local characteristics from the given face data. The two important LBP properties are (a) Simple computational features and (b) Working for various conditions of illumination. With the support of the neighborhood, LBP feature vector calculation can be performed by first dividing the entire image into cells. Then the middle pixel of the cell is compared with the eight neighboring pixels in the clockwise or anticlockwise direction around it. If (middle pixel-value > neighbor pixel value), then return "0" otherwise "1". The resulting 8-digit binary number transforms into decimal number. The histogram is computed for the features collected.

To measure the LBP code, the cell size of 3×3 is used. Each pixel in the image is compared to its 8 neighbors and encoded to "0" or "1" based on the comparative values as shown in the figure 1.

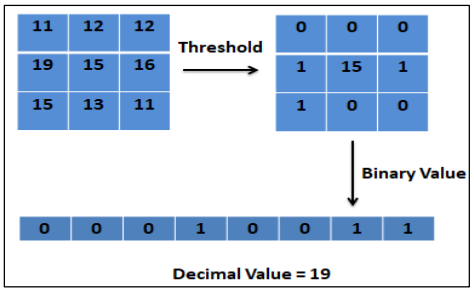

Fig. 1. LBP code calculation

Concatenate all encoded binary values in either clockwise or anticlockwise direction. This binary number consisting of 8 bits is translated to decimal number that is assigned to the cell's central pixel.

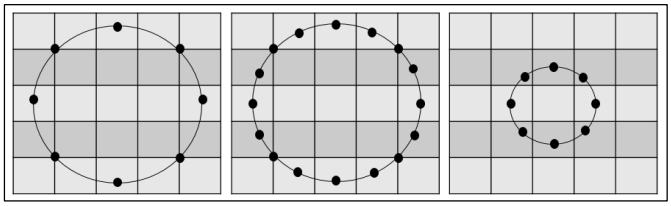

(a) r = 2 and p = 8 (b) r = 2 and p = 16 (c) r = 1 and p = 8

Fig. 2. Neighbour Pixels

The same process for the full image is continued. The cell size can be increased, and the extended LBP operator uses the notation (p, r), as shown in Figure 2, to denote a 'p' pixel neighbourhood on a 'r' radius sphere. Circular (8, 2) showing 8 neighbours for the central pixel in the circle with a radius of 2 and for circular (16, 2) showing 16 neighbours for the central pixel in the circle with a radius of 2 and also (8, 1) reveals that around the central pixel there are 8 neighbours with a radius of 1.

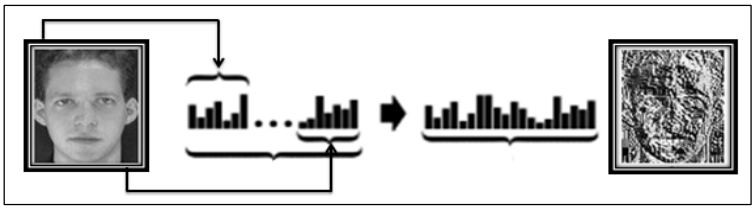

Fig. 3. Extracting feature histogram from the face image

Figure 3 demonstrates the exact workings of LBP. At first divide the window of the image into cells. Then, the histogram is determined for every cell. Concatenation of the LBP histogram obtained for each cell gives a resultant histogram feature.

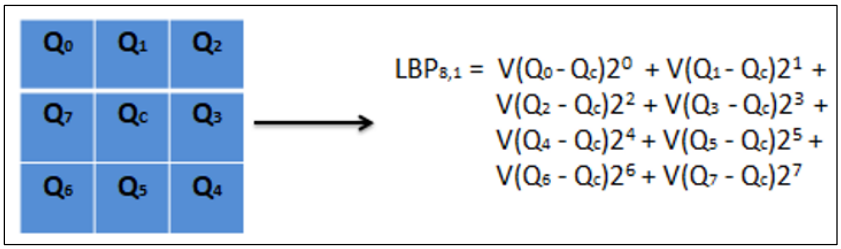

Fig. 4. LBP Calculation Code

LBP characteristics of the circular neighbours of a central pixel are indicated by LBPp,r, here p is the number of circular neighbouring points with r radius. Figure 4 shows one such calculation when p=4 and r=1. The following code is obtained in LBPp,r

$$LBP_{p,r} = \sum_{Q=0}^{Q-1} V(Q_i - Q_c)\, 2^i \,, V(x) = \begin{cases} 1 \; if \; x \geq 0 \\ 0 \; otherwise \end{cases} \tag{1}$$

Where Q_c gives the central pixel grey-level value, and Q_i is the value of the surrounding pixel in the circular neighbour. To reduce the number of bins, the idea of uniform pattern is used. It is possible to distinguish uniform patterns if there are at most two transitions from "1" to "0" or "0" to "1". Consider pattern 1111111111 with no transition or pattern 00110000 with two transitions as examples of a uniform transition, whereas pattern 10101011 with six transitions is not uniform. This restriction reduces the LBP patterns automatically from 256 to 58.

2.2. DCT based face descriptors

Using DCT, Invertible linear transforms image into feature vectors with low and high frequency coefficients. 2D-DCT converts the face image into a frequency domain, and reverse processes can also be done using invert 2D-DCT (Chen & Chen, 2010; Shermina 2011). The 2D-DCT on an image of dimension r x c:

$$\mathrm{F(u,v)} = \alpha(u)\alpha(v) \sum_{i=0}^{r-1} \sum_{j=0}^{c-1} f(i,j) \cos\left[\frac{u(2i+1)\pi}{2r}\right] \cos\left[\frac{\mathrm{v(2j+1)\pi}}{\mathrm{2c}}\right] \tag{2}$$

$$\text{where, } \alpha(u) = \sqrt{\frac{1}{r}} \text{ for u} = 0 \tag{3}$$

$$\alpha(u) = \sqrt{\frac{2}{r}} \text{ for u} = 1 \text{ to r} - 1 \tag{4}$$

$$\text{and } \alpha(v) = \sqrt{\frac{1}{c}} \text{ for v} = 0 \tag{5}$$

$$\alpha(v) = \sqrt{\frac{2}{c}} \text{ for v} = 1 \text{ to c} - 1 \tag{6}$$

The important few, low frequency DCT components of the training and testing images are extracted. Then the more relevant extracted information also called the feature vectors of training and testing images are compared. The Euclidean distance measure is used for the classification.

3. PROPOSED METHOD

Face recognition algorithm uses 2D or 3D input images for the recognition. Usually, 3D faces are used to create advanced algorithms to improve the performance, but these images are difficult to get because of the cost. This paper uses RGB-D images alternate to 3D images to implement certain face recognition algorithms.

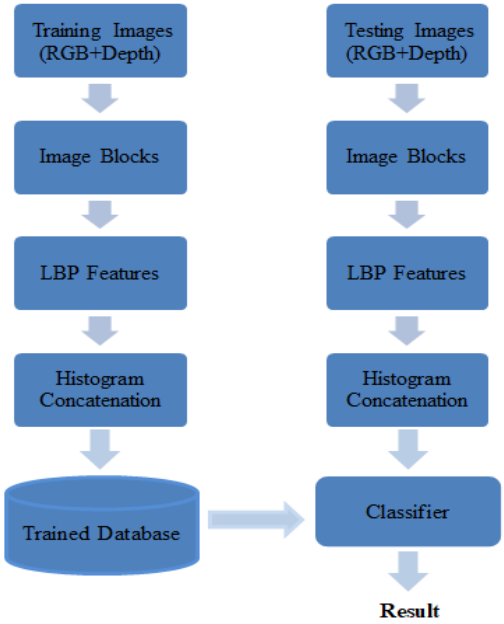

Fig. 5. Block diagram of face recognition using LBP

Local binary pattern is an extremely effective method to describing a digital image's texture, and it was ideal for obtaining features for face recognition systems as shown in Figure 5. First of all, split the image for extracting the LBP histograms and then stored in a vector. This vector represents the features of face and can be used for further processing. Much of the current face recognition work using RGB-D has focused on controlled environments. But in a real-world environment, the sensors can also capture images from a distance. The accuracy of the depth images is strong when the images are taken at close ranges. Yet, with the camera's large distance to the actual face, depth sensors struggle to capture images of good quality depth. It may not be desirable to use poor-quality pictures in these circumstances. So, the proposed approach uses both RGB and depth images for the better recognition of faces.

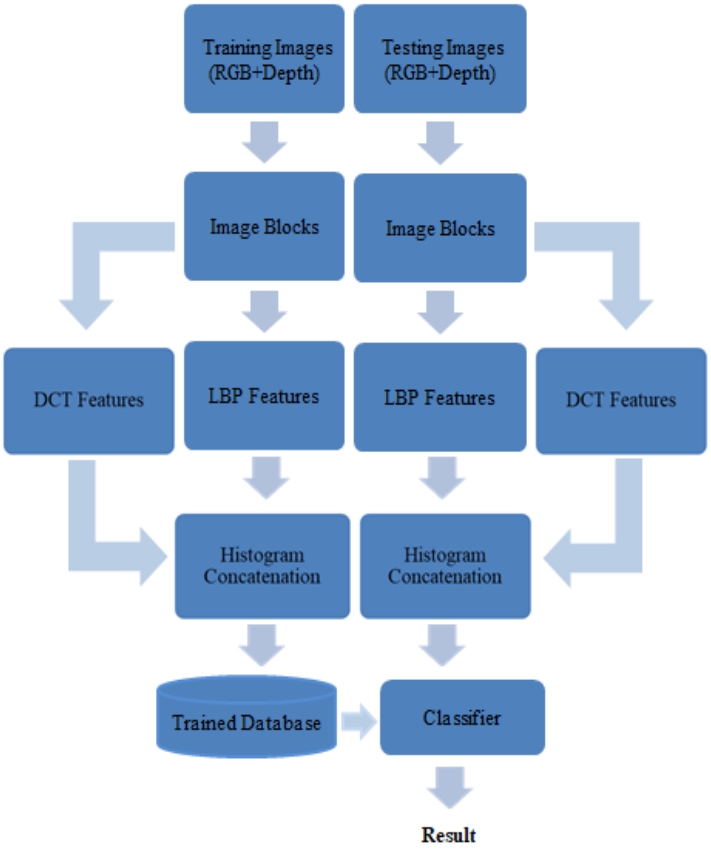

Fig. 6. Block diagram of face recognition using LBP and DCT

The proposed algorithm calculates an LBP descriptor and DCT features for the RGB images as well as for the depth images. The combined histograms are computed based on the collected features from LBP and DCT. The steps as shown in Figure 6 is repeated for all the training datasets. Finally, features of testing data are extracted and compared with all the features of the trained data set to recognize the image. The series of experiments were performed using the combined effect of features LBP and DCT. To compare and recognize the images, Euclidian distance is used in this experiment.

4. RESULTS AND DISCUSSIONS

The above methods are tested on IIITD RGB-D face images. This data-set consists of 106 subjects captured using the sensor version 1 of Microsoft Kinect. It has a large number of photos, ranging from 254 to 11 pictures per subject, per fold. The RGB and the depth images are recorded separately as 24-bit images. For these images the 640×480 resolution is used.

Fig. 7. Sample RGB-D images of a person from IIITD RGBD face dataset

The face recognition algorithms are executed by changing the count of training samples for each subject. For all such cases, the accuracy of recognition is noted as shown in the table 1 and Figure 8 shows the results on RGB-D face image data collection using conventional LBP and LBP+DCT algorithms.

Tab. 1. Recognition rate using LBP and LBP+DCTmethods

	Recognition Rate (%) (LBP)			Recognition Rate (%) (LBP+DCT)		
	RGB	Depth	RGB+ Depth	RGB	Depth	RGB+ Depth
1	85.0	75.0	92.5	85.0	82.5	92.5
2	87.5	80.5	95.0	87.5	80.5	95.0
3	90.0	77.5	92.5	90.0	82.5	95.0
4	92.5	77.5	95.0	95.5	90.0	97.5
5	92.5	75.0	95.0	95.5	90.0	97.5
6	87.5	60.0	87.5	90.0	67.5	95.0

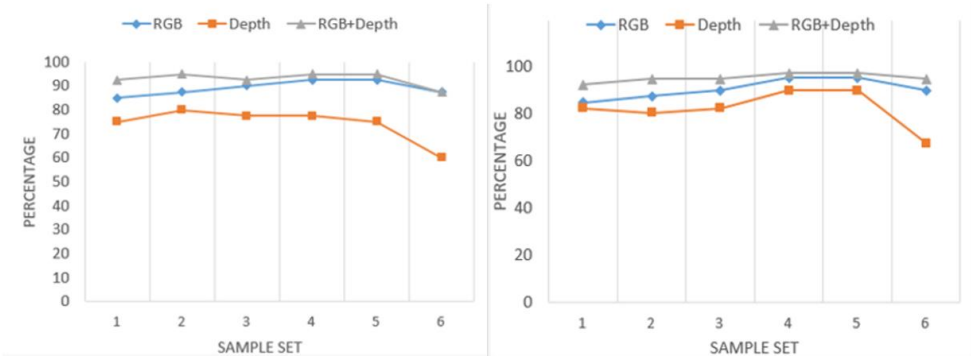

Fig. 8. Results of LBP and LBP+DCT on RGB, Depth and RGBD images

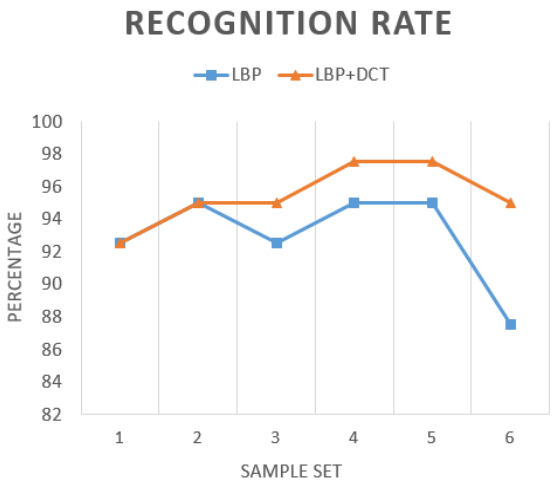

Fig. 9. Comparison of LBP and LBP+DCT

Figure 9 clearly shows combining LBP and DCT algorithms gives better result than only LBP.

5. CONCLUSION

Algorithms for face recognition generally use features of 2D or 3D images. This paper compares the effect of algorithms for extraction of features such as LBP and the fusion of LBP+DCT using both RGB and depth images. IIT-D RGB-D face image set is used for the analysis of above algorithms. For these images proposed algorithm shows 97.5% of recognition. As a future work different combinations of the feature extracting algorithms can be used on RGB-D dataset.

REFERENCES

Abebe, H. B., & Hwang, C. L. (2019). RGB-D face recognition using LBP with suitable feature dimension of depth image. *IET Cyber-Physical Systems: Theory & Applications*, *4*(3), 189–197. https://doi.org/10.1049/iet-cps.2018.5045

Chen, P. Z., & Chen, S. L. (2010). *A new face recognition algorithm based on dct and lbp. In Quantitative Logic and Soft Computing 2010* (pp. 811–818). Springer. https://doi.org/10.1007/978-3-642-15660-1_82

Chowdhury, A., & Vatsa, M. (2016). *RGB-D face recognition in surveillance videos* (Doctoral dissertation). Retrieved from https://repository.iiitd.edu.in/jspui/handle/123456789/440

Cruz, L., Lucio, D., & Velho, L. (2012). Kinect and rgbd images: Challenges and applications. In *2012 25th SIBGRAPI conference on graphics, patterns and images tutorials* (pp. 36–49). IEEE. https://doi.org/10.1109/SIBGRAPI-T.2012.13

Goswami, G., Vatsa, M., & Singh, R. (2014). RGB-D face recognition with texture and attribute features. *IEEE Transactions on Information Forensics and Security*, *9*(10), 1629–1640. https://doi.org/10.1109/TIFS.2014.2343913

Han, J., Shao, L., Xu, D., & Shotton, J. (2013). Enhanced computer vision with microsoft kinect sensor: A review. *IEEE transactions on cybernetics*, *43*(5), 1318–1334. https://doi.org/10.1109/TCYB.2013.2265378

Hg, R. I., Jasek, P., Rofidal, C., Nasrollahi, K., Moeslund, T. B., & Tranchet, G. (2012). An rgb-d database using microsoft's kinect for windows for face detection. In *2012 Eighth International Conference on Signal Image Technology and Internet Based Systems* (pp. 42–46). IEEE. https://doi.org/10.1109/SITIS.2012.17

Hsu, G. S. J., Liu, Y. L., Peng, H. C., & Wu, P. X. (2014). RGB-D-based face reconstruction and recognition. *IEEE Transactions on Information Forensics and Security, 9*(12), 2110–2118. https://doi.org/10.1109/TIFS.2014.2361028

Huynh, T., Min, R., & Dugelay, J. L. (2012). An efficient LBP-based descriptor for facial depth images applied to gender recognition using RGB-D face data. In *Asian Conference on Computer Vision* (pp. 133–145). Springer. https://doi.org/10.1007/978-3-642-37410-4_12

Lin, D., Fidler, S., & Urtasun, R. (2013). Holistic scene understanding for 3d object detection with rgbd cameras. In *Proceedings of the IEEE international conference on computer vision* (pp. 1417–1424). IEEE. https://doi.org/10.1109/ICCV.2013.179

Min, R., Kose, N., & Dugelay, J. L. (2014). Kinectfacedb: A kinect database for face recognition. *IEEE Transactions on Systems, Man, and Cybernetics: Systems, 44*(11), 1534–1548. https://doi.org/10.1109/TSMC.2014.2331215

Shermina, J. (2011). Illumination invariant face recognition using discrete cosine transform and principal component analysis. In *2011 International Conference on Emerging Trends in Electrical and Computer Technology* (pp. 826–830). IEEE. https://doi.org/10.1109/ICETECT.2011.5760233

Silberman, N., Hoiem, D., Kohli, P., & Fergus, R. (2012). Indoor segmentation and support inference from rgbd images. In *European conference on computer vision* (pp. 746-760). Springer. https://doi.org/10.1007/978-3-642-33715-4_54

Song, K., Yan, Y., Zhao, Y., & Liu, C. (2015). Adjacent evaluation of local binary pattern for texture classification. *Journal of Visual Communication and Image Representation, 33*, 323–339. https://doi.org/10.1016/j.jvcir.2015.09.016

Wang, J., Liu, Z., Chorowski, J., Chen, Z., & Wu, Y. (2012). Robust 3d action recognition with random occupancy patterns. In *European Conference on Computer Vision* (pp. 872–885). Springer. https://dl.acm.org/doi/10.5555/2964398.2964463

Yu, W., Gan, L., Yang, S., Ding, Y., Jiang, P., Wang, J., & Li, S. (2014). An improved LBP algorithm for texture and face classification. *Signal, Image and Video Processing, 8*(1), 155–161. https://doi.org/10.1007/s11760-014-0652-5

Zhao, W., Chellappa, R., Phillips, P. J., & Rosenfeld, A. (2003). Face recognition: A literature survey. *ACM computing surveys (CSUR), 35*(4), 399–458. https://doi.org/10.1145/954339.954342

Zohra, F. T., Rahman, M. W., & Gavrilova, M. (2016). Occlusion detection and localization from Kinect depth images. In *2016 International Conference on Cyberworlds (CW)* (pp. 189–196). IEEE. https://doi.org/10.1109/CW.2016.40

Applied Computer Science, vol. 17, no. 3, pp. 82–91
doi: 10.23743/acs-2021-23

Submitted: 2021-06-01 | Revised: 2021-08-16 | Accepted: 2021-09-21

frequent itemset, nodeset, FIN and IPOC

Pannangi NARESH[0000-0003-2932-6699]*, *R. SUGUNA*[0000-0002-8930-9092]*

IMPLEMENTATION OF DYNAMIC AND FAST MINING ALGORITHMS ON INCREMENTAL DATASETS TO DISCOVER QUALITATIVE RULES

Abstract

Association Rule Mining is an important field in knowledge mining that allows the rules of association needed for decision making. Frequent mining of objects presents a difficulty to huge datasets. As the dataset gets bigger and more time and burden to uncover the rules. In this paper, overhead and time-consuming overhead reduction techniques with an IPOC (Incremental Pre-ordered code) tree structure were examined. For the frequent usage of database mining items, those techniques require highly qualified data structures. FIN(Frequent itemset-Nodeset) employs a node-set, a unique and new data structure to extract frequently used Items and an IPOC tree to store frequent data progressively. Different methods have been modified to analyze and assess time and memory use in different data sets. The strategies suggested and executed shows increased performance when producing rules, using time and efficiency.

1. INTRODUCTION

The extraction procedure for information and new data formats is called knowledge mining (Agrawal, Imieliński & Swami, 1993). We may construct association rules and relationships from this derived information and itemsets that reveal some relationship and the link between items in transactions. In numerous fields like marketing, analysis and company improvement forecasts, this may be beneficial. Two qualitative metrics are needed by Association Rule (Naresh & Suguna, 2019) in general for the production of rules. Firstly, support and secondly, trust. This can enhance the procedure of mining and achieve the necessary regulations.

The FP (frequent pattern) growth method for mining was devised by Han et.al (Han et al., 2004). The first way is to develop FP-growth in depth. The tree structure has a left node and a right node; each node is associated with a transaction. About all repeated elements of a data collection, each node has a node count. This data was tree compressed, and two dataset scans were required for the mining of this technique. There was no requirement for a key candidate generation. It is substantially quicker for FP-Growth (UCI machine learning repository: Data sets, n.d.) than for other algorithms. Techniques of optimisation

* Vel Tech Rangarajan Dr. Sagunthala R&D Institute of Science and Technology, Chennai, pannanginaresh@gmail.com

are more time consuming to minimise. Zaki has suggested a first-hand depth approach such as FP to mining.

Infrequent production of items, the Apriori algorithm (Jain & Sharma, 2016) plays a vital role. This is done on each item-level by producing the candidate key. From these things created, two qualitative measures and trust will be considered to support these regulations. There are two levels in Apriori, one is joined, and the other is prune. All things are produced on a single level with the aid of the candidate key, and those things are cut to support at the pruning level.

Tab.1. Sample Transaction Databse

TID	Transactional Items
T001	{A,B,C,E}
T002	{B,C}
T003	{A,B,E}
T004	{A,C}
T005	{B,D}
T006	{A,C}
T007	{A,B}
T008	{A,C,E}
T009	{A,B,E}
T010	{A,B,C}

Minimum support level: 50% – {A},{B},{C},{A,B},{A,C}

Another type of common itemset production is the FP-growth algorithm. In the key generation, this is different from apriori. We have no candidate key in fp-growth. This works by creating a framework for an fp-tree in which each tree node is connected to an item. The graphic below explains the development of the Fp-tree from the data set (Naresh & Suguna, 2019). The data set is scanned by transaction, from which the fp-tree will be generated. The tree node link number will rise depending on the frequent order of the item if the same item is found again.

The chronological technique is applied to all essential association rule mining algorithms until the dataset amount is minimal. Their efficacy begins to decline with the number of data sets. Similar methods have therefore been devised to handle big datasets. Increasingly complex is the mining of the frequent items in a vast dataset (Chen, Zhao & Liu, 2020). Such problems have now been enhanced a day as enormous data sets and enormous volume databases are dealt with (Naresh & Suguna, 2019). Moreover, it was also a major problem, where datasets contain various attribute values, lack of and noisy data.

The PPC (pre-post code) tree (Lv et al., 2017) is made up of a null-value root node and child-value for that root. Without the root node, all nodes include pre-order (Deng & Lv, 2015), post-order, name of the item, count and list of children. The item name, which is only for which the individual items belong, is the pre-order, which indicates an integer value of the children number of the specific node, and the children list keeps all children of the tree.

The technological improvement in terms of power, communication networks and storage capacity has led to unprecedented data generation in the contemporary digital era. The mining of data from such vast databases helps to draw meaningful insights. These huge datasets nevertheless offer many difficulties. These include data volume, data speed, diversity and truthfulness. It is a problem for computer scientists to represent enormous data sets into a knowledge-based system and extract relevant information. In the field of knowledge engineering, data uncertainty is also a developing issue (Naresh & Suguna, 2019).

For example, data acquired from a location-based service such as GPS or sensor network data from several monitoring systems are generally probabilistic. The relevant information cannot be accurately retrieved for an educated conclusion using such data sets. In the finding of information from these probabilistic data sets, there is always uncertainty. Few new data mining methods (Qu et al., 2020) to overcome this problem have been introduced. The existing databases are nonetheless huge; so, new strategies must be deployed further to organise the data so that cost may be minimised.

2. BACKGROUND SURVEY

Transactional databases are distinct. The additional information offered on each transaction is different. A simple or conventional transactional database is merely a list of transactions with no further details in each transaction. In the database, temporary databases contained supplementary lifespan information. In this instance, transactions may be invalid beyond the end of their lifespan while new transactions are being put in incremental chunks (Abdelhamid et al., 2017) in the database with a fresh lifespan. Many techniques have been developed in general or total time databases to cope with the time association rules (TARs) mining process.

FP-Growt (Maw, 2020) and the so-called frequency pattern tree have been suggested with a scalable data structure (Hong et al., 2008). The advantages of employing them include not requiring candidate items and scanning the database twice so that FD-Growth is much more accurate than Apriori. The negative is that a wide range of body trees have to be constructed and take a great deal of RAM and engine time. The Apriori and FP-Growth approach for maintaining (Han et al., 2004) and controlling persistent databases are also useful. All this can not extend to a dynamic repository and may involve combining operational details over a period and the influence of pre-association rules and entirely new regulations.

To recreate the previous rules and identify new rules, the complete changed database has to be rescanned. However, this technique is time and money wasteful. The rules found in a database represent only the actual database status. However, Association rules found in the old database may no longer be valid and interesting rules for the upgraded databank in a dynamic database (Dhanaseelan & Sutha, 2016; Abdelhamid et al., 2017), where new transactions are often entered. Thus, new business information cannot be found, such as changing client preferences or new seasonal patterns.

In order to establish an intelligent environment that can detect new business data in a dynamic database (Dhanaseelan & Sutha, 2016), the algorithms of the association rules should be able to extract a dynamic database (Pavitra Bai & Ravi Kumar, 2016) gradually.

In order to resolve the problem, the larger database (Agrawal, Imieliński & Swami, 1993) may also be split into several smaller databases. Then, additional knowledge may be obtained in the incremental database without having to review the full repository. This methodology reduces the utilisation of devices and consumes less work to decode association rules from a small, incremental database than a huge dataset.

Several incremental updating strategies for the mining association rules have been developed for dynamic datasets (Hong et al., 2008). Cheung et al. described the FUP method as one of the earlier works for incremental association rule mining. FUP algorithm is the first incremental maintenance association update technology to insert new data into the database. FUP calculates frequent itemsets utilising big itemsets identified in the previous iteration based on the framework of the Apriori method. The main notion of FUP is the reuse with the incremental database (Song & Rong, 2018) of frequently produced items from prior mining. FUP's primary achievement is to cut the number of candidates set in update process.

The FUP extension algorithm (Chen, Zhao & Liu, 2020) is FUP2 which will be erased from a database to handle all the updates when a database has been added. In recent years, three types of data structure have been subsequently presented: Node-list (Deng, Wang & Jiang, 2012; Deng & Lv, 2015), N-list and Nodeset, for improving the efficiency of frequent mining elements. All of them are based on node sets from an encoded node tree. Pre-order number and post-order number are used to encode each node in the pre-order tree used by the node list and the N-list. The main distinction between nodes and N-lists is that nodes employ descendant nodes to represent a group of objects, whereas N-lists (Deng, Wang & Jiang, 2012) are an ancestral item. Two methods, dubbed PPV and PrePost, are presented for mining common items respectively based on the node-list (Deng, Wang & Jiang, 2012) and the N-list and prove to be highly successful and generally outperforming prior methods.

It is memory intensive, though, because node lists and N-lists (Deng, Wang & Jiang, 2012) must encode a node with pre-order and post-order. In addition, the Node-list and N-list encoding models cannot be used for joining N-lists (or Node-lists) of 2 short arrays to construct N-lists of a large array . We provide a data structure for mining frequently used itemsets named Nodeset. Unlike N-list, Nodeset requires the pre-order (or post-order) number of a node to encode the node without pre-order and post-order number requirements. We propose FIN to find frequent things based on the Nodeset structure.

3. PROPOSED APPROACH

New transactions can be inserted via a dynamic database. Not only may current association rules be invalidated but also new association rules be enabled. It is an important problem to maintain association rules for a dynamic database. This research thus offers a novel technique for dealing with these updates. We assume that the statistics of new transactions are progressively changing from the old transactions for the new method. According to the presumption, the old transaction data obtained through prior mining may estimate the new transaction data. Thus, after inserting new transactions into an original database that contains old transactions, supporting counts for objects derived from prior mining may deviate somewhat from support counts.

The new technique employs a maximum of 1 item set support from prior mining to estimate rare items in an original database, which can be frequent items when new transactions in the original database are added. The support count of unusual items that are eligible for frequent itemset, with maximum support number and size of new transactions that enable inserting to an original database

Tab. 2. Transaction database with ordered items of min_sup 2

Transaction ID	Items	Ordered Items
T200	**I1, I6, I7**	**I1, I6**
T201	**I1, I2, I3, I5**	**I2, I3, I5, I1**
T202	**I2, I3, I5, I9**	**I2, I3, I5**
T203	**I2, I3, I5, I8**	**I2, I3, I5,**
T204	**I2, I3, I4, I5, I6**	**I2, I3, I5, I6**

This table contains transaction ids, transaction items and arranged items by min support (2). I4, I7, I8 and I9 are deleted since their support is lower than min support. A POC tree will be generated with the rest of the items. Then create a POC tree for data D in the next step.

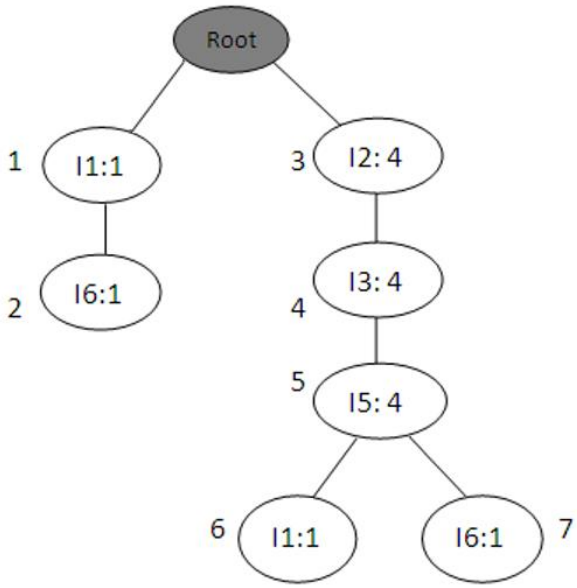

Fig. 1. POC Tree

FIN is a mining method used in transaction databases to locate frequent items. It depends on a new data structure called Nodeset that maintains frequent item information. FIN has three levels. Three levels. A POC-Tree has been established at the first level; frequency 1 itemsets are being mined, 2-item scanned in a second-level POC tree and 3 or more often used items at the final level.

Tab. 3. Ordered items of original (D) and new transaction database (d1)

	Transaction ID	Items	Ordered Items
D	T200	I1, I6, I7	I1, I6, I7
	T201	I2, I3, I5	I2, I3, I5
	T202	I2, I3, I5, I9	I2, I3, I5
	T203	I2, I3, I5, I8	I2, I3, I5, I8
	T204	I2, I3, I4, I5, I6	I2, I3, I5, I6
Incremental data – d1	T205	I1, I6, I7, I8	I1, I6, I8, I7
	T206	I1, I2, I3, I8	I2, I3, I1, I8
	T207	I1	I1

Some items support the min_sup criterion after adding new data set d1 to D. I7 and I8 are added to the current tree, and new frequent items comprising new data are also produced. The command of items changes in the ordered item list depending on the frequency count of each item. It is hence not necessary to me from scratch (existing data). Rather than updating the new item count in the tree structure, it is simple to mine the frequent things by looking at the count. In this tree, the IPOC structure is described.

3.1. FIN with POC and PPC

Although the node list and n list are composed of new mining structures, all PPC or POC tree nodes that demand time and space for often generated items must be encoded in these lists. A nodeset structure was developed to enhance time-space compromise in order to overcome these disadvantages. The nodeset shows that speed and performance are improved.

All frequent itemsets in the supplied dataset are generated by the FIN algorithm. Finish algorithm scans and produces the data set first, then visits each tree node and then calculates its support once it moves to the next node and follows the same way up to all nodes in the tree. It shows all the created FIs together with their support. We can produce association rules for analysis from these common objects.

POC Tree:

POC Tree algorithm works as follows:

- Build a POC tree.
- Identify 1-frequency item sets.
- Build the frequency sets according to the POC tree.
- Scan a POC tree for 2-items often.
- Mine all common dataset k-itemsets.

Each node N in the POC tree has a pair of values: one is pre-order, and the other is counting and N-info. The frequent item I nodeset is the series with every N-info about the POC tree nodes.

IPOC-tree

There are three major fields in the FP trees for each node: the name of the entity, the count and the connection to the node. The number of path components that strike the node reflects the number of operations is one integer in every node. Unlike the FP tree, each IPOC tree node contains four primary fields: object-id, initial number, scaled number, and node linkage. The first number tracks an object's counts in the database. A scaling number is supported in the scaling database by an object count. The increment count is started at 0 per node and increased when the associated entity is created from the main repository in the scaled depository during an IPOC-tree. . This feature is useful because an incremental database is shown in which several actions are added to the node item.

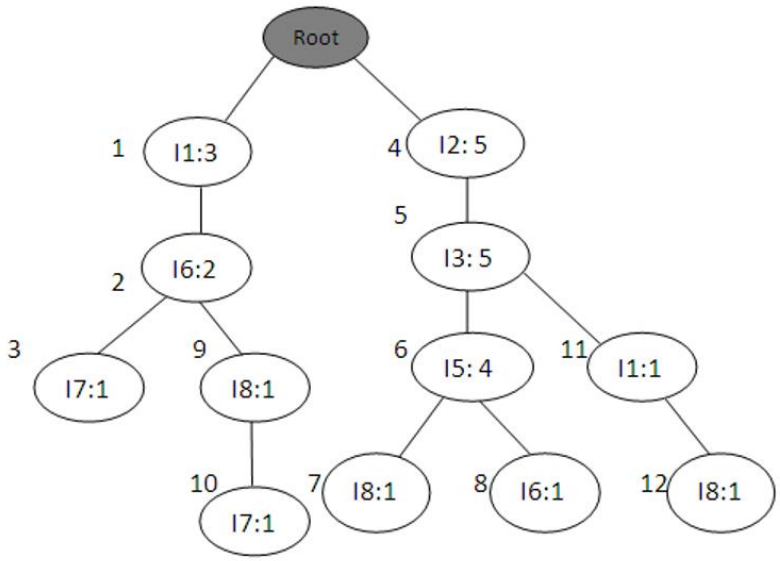

Fig. 2. IPOC tree for old data (D) and new data (d1)

4. RESULTS ANALYSIS

Datasets used: To implement the frequent items some standard datasets were needed. In this implementation Mushroom, Connect, Chess and Online Retail datasets were used. Mushroom, Connect and Chess datasets were downloaded from FIMI Repository and Online Retail Dataset was taken from UCI Machine Learning Repository (UCI machine learning repository: Data sets, n.d.).

Tab. 4. Datasets description

Dataset	No of Instances	No of Attributes	Size
Chess	3196	36	349 KB
Mushroom	8124	22	365 KB
Connect	67557	42	5829 KB
Online Retail	541909	8	23160 KB

The datasets were selected for implementing and analyzing the time and space trade offs for IPOC tree for mining qualitative association rules. The following table describes various datasets performances. Here the dataset sizes was increased dynamically to check efficiency , memory and time.

Tab. 5. Comparison analysis of time and memory for various datasets

Dataset Size/Name	IPOC-Tree							
	Chess		Mushroom		Connect		Online Retail	
	Time	Memory	Time	Memory	Time	Memory	Time	Memory
20%	0.92	12.36	2.51	25.16	7.58	78.91	17.51	180.75
40%	1.14	14.85	2.73	26.25	8.95	81.65	24.65	197.63
60%	1.42	17.87	3.01	26.38	10.87	93.85	31.86	204.36
80%	1.97	18.96	4.23	26.42	11.32	101.25	42.88	221.45
100%	2.12	21.61	4.42	26.64	13.86	109.24	50.81	239.61

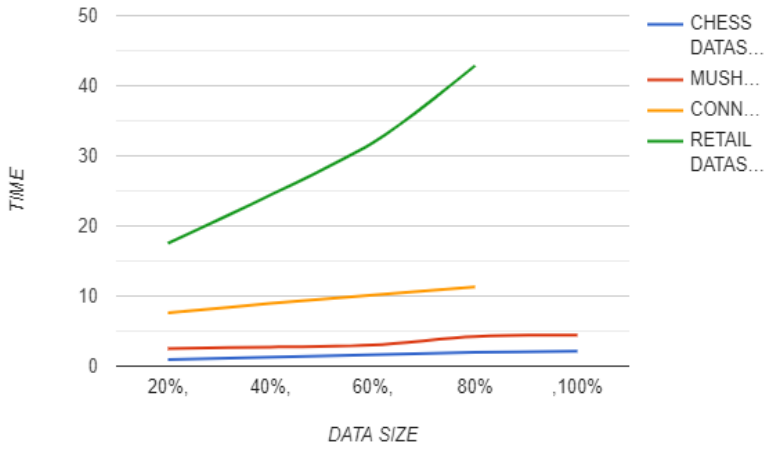

Fig. 3. Time comparisions of increasing datasets

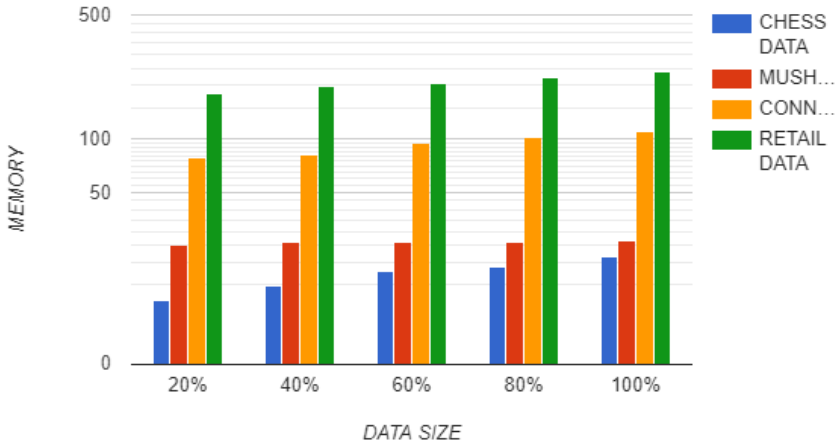

Fig. 4. Memory comparisions of increasing datasets

5. CONCLUSION

This article discusses an implementation employing a concept of FP algorithms for improved progressive association rules discovery for dynamic datasets. The fundamental notion behind the technology is to get and dynamically employ all recurring things in the initial repositories to detect all the common objects. The redesigned IPOC tree will ensure that starting pathways are avoided and that the installed substrates are minimised. The issue of incremental mining under the rule of temporary association was addressed in this work. The difficulty is to locate frequent time items in updated databases that add new transactions depending on a specified timetable. Results also demonstrated that the methodology presented uses less storage space. On the other hand, the method demonstrated linear squealing speed even at lower minsupp threshold values while mining huge datasets. The experimental results show that the proposed methodology has minimised the number of subtrees formed and the time required.

REFERENCES

Agrawal, R., Imieliński, T., & Swami, A. (1993). Mining association rules between sets of items in large databases. *Proceedings of the 1993 ACM SIGMOD international conference on Management of data – SIGMOD '93* (pp. 207–216). ACM Digital Library. https://doi.org/10.1145/170035.170072

Deng, Z., Wang, Z., & Jiang, J. (2012). A new algorithm for fast mining frequent itemsets using N-lists. *Science China Information Sciences*, *55*(9), 2008–2030. https://doi.org/10.1007/s11432-012-4638-z

Deng, Z., & Lv, S. (2015). PrePost+: An efficient N-lists-based algorithm for mining frequent itemsets via children–parent equivalence pruning. *Expert Systems with Applications*, *42*(13), 5424–5432. https://doi.org/ 10.1016/ j.eswa.2015.03.004

Hong, T.-P., Chen, H.-Y., Lin, Ch.-W., & Li, S.-T. (2008). Incrementally fast updated sequential pattern trees. *2008 International Conference on Machine Learning and Cybernetics* (pp. 3991–3996). IEEE. https://doi.org/10.1109/icmlc.2008.4621100

Lv, D., Fu, B., Sun, X., Qiu, H., Liu, X., & Zhang, Y. (2017). Efficient fast updated frequent pattern tree algorithm and its parallel implementation. *2017 2nd International Conference on Image, Vision and Computing (ICIVC)* (pp. 970-974). IEEE. https://doi.org/10.1109/icivc.2017.7984699

Naresh, P., & Suguna, R. (2019). Association rule mining algorithms on large and small datasets: A comparative study. *2019 International Conference on Intelligent Computing and Control Systems (ICCS)* (pp. 587–592). IEEE. https://doi.org/10.1109/iccs45141.2019.9065836

Pavitra Bai, S., & Ravi Kumar, G. K. (2016). Efficient incremental Itemset tree for approximate frequent Itemset mining on data stream. *2016 2nd International Conference on Applied and Theoretical Computing and Communication Technology (iCATccT)* (pp. 239–242). IEEE. https://doi.org/10.1109/icatcct.2016.7912000

Qu, J., Hang, B., Wu, Z., Wu, Z., Gu, Q., & Tang, B. (2020). Efficient mining of frequent Itemsets using only one dynamic prefix tree. *IEEE Access*, *8*, 183722-183735. https://doi.org/10.1109/access.2020.3029302

Maw, S. S. (2020). An improvement of FP-growth mining algorithm using linked list. *2020 IEEE Conference on Computer Applications (ICCA)* (pp. 1–4). IEEE. https://doi.org/10.1109/icca49400.2020.9022857

Chen, R., Zhao, S., & Liu, M. (2020). A fast approach for up-scaling frequent Itemsets. *IEEE Access*, *8*, 97141–97151. https://doi.org/10.1109/ACCESS.2020.2995719

Jain, T., & Sharma, D. V. (2016). Quantitative analysis of Apriori and eclat algorithm for association rule mining. *International Journal Of Engineering And Computer Science*, *4*(10). https://doi.org/10.18535/ijecs/v4i10.18

Dhanaseelan, F. R., & Sutha, M. J. (2016). An effective hashtable-based approach for incrementally mining closed frequent itemsets using sliding Windows. I*nternational Journal of Data Mining, Modelling and Management*, *8*(4), 382. https://doi.org/10.1504/ijdmmm.2016.10002313

Abdelhamid, E., Canim, M., Sadoghi, M., Bhattacharjee, B., Chang, Y., & Kalnis, P. (2017). Incremental frequent Subgraph mining on large evolving graphs. *IEEE Transactions on Knowledge and Data Engineering*, *29*(12), 2710–2723. https://doi.org/10.1109/tkde.2017.2743075

Song, W., & Rong, K. (2018). Mining high utility sequential patterns using maximal remaining utility. In Y. Tan, Y. Shi & Q. Tang (Eds.), *Data Mining and Big Data. DMBD 2018. Lecture Notes in Computer Science* (Vol. 10943, pp. 466–477). Springer. https://doi.org/10.1007/978-3-319-93803-5_44

Han, J., Pei, J., Yin, Y., & Mao, R. (2004). Mining frequent patterns without candidate generation: A frequent-pattern tree approach. *Data Mining and Knowledge Discovery*, *8*(1), 53–87. https://doi.org/10.1023/b:dami.0000005258.31418.83

UCI machine learning repository: Data sets. (n.d.). Retrieved April 8, 2021 from https://archive.ics.uci.edu/ml/datasets

Applied Computer Science, vol. 17, no. 3, pp. 92–105
doi: 10.23743/acs-2021-24

Submitted: 2021-08-23 | Revised: 2021-09-17 | Accepted: 2021-09-28

tensile strength, FEM, CAD modelling, stainless steel, mechanical engineering

Mateusz SAWA [0000-0002-9800-7715]*, *Mirosław SZALA* [0000-0003-1059-8854]**, *Weronika HENZLER* [0000-0002-9388-1382] *

INNOVATIVE DEVICE FOR TENSILE STRENGTH TESTING OF WELDED JOINTS: 3D MODELLING, FEM SIMULATION AND EXPERIMENTAL VALIDATION OF TEST RIG – A CASE STUDY

Abstract

This work shows a case study into 3D modelling, numerical simulations, and preliminary research of self-designed test rig dedicated for uniaxial tensile testing using pillar press. Innovative device was CAD modelled, FEM optimized, build-up according to the technological documentations. Then, the device utilization for tensile testing was validated via preliminary research. 3D model of the device was designed and FEM-analyzed using Solid Edge 2020 software. The set of FEM simulations for device components made of structural steel and stainless steel and at a workload equal 20 kN were conducted. This made it possible to optimize dimensions and selection of material used for individual parts of the device structure. Elaborated technical documentation allows for a build-up of a device prototype which was fixed into the pillar press. After that, the comparative preliminary experiments regarding tensile strength tests of X5CrNi18-10 (AISI 304) specimens were carried out. Tests were done using the commercial tensile strength machine and obtained results were compared with those received from an invented device. The ultimate tensile strength of X5CrNi18-10 steel, estimated using the commercial device (634 MPa) and results obtained from the patented device (620 MPa), were in the range of the standardized values. Findings confirm the utilization of the invented device for tensile strength testing.

1. INTRODUCTION

Tensile strength testing is the fundamental method for the evaluation of the basic mechanical properties of structural materials. Operation idea of testing machines, i.e. instruments used to state the strength of materials, is well known. The specimen of tested material shall be subjected to stresses leading to its deformation; values of forces and

* Lublin University Of Technology, Mechanical Engineering Faculty, Department of Materials Engineering, Students Research Group of Materials Technology, Nadbystrzycka 36, 20-618 Lublin, Poland, mateusz.sawa1@pollub.edu.pl, weronika.henzler@pollub.edu.pl
** Lublin University Of Technology, Mechanical Engineering Faculty, Department of Materials Engineering, Nadbystrzycka 36, 20-618 Lublin, Poland, m.szala@pollub.pl

deformation are measured. Typically, a universal testing machine (UTM) is used to investigate mainly the tensile strength and compressive strength of materials. Thus, different research papers relate to estimating the mechanical properties based on true stress analysis during tensile, likewise (Estrada et al., 2019; Kowal & Szala, 2020; Żebrowski et al., 2019) or compression (Machrowska et al., 2020; Szala et al., 2020). Moreover, the specialized testing machines allow to an investigation of the fatigue properties of materials (Branco et al., 2021; Macek, Szala, Trembacz, Branco & Costa, 2020), however then advanced equipment is required. Wide variety of metallic materials, e.g. carbon (Świć et al., 2020), structural (Caban, Nieoczym & Gardyński, 2021), high strength (Macek, Branco, Trembacz, Costa, Ferreira & Capela, 2020) steels, aluminium (Kilicaslan, Elburni & Akgul, 2021), magnesium (Zagórski et al., 2019), nickel (Sarre et al., 2016), cobalt (Szala, Chocyk, Skic, Kamiński, Macek & Turek, 2021), titanium (Rudawska et al., 2019) based alloys are employed in mechanically loaded components and structures fabrication. In addition, welded (Nowacki, Sajek & Matkowski, 2016), riveted (Lubas & Witek, 2021) or adhesive (Kłonica, 2018) joints are required to be mechanically investigated too. The available studies show that testing of mechanical properties of materials is a source of highly useful knowledge allowing the correct selection of materials or forecast the structure performance. Engineering practice requires cost-effective and easy-in-operation equipment for preliminary, in-work investigation of as-fabricated welded samples. Standard mechanical testing procedures aiming at the estimation of the metallic specimens strength properties employes complex testing systems. Moreover, specimens could be redirected to professional laboratories. An easy-in-use rig for mechanical testing of welded joins could speed up the modification of welding procedures before the final welding technology qualification. This will limit the production time and reduces the costs. Therefore, the objective of the current project was to invent the test rig for tensile testing of welded joints using simple, workhouse equipment.

Nowadays essential engineering practice is to optimize the mechanical behaviour of engineering structures using FEM (finite elements method) analysis's which is systematically employed by many research groups (Falkowicz, Ferdynus & Wysmulski, 2015; Kawecki & Podgórski, 2017; Szklarek & Gajewski, 2020). Moreover, recommended research practice is to validate the FEM results experimentally (Dziubińska et al., 2021; Jonak, Karpiński & Wójcik, 2021; Różyło, Wysmulski & Falkowicz, 2017). On the other hand, in the specific application, the in-situ mechanical tests are still essential and cannot be replaced by computer simulations. Exemplary, to evaluate the quality of welded joints especially during qualification of the welding technology (Janeczek, Tomków & Fydrych, 2021). It is known from the ISO 6892-1 standard that UTMs allow determining the complex set of mechanical properties e.g. ultimate tensile strength R_m, yield strength $Rp_{0.2}$ (set at 0.2% plastic strain), elongation used for engineering strain and stress calculations. In case of the welded specimens testing, according to the standard EN ISO 4136, the most important is to evaluate the ultimate tensile strength (R_m) deriving from the maximum load (F) and the cross-sectional area of the specimen. It seems that Rm could be easily estimated with the usage of basic engineering equipped able to measure the applied force, likewise hydraulic presses. In addition, the engineering-workhouses the hydraulic presses are much more popular than the tensile testing divides mostly because these are quite universal machines. Therefore, rather than utilizing the expensive specialized equipment, it seems justified to elaborate ergonomic, cost-effective devices for tensile testing by adapting the available equipment. Therefore there is need form the point of view of industry practice to elaborate easy-to-

operate device for tensile testing of metallic samples. This device should base on utilization popular equipment and well-available workhouse equipment likewise pillar hydraulic press. Presses have a wide applications in machine building industry, and facilite fast determination of the maximum load required to strength calculation.

Patent databases survey indicates that no devices are allowing tensile strength testing using a hydraulic press. In other words, specimen tensile via semi-compression. An exemplary patented device (Lyalin Mikhajlovich, Zykov Mikhajlovich & Sidorov Aleksandrovich, 2021) consists of a movable housing with a fixed-grip unit for fixing one end of the sample. Inside the mobile housing of the device, there is a fixed part with a second grip unit attached to secure the other end of the sample, fixed to the fixed anvil. Hitting the upper surface of the moving part, it is dynamically vertically moving downwards while breaking the sample, fixed on one side in the fixed holder and on the other side in the moving holder. This device allows the impact test to be carried out for samples using an available strength machine. Another available description of the patent application (Pezowicz et al., 2016) shows a device for biaxial stretching of biological samples. It is characterized by the use of four jaws for fixing the sample, embedded in sleds connected to the corresponding drive systems. Each jaw can move perpendicular to the direction of movement of the sleds, which allows generating the expected lengthening of the sample according to the tensile axes. It is also known for its utility model (Haizhou, 2020) testing machine for tensile strength of samples. It consists of a bracket, a screw drive system, guide rods, lifting bolts, lifting plate, top plate, two jaw assemblies, pressure sensor, notched guard, and protective cover. The device can carry out a static sample tensile test by attaching the sample to the jaws and by straining it with vertical force.

Basing on the literature and patent databases survey it can be concluded that tensile strength tests are very often carried out using specialized equipment or complex UTM systems. These rigs, contrary to the popular pillar hydraulic presses, are often inaccessible, economically problematic due to their cost-demanding maintenance.

Therefore our project aims to research the design of the device for tensile testing of metallic samples with the usage of a pillar hydraulic press. The application of CAD modelling, FEM optimization allows the design of the original device structure. The utilization of the built test rig was positively validated by preliminary investigations.

2. CAD MODELLING OF THE INVENTED DEVICE

Brief foredesign. The project aimed to create a device for static, sample tensile testing to be carried out with the use of a laboratory hydraulic press P-50 type. The tested specimen should be loaded uniaxially and the device should be easy to use. The main problem was to achieve a sample shoulder system eliminating the non-linearity which could be presented while testing the welded joint specimens. The device should allow tensile testing of metallic samples in standardized conditions described by (*ISO 6892-1: Metallic materials – Tensile testing – Part 1: Method of test at room temperature*, 2010) and (*ISO 4136:2012 Destructive tests on welds in metallic materials — Transverse tensile test*, 2012, p. 2012).

Invented device characterization. The original idea of the device was 3D modelled using Solid Edge 2020 software. The designed facility is presented with the markings of the individual parts in Fig. 1. The device consists of a housing (1) which consists of a lower base

(1.1), two side walls (1.2) perpendicular to it, a rear wall (1.3) fixed between the sidewalls (1.2) and attached to the sidewalls (1.2), and the top plate (1.4) with a through-hole (A) in the central part parallel to the bottom plate (1.1). On the top plate (1.4) with a hole (A) in the central part, a graded mounting sleeve (2) with a thrust bearing (3) attached to it, is mounted in the axis of the bore (A), in which the upper part of the upper jaw assembly (4) located in the hole (A) in the top plate where the first end of the test sample (10) is mounted. In the top plate (1.4), there are two through-holes (B) arranged symmetrically to the axis of the hole (A). In the axis of each of the two holes (B), a guide sleeve (5) facing upwards is attached and in each of the two holes (B), there is a rod (6), the upper end of which is attached to the upper movable plate (7) above the top plate (1.4). On the other hand, the lower end of each rod (6) is attached to the lower movable plate (8) inside the housing (1). A lower jaw assembly (9) is attached to the lower movable plate (8) from the bottom base side.

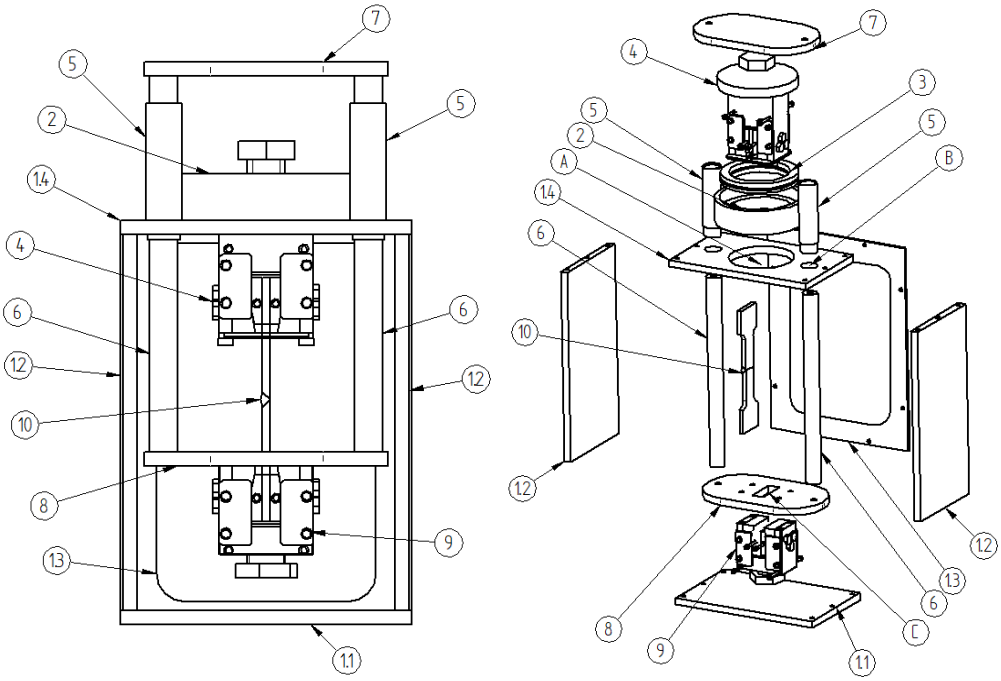

Fig. 1. Patented idea of the device (CAD) – description in the text

In the examination of the samples using a device, the sample shall be fixed in the jaw assemblies in such a way that the jaw-grabbing surface is clamped on the grip surface of the sample, which is achieved by using a screw to press the jaw gripper to the grip surface of the sample. The device with the sample fixed shall be placed on the press table and the clearance between the upper surface of the upper movable plate and the application surface of the press rod shall be eliminated. Then, through a press rod, pressure is exerted on the upper movable plate, which, by interacting with the rods, causes the lower movable plate to move, causing the sample to stretch. On the other hand, the upper part of the sample is attached to the top plate of the housing, which prevents it from moving progressively.

The main advantage of the invention is the use of a thrust bearing on which the upper assembly is mounted. The bearing, which is aligned with the geometry, compensates for the

non-linearity of the sample stretching by positioning the jaws spontaneously under the applied force. This is crucial while testing the welded joints which are prone to heat-induced deformation and other dimensional and shape-related non-uniformities. The device idea was subject is an objective of a patent application submitted to the Patent Office of the Republic of Poland (Szala, Sawa & Walczak, 2021).

3. STRUCTURE OPTIMISATION – FEM SIMULATION

The device structure was optimized using Solid Edge 2020 software. For the designed device, a static analysis of the stresses caused by the working load needed to break the sample of F=20 kN was performed. The accuracy of the calculation mesh was 3.25 mm. The set of analyses allows selection of the ideal structural material, and to minimalize the total mas and in turn, optimize the performance of the invented device.

Each of the FEM simulations allows determining the strengthened components. Then the rig was redesigned to improve the mechanical properties of the strenuous areas. Finally, the FEM analysis was repeated to validate the redesigned object. FEM results of the finally designed device are presented in Fig. 2–Fig. 5. The graphical results of the endurance simulation of the whole device with a fixed sample are shown in Fig. 2. Stress distribution of housing and movable part of the device is shown in Fig. 3. The deformation of construction is shown in Fig. 4. Even though the rig will be dedicated to testing the welded joints the isotropic sample was designed for the FEM analysis and preliminary research. The results of sample stress distribution and its dimensions are shown in Fig. 5. On the stress scale, critical stresses are determined for the device material, i.e. structural steel S355 and stainless steel X5CrNi18-10 (AISI 304), EN 1.4301 according to (*EN 10088-2:2014 – Stainless steels. Part 2: Technical delivery conditions for sheet/plate and strip for general purposes*, 2014). The same specimen's shape was manufactured for the preliminary in-situ experiments.

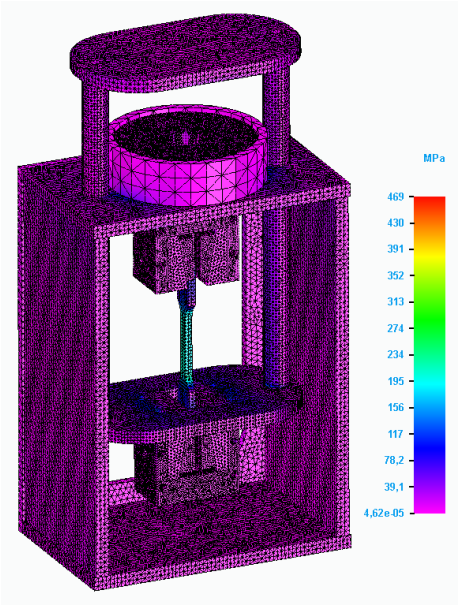

Fig. 2. Graphic results of FEM simulation of stresses estimated for a device in operation conditions

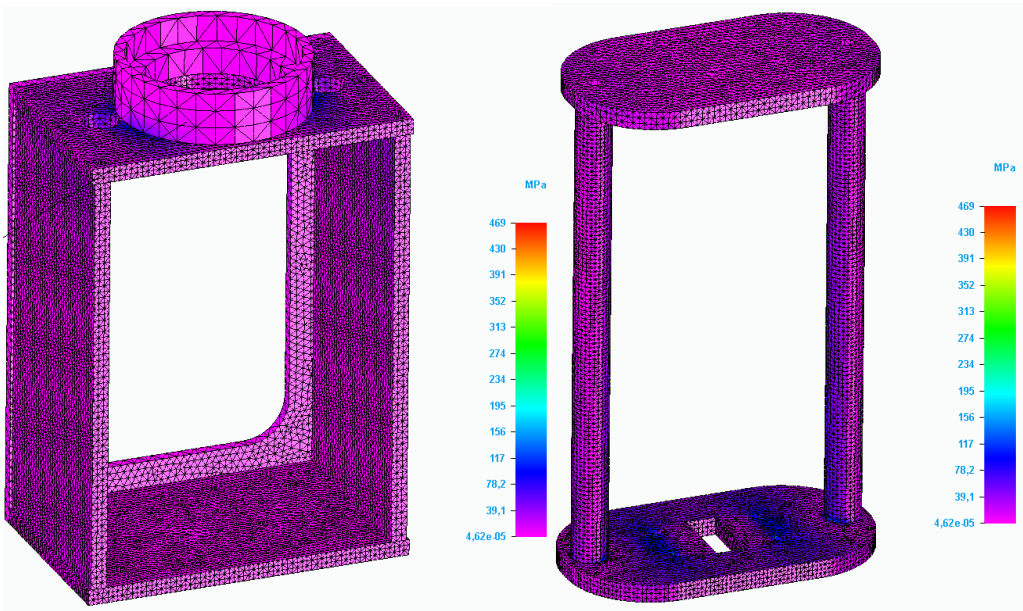

Fig. 3. From left: tension in housing and movable part – FEM

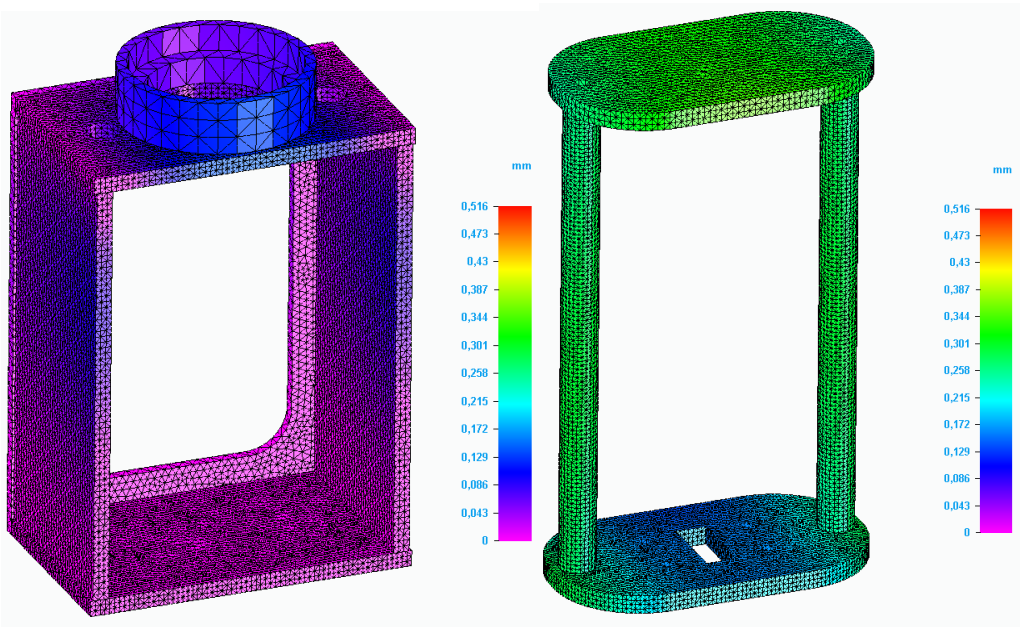

Fig. 4. Deformation of – from left: housing, movable part – FEM

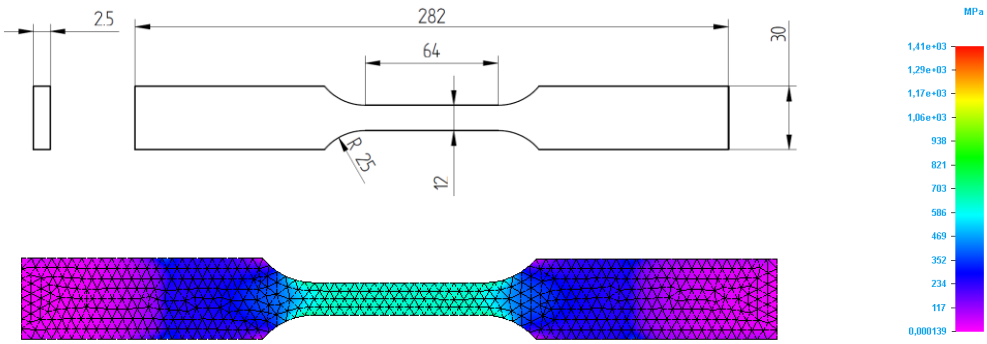

Fig. 5. The dimensions of a test sample with a square section along the gauge length and results of FEM simulation presenting stresses distribution in the specimen

4. BUILT-UP DEVICE AND VALIDATION OF INVENTION

The results of FEM analysis allow obtain the final design, select the materials and optimise dimensions of structural details described in the technological documentation. After that, the test device components were manufactured and the test rig dedicated for tensile testing was finally constructed. In addition, the device operation idea was subject to a patent application submitted to the Patent Office of the Republic of Poland (Szala, Sawa & Walczak, 2021). Finally, the designed device was manufactured, as can be seen in Fig. 6. In order to demonstrate the utility of a proposed patent and evaluate the usefulness for real-operation of the build-up test device, preliminary research was carried out.

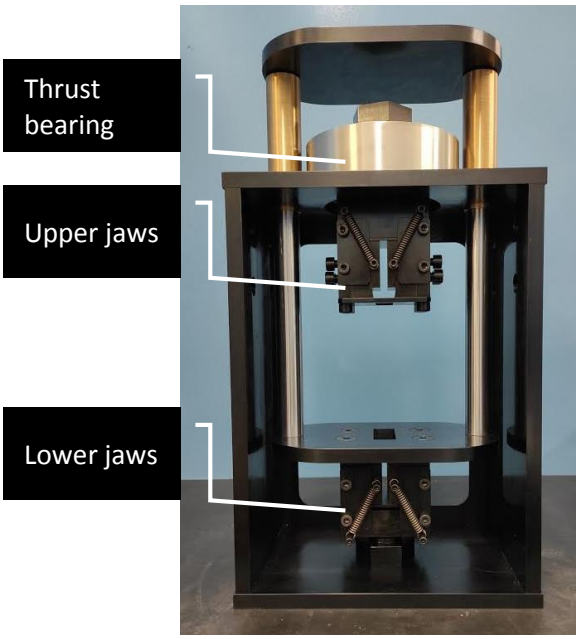

Fig. 6. Invented device for tensile testing

4.1. Preliminary research procedures and tested samples characterization

The main goal was to compare the ultimate tensile strength result obtained from the originally designed test rig, presented in Fig. 7a, and the commercial tensile machine, Fig. 7b. Even though the device is dedicated for welded joints tensile in the preliminary studies we utilized samples fabricated from a model material, namely stainless steel grade X5CrNi18-10 (AISI 304). This steel thanks to its good comprehensive mechanical properties, good ductility and weldability (Pańcikiewicz et al., 2020; Skowrońska et al., 2021; Zheng et al., 2018) is utilized in broad types of applications likewise leisure (Szala & Łukasik, 2018), engineering piping systems (Łabanowski et al., 2017), and devices operating in a corrosive environment (Ha et al., 2018) also operated under tensile loads (Hamidah, Wati & Hamdani, 2018). As shown in Fig. 8, steel microstructure consists of austenite with the visible twinning due to sheet metal forming which is in agreement with the literature (Szala et al., 2019; Zheng et al., 2018). Nominal mechanical properties of tested stainless steel are given in Tab. 1. Samples used for comparative tensile testing were water-jet cut for the 2.5 mm thick sheet metal to be strengthened along to the X5CrNi18-10 sheet metal rolling direction. The dimensions of test specimens and exemplary samples are shown in, Fig. 5. The ultimate tensile strength (UTS, R_m) of a set of identical samples was tested using the INSTRON 8801 commercial machine (a maximum available load of 100 kN) and with a hydraulic press (a maximum load of 500 kN) equipped with the constructed device, both shown in Fig. 7. The displacement and load were controlled during investigations. Therefore, UTS (estimated as maximum stress that a material can withstand while being stretched) and elongation were calculated according to ISO 6892-1 standard specification. The fractured X5CrNi18-10 steel specimens were comparatively analyzed concerning the standard mechanical properties and literature.

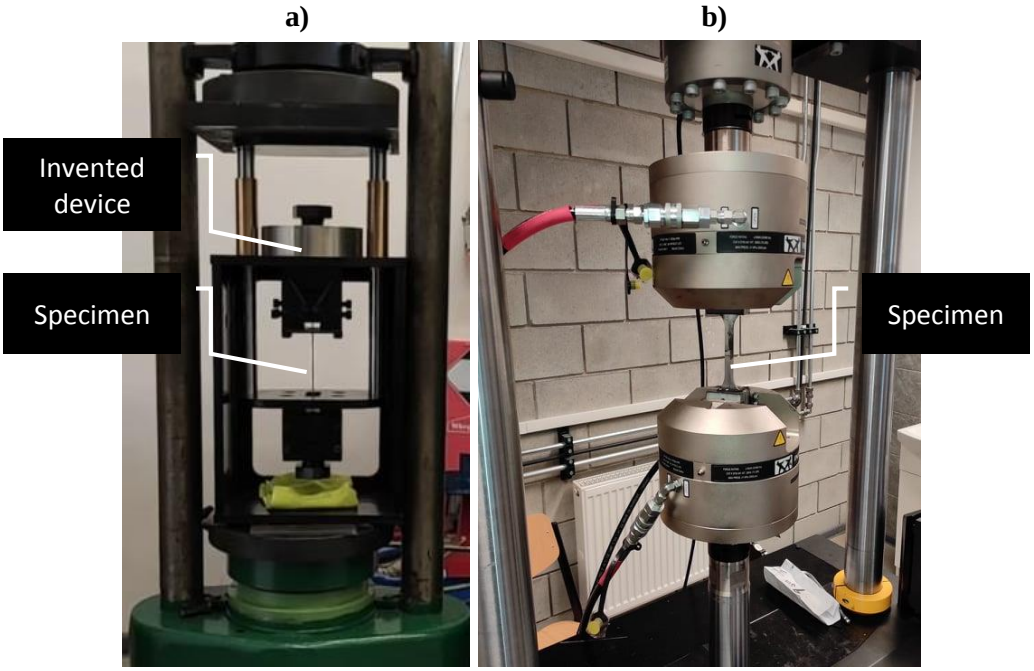

Fig. 7. Equipment used for preliminary tests: a) hydraulics press with an invented device, b) universal testing machine INSTRON 8801

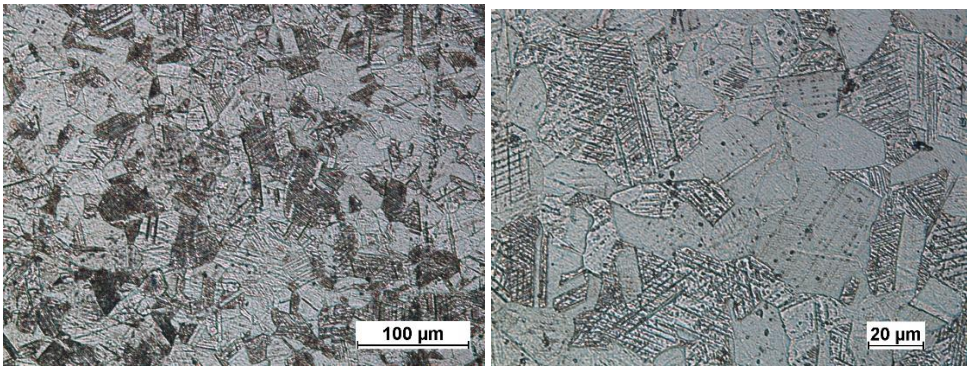

Fig. 8. Microstructure of the X5CrNi18-10 (AISI 304) stainless steel, metallographic microscope

Tab. 1. Mechanical properties of X5CrNi18-10 samples according to (*EN 10088-2:2014—Stainless steels. Part 2: Technical delivery conditions for sheet/plate and strip for general purposes*, 2014)

Ultimate tensile strength, R_m	0.2% proof strength, $R_{p0.2}$	Elongation after fracture		Vickers hardness*
		A_{80}<3 mm thick, $\%_{min}$	A≥3 mm thick, $\%_{min}$	192±12 HV0.2
540-750 MPa	230 MPa	45%	45%	

* measured according to the ISO 6507 standard

4.2. Results and analysis of the utility of the invented device

The exemplary AISI 304 tensile sample is shown in Fig. 9 while Tab. 2 and Fig. 10 present the quantitative results of the comparative tensile testing. The fracture is located in the highest stress area which agrees with the FEM simulations presented in Fig. 5. The fractographic inspection of the broken samples reveals the ductile fracture mode which is in agreement with the literature data for cold-rolled AISI 304 austenitic stainless steel (Amininejad, Jamaati & Hosseinipour, 2019). Moreover, fractured samples were characterised by relatively high elongation after fracture at the level of 50–60% (see Fig. 8), which also follows the elongation required by the standard recommendations, see Tab. 1. The literature (Nedeloni et al., 2018) reports the ultimate tensile strength (UTS) of X5CrNi18-10 at the level of R_m= 605 MPa. The comparison of maximum tensile stress and UTS indicates comparable results given for both the invented device and the professional testing machine, see Fig. 10. Results fulfil the required nominal mechanical properties of X5CrNi18-10 steel. Also, it should be pointed out that AISI 304 steel mechanical properties strongly relates to the grain size (Mahmood et al., 2021, p. 304) namely, grain refinement increases the strength and hardness. Moreover, the AISI 304 steel sheet rolling direction affects the anisotropy in tensile properties (Rout, 2020) - higher UTS value is obtained usually on the specimen tested along the rolling direction than transverse tensile.

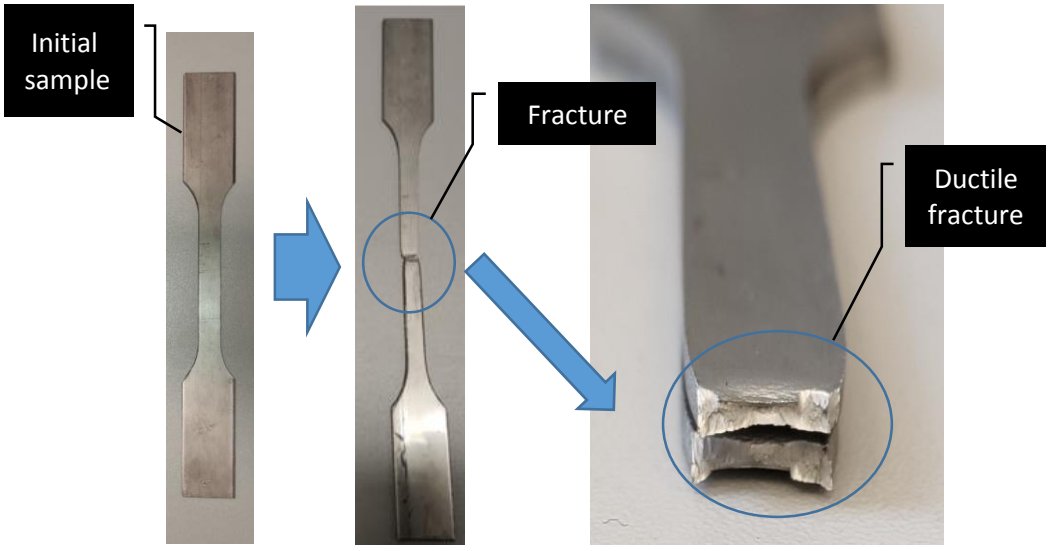

Fig. 9. AISI 304 tensile sample: fracture locations, marked ductile fracture, specimen dimensions in fig. 5

Tab. 2. Test results of X5CrNi18-10 stainless steel specimens

Type of test rig used for tensile testing	Maximum stress, F_m [N]	Ultimate tensile strength, R_m [MPa]
INSTRON 8801	19341	634
Invented device fixed in hydraulic press P-50 type	19530	620

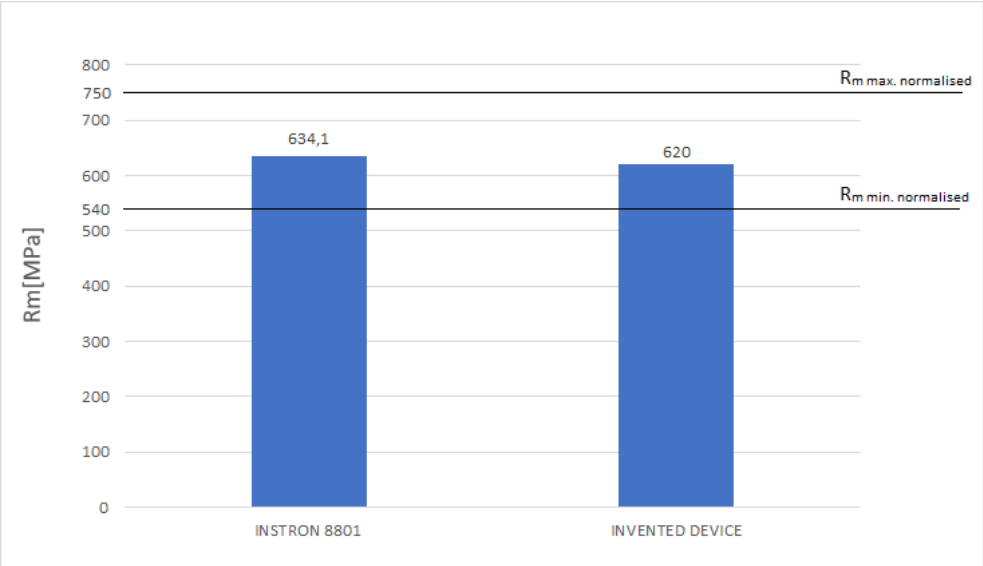

Fig. 10. Comparison of ultimate tensile strength obtained from the commercial machine, a self-made device with nominal values given for X5CrNi18-10 steel acc. to EN ISO 10088-2 standard (*EN 10088-2:2014 – Stainless steels. Part 2: Technical delivery conditions for sheet/plate and strip for general purposes*, 2014)

Findings obtained in comparative tensile testing studies, using two test rigs, confirm the utilization of the invented and constructed test device for testing the R_m of steel samples. The innovation of the device relies on the application of thrust bearing allows positioning the loaded jaws uniaxially, which is crucial in the case of welded joints testing. The R_m of model samples made of X5CrNi18-10 steel were at a comparable level and follow the literature data and standard requirements. Obtained results confirm the thesis of the project. Tensile testing using the hydraulic press provides reliable results and gives comparable to professional test equipment results.

5. CONCLUSIONS

The results of the case study lead to the following conclusions:

- The original device for tensile testing of metallic samples with the usage of pillar hydraulic press was invented. Thanks to the application of computer modelling and FEM simulation, device design optimization was achieved.
- The innovation of the device relies on the application of thrust bearing allows compensating the non-linearity of the stretching welded samples by positioning the loaded jaws uniaxially. The device idea is an objective of the patent application submitted to the Patent Office of the Republic of Poland (Szala, Sawa, et al., 2021).
- The utilization of the built test rig for ultimate tensile strength (UTS) testing was positively validated by the preliminary experimental investigations using model X5CrNi18-10 stainless steel specimens.

- Ultimate tensile strength of X5CrNi18-10 steel specimens, estimated using the commercial device (634 MPa) and obtained from the patented device (620 MPa), were in the range of the standardized values. Fractographic inspection of the specimens reveals the ductile fracture mode.
- The beneficial effect of the designed device is the possibility of stretching the test samples, including welded joints with the help of a press (e.g. in workshop conditions), which can translate into positive economic effects such as avoiding the need to purchase specialized testing strength machines.

Acknowledgement

This project was financed by the Lublin University of Technology Project – Regional Initiative of Excellence from the Ministry of Science and Higher Education on the basis of contract No. 030/RID/2018/19 and within the framework of the statutory activities of the Students Research Group of Materials Technology (Mechanical Engineering Faculty, Lublin University of Technology, Poland).

The authors would like to send their gratitude's to Conti Sp. z.o.o company (Rzeszów, Poland) for the manufacturing of the invented device according to supplied technological documentation.

REFERENCES

Amininejad, A., Jamaati, R., & Hosseinipour, S. J. (2019). Achieving superior strength and high ductility in AISI 304 austenitic stainless steel via asymmetric cold rolling. *Materials Science and Engineering: A*, *767*, 138433. https://doi.org/10.1016/j.msea.2019.138433

Branco, R., Costa, J. D., Martins Ferreira, J. A., Capela, C., Antunes, F. V., & Macek, W. (2021). Multiaxial fatigue behaviour of maraging steel produced by selective laser melting. *Materials & Design*, *201*, 109469. https://doi.org/10.1016/j.matdes.2021.109469

Caban, J., Nieoczym, A., & Gardyński, L. (2021). Strength analysis of a container semi-truck frame. *Engineering Failure Analysis*, *127*, 105487. https://doi.org/10.1016/j.engfailanal.2021.105487

Dziubińska, A., Surdacki, P., Winiarski, G., Bulzak, T., Majerski, K., & Piasta, M. (2021). Analysis of the New Forming Process of Medical Screws with a Cylindrical Head of 316 LVM Steel. *Materials*, *14*(4), 710. https://doi.org/10.3390/ma14040710

EN 10088-2:2014 – Stainless steels. Part 2: Technical delivery conditions for sheet/plate and strip for general purposes. (2014). ISO.

Estrada, Q., Szwedowicz, D., Vergara, J., Solis, J., Paredes, M., Wiebe, L., & Silva, J. (2019). Numerical simulations of sandwich structures under lateral compression. *Applied Computer Science*, *15*(2), 31–41. https://doi.org/10.23743/acs-2019-11

Falkowicz, K., Ferdynus, M., & Wysmulski, P. (2015). FEM analysis of critical loads plate with cut-out. *Applied Computer Science*, *11*(2), 43-49.

Ha, H.-Y., Jang, J. H., Lee, T.-H., Won, C., Lee, C.-H., Moon, J., & Lee, C.-G. (2018). Investigation of the Localized Corrosion and Passive Behavior of Type 304 Stainless Steels with 0.2–1.8 wt % B. *Materials*, *11*(11), 2097. https://doi.org/10.3390/ma11112097

Haizhou, W. (2020). *Geosynthetic material tensile strength detection device for hydraulic engineering detection.* CN212254881 (U), 2020-12-29, Tianjin Xinan Eng Testing Co Ltd.

Hamidah, I., Wati, R., & Hamdani, R. A. (2018). Analysis of AISI 304 Tensile Strength as an Anchor Chain of Mooring System. *IOP Conference Series: Materials Science and Engineering*, *367*, 012058. https://doi.org/10.1088/1757-899X/367/1/012058

ISO 4136:2012 Destructive tests on welds in metallic materials—Transverse tensile test. (2012). ISO.

ISO 6892-1: Metallic materials – Tensile testing – Part 1: Method of test at room temperature. (2010). ISO.

Janeczek, A., Tomków, J., & Fydrych, D. (2021). The Influence of Tool Shape and Process Parameters on the Mechanical Properties of AW-3004 Aluminium Alloy Friction Stir Welded Joints. *Materials*, *14*(12), 3244. https://doi.org/10.3390/ma14123244

Jonak, J., Karpiński, R., & Wójcik, A. (2021). Influence of the Undercut Anchor Head Angle on the Propagation of the Failure Zone of the Rock Medium—Part II. *Materials*, *14*(14), 3880. https://doi.org/10.3390/ma14143880

Kawecki, B., & Podgórski, J. (2017). Numerical results quality in dependence on abaqus plane stress elements type in big displacements compression test. *Applied Computer Science*, *13*(4), 56–64. https://doi.org/10.23743/acs-2017-29

Kilicaslan, M. F., Elburni, S. I., & Akgul, B. (2021). The Effects of Nb Addition on the Microstructure and Mechanical Properties of Melt Spun Al-7075 Alloy. *Advances in Materials Science*, *21*(2), 16–25. https://doi.org/10.2478/adms-2021-0008

Kłonica, M. (2018). Analysis of the effect of selected factors on the strength of adhesive joints. *IOP Conference Series: Materials Science and Engineering*, *393*, 012041. https://doi.org/10.1088/1757-899X/393/1/012041

Kowal, M., & Szala, M. (2020). Diagnosis of the microstructural and mechanical properties of over century-old steel railway bridge components. *Engineering Failure Analysis*, *110*, 104447. https://doi.org/10.1016/j.engfailanal.2020.104447

Lubas, M., & Witek, L. (2021). Influence of Hole Chamfer Size on Strength of Blind Riveted Joints. *Advances in Science and Technology. Research Journal*, *15*(2), 49–56. https://doi.org/10.12913/22998624/135632

Lyalin Mikhajlovich, V., Zykov Mikhajlovich, S., & Sidorov Aleksandrovich, R. (2021). *Installation for Dynamic Tensile Testing of Flat Samples of Materials*. RU2744319 (C1). Federalnoe Gosudarstvennoe Byudzhetnoe Obrazovatelnoe Uchrezhdenie Vysshego Obrazovaniya Tulskij Gos.

Łabanowski, J., Jurkowski, M., Fydrych, D., & Rogalski, G. (2017). Durability of welded water supply pipelines made of austenitic stainless steels. *Welding Technology Review*, *89*(8), 35–40. https://doi.org/10.26628/wtr.v89i8.801

Macek, W., Branco, R., Trembacz, J., Costa, J. D., Ferreira, J. A. M., & Capela, C. (2020). Effect of multiaxial bending-torsion loading on fracture surface parameters in high-strength steels processed by conventional and additive manufacturing. *Engineering Failure Analysis*, *118*, 104784. https://doi.org/10.1016/j.engfailanal.2020.104784

Macek, W., Szala, M., Trembacz, J., Branco, R., & Costa, J. (2020). Effect of non-zero mean stress bending-torsion fatigue on fracture surface parameters of 34CrNiMo6 steel notched bars. *Production Engineering Archives*, *26*(4), 167-173. https://doi.org/10.30657/pea.2020.26.30

Machrowska, A., Karpiński, R., Jonak, J., Szabelski, J., & Krakowski, P. (2020). Numerical prediction of the component-ratio-dependent compressive strength of bone cement. *Applied Computer Science*, *16*(3), 88–101. https://doi.org/10.23743/acs-2020-24

Mahmood, M. A., Popescu, A. C., Oane, M., Chioibasu, D., Popescu-Pelin, G., Ristoscu, C., & Mihailescu, I. N. (2021). Grain refinement and mechanical properties for AISI304 stainless steel single-tracks by laser melting deposition: Mathematical modelling versus experimental results. *Results in Physics*, *22*, 103880. https://doi.org/10.1016/j.rinp.2021.103880

Nedeloni, M. D., Birtărescu, E., Nedeloni, L., Ene, T., Băra, A., & Clavac, B. (2018). Cavitation Erosion and Dry Sliding Wear Research on X5CrNi18-10 Austenitic Stainless Steel. *IOP Conference Series: Materials Science and Engineering*, *416*, 012028. https://doi.org/10.1088/1757-899X/416/1/012028

Nowacki, J., Sajek, A., & Matkowski, P. (2016). The influence of welding heat input on the microstructure of joints of S1100QL steel in one-pass welding. *Archives of Civil and Mechanical Engineering*, *16*(4), 777–783. https://doi.org/10.1016/j.acme.2016.05.001

Pańcikiewicz, K., Świerczyńska, A., Hućko, P., & Tumidajewicz, M. (2020). Laser Dissimilar Welding of AISI 430F and AISI 304 Stainless Steels. *Materials*, *13*(20), 4540. https://doi.org/10.3390/ma13204540

Pezowicz, C., Szotek, S., Kobielarz, M., & Wudarczyk, S. (2016). *Device for biaxial stretching of biological samples*. PL412122 (A1), 2016-11-07, Wojewódzki Szpital Specjalistyczny We Wrocławiu.

Rout, M. (2020). Texture-tensile properties correlation of 304 austenitic stainless steel rolled with the change in rolling direction. *Materials Research Express*, *7*(1), 016563. https://doi.org/10.1088/2053-1591/ab677c

Różyło, P., Wysmulski, P., & Falkowicz, K. (2017). Fem and Experimental Analysis of Thin-Walled Composite Elements Under Compression. *International Journal of Applied Mechanics and Engineering*, *22*(2), 393–402. https://doi.org/10.1515/ijame-2017-0023

Rudawska, A., Zaleski, K., Miturska, I., & Skoczylas, A. (2019). Effect of the Application of Different Surface Treatment Methods on the Strength of Titanium Alloy Sheet Adhesive Lap Joints. *Materials*, *12*(24), 4173. https://doi.org/10.3390/ma12244173

Sarre, B., Flouriot, S., Geandier, G., Panicaud, B., & de Rancourt, V. (2016). Mechanical behavior and fracture mechanisms of titanium alloy welded joints made by pulsed laser beam welding. *Procedia Structural Integrity*, *2*, 3569–3576. https://doi.org/10.1016/j.prostr.2016.06.445

Skowrońska, B., Chmielewski, T., Kulczyk, M., Skiba, J., & Przybysz, S. (2021). Microstructural Investigation of a Friction-Welded 316L Stainless Steel with Ultrafine-Grained Structure Obtained by Hydrostatic Extrusion. *Materials*, *14*(6), 1537. https://doi.org/10.3390/ma14061537

Szala, M., Chocyk, D., Skic, A., Kamiński, M., Macek, W., & Turek, M. (2021). Effect of Nitrogen Ion Implantation on the Cavitation Erosion Resistance and Cobalt-Based Solid Solution Phase Transformations of HIPed Stellite 6. *Materials*, *14*(9), 2324. https://doi.org/10.3390/ma14092324

Szala, M., & Łukasik, D. (2018). Pitting Corrosion of the Resistance Welding Joints of Stainless Steel Ventilation Grille Operated in Swimming Pool Environment. *International Journal of Corrosion*, *2018*, 9408670. https://doi.org/10.1155/2018/9408670

Szala, M., Sawa, M., & Walczak, M. (2021). *Device for specimens uniaxially tensile strength tesitng (Urządzenie do statycznego, jednoosiowego rozciągania próbek)* (Poland Patent Nr P.437489).

Szala, M., Szafran, M., Macek, W., Marchenko, S., & Hejwowski, T. (2019). Abrasion Resistance of S235, S355, C45, AISI 304 and Hardox 500 Steels with Usage of Garnet, Corundum and Carborundum Abrasives. *Advances in Science and Technology. Research Journal*, *13*(4), 151–161. https://doi.org/10.12913/22998624/113244

Szala, M., Winiarski, G., Wójcik, Ł., & Bulzak, T. (2020). Effect of Annealing Time and Temperature Parameters on the Microstructure, Hardness, and Strain-Hardening Coefficients of 42CrMo4 Steel. *Materials*, *13*(9), 2022. https://doi.org/10.3390/ma13092022

Szklarek, K., & Gajewski, J. (2020). Optimisation of the Thin-Walled Composite Structures in Terms of Critical Buckling Force. *Materials*, *13*(17), 3881. https://doi.org/10.3390/ma13173881

Świć, A., Gola, A., Sobaszek, Ł., & Orynycz, O. (2020). Control of Machining of Axisymmetric Low-Rigidity Parts. *Materials*, *13*(21), 5053. https://doi.org/10.3390/ma13215053

Zagórski, I., Kulisz, M., Kłonica, M., & Matuszak, J. (2019). Trochoidal Milling and Neural Networks Simulation of Magnesium Alloys. *Materials*, *12*(13), 2070. https://doi.org/10.3390/ma12132070

Zheng, C., Liu, C., Ren, M., Jiang, H., & Li, L. (2018). Microstructure and mechanical behavior of an AISI 304 austenitic stainless steel prepared by cold- or cryogenic-rolling and annealing. *Materials Science and Engineering: A*, *724*, 260–268. https://doi.org/10.1016/j.msea.2018.03.105

Żebrowski, R., Walczak, M., Korga, A., Iwan, M., & Szala, M. (2019). Effect of Shot Peening on the Mechanical Properties and Cytotoxicity Behaviour of Titanium Implants Produced by 3D Printing Technology. *Journal of Healthcare Engineering*, *2019*, 8169538. https://doi.org/10.1155/2019/8169538